A Printed Circuit Board Stack Based Antenna Implementation and A Study in Green's

Functions

A Thesis

Presented in Partial Fulfillment of the Requirements for the

Degree of Master of Science

with a

Major in Electrical Engineering

in the

College of Graduate Studies

University of Idaho

by

Jeremy Michael Ziegler

Major Professor: Ata Zadehgol, Ph.D.

Committee Members: Brian Johnson, Ph.D.; Feng Li, Ph.D.

Department Administrator: Mohsen Guizani, Ph. D.

May 2017

Authorization to Submit Thesis

This thesis of Jeremy Michael Ziegler, submitted for the degree of Master of Science with a major in Electrical Engineering and titled "A Printed Circuit Board Stack Based Antenna Implementation and A Study in Green's Functions," has been reviewed in final form. Permission, as indicated by the signatures and dates given below, is now granted to submit final copies to the College of Graduate Studies for approval.

Major Professor: _____Date_____
                                    Ata Zadehgol, Ph.D.

Committee
Members: _____Date_____
                                    Brian Johnson, Ph.D.

_____Date_____
                                    Feng Li, Ph.D.

Department
Administrator: _____Date_____
                                    Mohsen Guizani, Ph.D.

Abstract

The first part of this thesis presents a new and novel method for realizing complex antenna designs. The method utilizes a printed circuit board stack that is appropriately contoured along the vertical direction in order create the three dimensional structure for the antenna. Selective copper etching and copper plated edges are used to create the antenna elements. The method is applied to an electrically small, hemispherical helix antenna for the realization of an otherwise complex structure. The design is then characterized in detail and compared with prior works.

The second part of this thesis investigates the Green's function method for solving inhomogeneous differential equations. An overview of the theory is presented and one-dimensional examples are presented and compared to results obtained using the finite-difference time domain method. Finally, the work is concluded with a discussion of opportunities for future work.

Acknowledgements

It is with sincere gratitude that I thank Dr. Zadehgol for being my advisor. His mentoring, passion, and patience has been invaluable for my academic and professional growth.

I also would like to thank Dr. Johnson and Dr. Li for being on my thesis committee. I am ever grateful for their time and advice.

Dedication

To my wife, Justine, and daughter, Peyton. Your love and support made this possible.

Table of Contents

List of Tables

List of Figures

CHAPTER 1

Introduction

The trend of technology has been such that the size of electronic devices is continually decreasing. A perfect example of this are mobile phones, which seek to minimize size and maximize efficiencies, such as battery life. However, often the communication methods and the carrier frequencies utilized by these devices remains unchanged. From electromagnetics, it is known that the wavelength of a wave is inversely proportional to the frequency. This means that the physical size of the device is becoming proportional to higher and higher frequencies. This presents a significant challenge to the antenna designer when devices shrink to sizes that are less than a tenth of the electrical wavelength being used. At this point, the antenna is considered to be electrically small, which typically results in significant trade-offs in antenna performance. In order to overcome this predicament, studies and advances in electrically small antennas are needed in order to create electrically small antennas that are efficient and meet desired performance specifications. Electrically small antennas will continue to be a highly-demanded research field, and advances can be applied to the operational frequency of interest, whether it be millimeter wave applications or sub-gigahertz communications.

Within antenna deign, three of the most common antenna realization methods are wire, printed circuit boards (PCBs), and ceramic chips, each of which are outlined in Table 1.1. One of the most widely used antenna types in high-volume manufacturing is the PCB antenna, primarily due to the low cost. Further advancements utilizing this technology would be of great interest.

In order to further the advancement of electrically small antennas, this research work presents a new fabrication method which leverages PCB technology to realize three dimensional antenna designs through stacks of two layer PCBs. Since a primary aim of using an electrically small antenna is to maximize the available trade space, the PCB stack method is then enhanced by creating a cavity within the structure in order to house circuit components

Table 1.1: Common Antenna Types [1].

Antenna Type	Advantages	Disadvantages
Wire	Performance	Size Cost
Printed Circuit Board	Cost	Design changes require a new board revision
Ceramic Chip	Size	Cost Design changes require a new board revision

without significantly impacting antenna performance. A sensitivity analysis of a hemispherical helix antenna created using PCB stack method is then performed to understand the impact of manufacturing process variations on antenna performance. This data is also used to develop design enhancements that are unique to the PCB stack method.

The aforementioned PCB stack method was primarily developed using commercial simulation software based on the Finitie-Difference Time Domain (FDTD) method. While the FDTD method is a powerful, electromagnetic simulation method, it can leave the user with a lack if physical insight behind a given antenna design. This can impede the development of novel designs by rendering a guess and check design process. The physical insights offered though analytic approaches is of interest and one method is through the use of Green's functions. This work presents background information on the Green's function method and provides illustrative examples. The conclusion provides a discussion on future work opportunities to further integrate analytic methods with antenna design.

CHAPTER 2

Design and Simulation of a Four-Arm Hemispherical Helix Antenna Realized Through a Stacked Printed Circuit Board Structure

Forthcoming in conference proceedings from *2016 IEEE Electrical Design of Advanced Packaging and Systems (EDAPS)* [2].

As transistors, integrated circuits, and other electronic components decrease in physical size, opportunities are sought for the optimization and miniaturization of antennas. Electrically small antennas have become attractive, due to their small physical size when compared to the wavelength of operation [3]. Much work has been done to determine the theoretical performance limits of an electrically small antenna, initially investigated in [4] and later expanded upon in [5] and [6]. Antenna performance is typically evaluated based upon the Q of the antenna, which is inversely proportional to the bandwidth, and its ratio to the minimum achievable Q given by [5]:

$$Q_{min} = \left(\frac{1}{(ka)^3} + \frac{1}{(ka)} \right) \tag{2.1}$$

Where k is the free space wavenumber of the electromagnetic wave and a is the radius of a sphere that encloses the antenna. The spherical helix antenna (Fig. 2.1) has been investigated for use as an electrically small antenna and has been able to reach Q values close to the minimum achievable limit [7–11].

A variety of different design approaches have been investigated [12–14] for realization of the multi-arm spherical helix antenna, including a miniaturization technique through folding of the antenna elements [15]. However, the structure of the spherical helix presents a fabrication challenge in order to realize the designed geometry in a timely and inexpensive fashion. Of great importance is repeatability of the process and its ability to stay within acceptable

design tolerance in order to guarantee optimal antenna performance. Many implementations have been investigated, including coupled planar elements [16], rapid prototyping [17], and 3D printing [18].
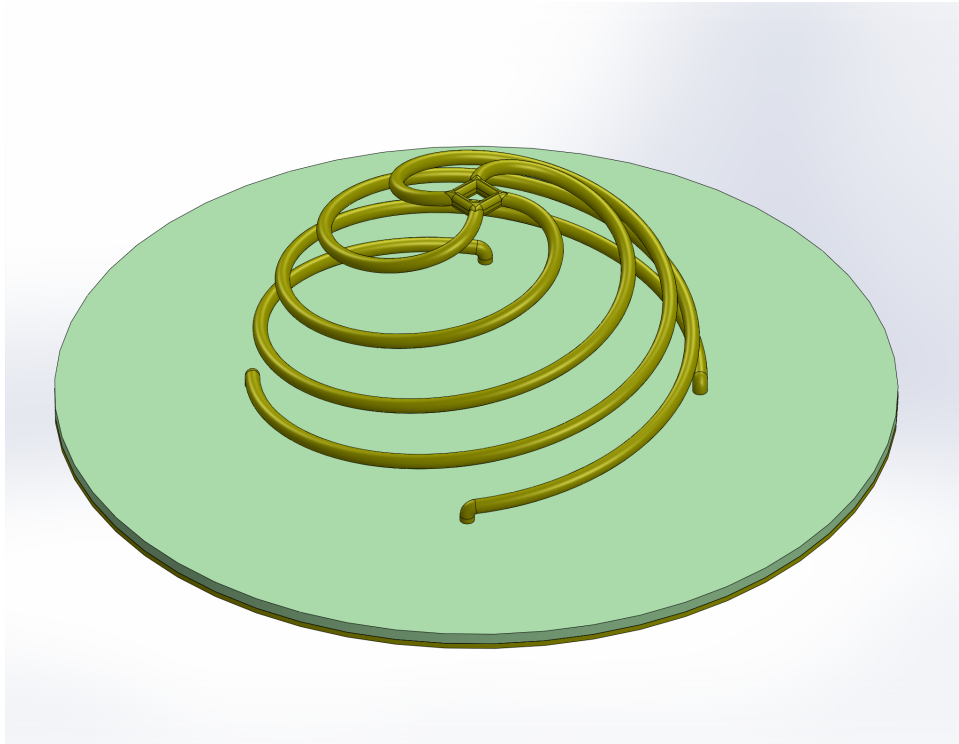
Figure 2.1: The four arm spherical helix wire antenna used as the baseline antenna for this investigation.
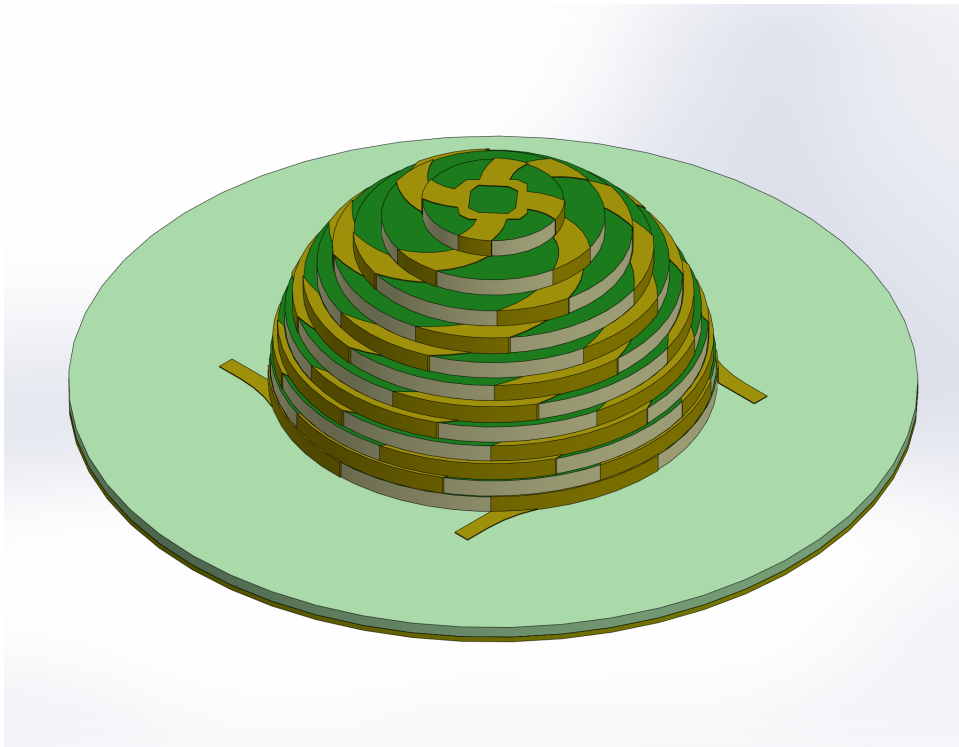
Figure 2.2: A four-arm spherical helix antenna created through a stack of PCBs.

To overcome implementation and fabrication challenges, a novel approach is designed and simulated that leverages printed circuit board (PCB) technology. The basis of this approach is the utilization of a stack of two-layer PCBs that replicate the three dimensional geometry of a hemispherical antenna (Fig. 2.2). PCB stacking techniques have been used with success by [19] for design of a small wireless sensor node and by [12] for the creation of microwave components and subsystems. The same methodology is utilized in this research for the hemispherical helix antenna design. With the proposed approach, the thickness and outline of each PCB within the stack is adjusted to optimally spatially sample the three dimensional geometry. The antenna conductors are realized through selective copper plating of the PCB edges and top copper layers. The stacked PCB based antenna is analyzed through simulation using the SEMCAD X Matterhorn Antenna software package. The individual PCBs are modeled with the copper elements treated as contiguous elements that follow the contour of the stacked PCBs, whose composition has been modeled with two different PCB substrates. The antenna design is evaluated on performance metrics of radiation pattern, reflection coefficient, and efficiency.

2.1   Antenna Design

This research considers two hemispherical four-arm helix antennas developed based upon principles in [20, 21]. In order to evaluate effectiveness of the PCB stacked antenna design, a four-arm hemispherical helix antenna was designed using wire conductors. A wire radius of 1.25 mm was chosen, and the design served as a baseline for comparison due to its thorough characterization in other research [20]. Specifications common for both antennas are outlined in Table 2.1. The antenna feed was modeled as being connected directly to a 50 ohm source.

For replicating the baseline antenna as a stack of PCBs, a structure utilizing twelve two-layer PCBs with a board thickness of 1.575 mm was chosen, with both parameters being determined empirically. The PCB stack conforms to the hemispherical geometry used for the baseline wire antenna, with a height slightly less than the radius of the hemisphere.

Table 2.1: Antenna specifications for the four-arm hemispherical wire antenna

Number of Turns	Antenna Radius (mm)	Ground Plan Radius (mm)	Target Frequency (MHz)
1	19.1	36	1000

The width of the planar copper elements were restricted to not exceed the circumference of the baseline wire antenna. A 50 ohm microstrip is used to interface with the PCB-based antennas. SolidWorks was used to create the antenna geometries for both antennas, which were then simulated using SEMCAD X Matternhorn.

2.2 Results

Three antenna implementations were simulated as having copper conductors with a conductivity of $5.813 \cdot 10^7$ siemens per meter. The wire-based helix antenna had a resonant frequency that was slightly lower than the designed target frequency, likely due to unaccounted element length in the connection to the antenna ground plane.

The antenna feed geometry was optimized to provide a 50 ohm match for each of the dielectric substrates. The antennas were then tuned to resonance by adjusting the spacing between the antenna and the ground plane. Since the radius of the antenna also remained constant, a significant shift in frequency was observed (see Fig. 2.3) with the stacked PCB antennas for two reasons: dielectric loading of the antenna elements, due to the higher relative permittivities of the substrates, and longer antenna element length. During the conversion to planar geometry, a meander line is created as the copper traverses the PCB stack. The FR4 dielectric significantly impacts the radiation efficiency of the antenna, due to the increased material permittivity leading to increased internal stored energy [22] and due to the high loss tangent of the material. However, this has negligible impact on the antenna directivity (Fig. 2.4 and 2.5), which achieves a peak value of 1.8 dBi, which is slightly higher than the 1.76 dBi peak directivity of the wire antenna. With the proof of

concept simulations completed, further adjustments to the antenna feed and ground spacing can be made to improve overall antenna efficiency. The impacts to antenna efficiency are supported by the data collected in [23] and one additional advantage pointed out is that the dielectric material does increase the radiation resistance of the antenna, at lower frequencies, which helps to improve the overall antenna efficiency when compared to the performance of the wire antenna at those same frequencies.

The quality factors for the wire antenna and the PCB stack antenna with RO3003 dielectric are show in Fig. 2.6. It can be seen that the wire antenna achieves a Q value of around 35, which is 1.6 times the minimum Q value calculated by (2.1) for the wire antenna geometry and associated resonant frequency. This value is in agreement with the Q values presented in [21] for similar antenna designs. The PCB stack antenna with RO3003 dielectric achieved a higher Q value of about 110 but, due to the lower resonant frequency of 793.6 MHz, the minimum Q value increases slightly to 34.34. This results in a Q value that is 3.2 times the lower bound calculated by (2.1). The higher quality factor of the PCB stack antenna is in large part due to the addition of the dielectric material to the antenna core.

The dieletric material impact can be broken into to two componenets: 1) stored energy and 2) dissapated power. The effects of the dielectric permittivity to antenna performance can be best understood through the inspection of the expressions for the time-averaged dissapated power and stored energy given by [24]:

$$\overline{W}_e = \frac{1}{2} \int \int \int \epsilon' \, |E|^2 \, dr \tag{2.2}$$

$$\overline{P}_d = \int \int \int \omega \epsilon'' \, |E|^2 \, dr \tag{2.3}$$

Where the over bar denotes a time-averaged quantity. A comparison was performed by [25] to evaluate the impact of dielectric material to antenna efficiency and a reduction on the order of -3 dB was measured compared to the antenna's free space counterpart. This

study was performed at higher relative permittivity values, but loss tangent values were not specifed. Similar conclusions can be drawn that the addition of the dielectric material results in a reduction in the efficency bandwidth product of the antenna.

Table 2.2: Simulated resonant frequency and radiation efficiency

Antenna	Resonant Frequency (MHz)	Radiation Efficiency (%)
Wire	942.5	99
PCB - FR4	682.8	14.5
PCB - RO3003	793.6	81
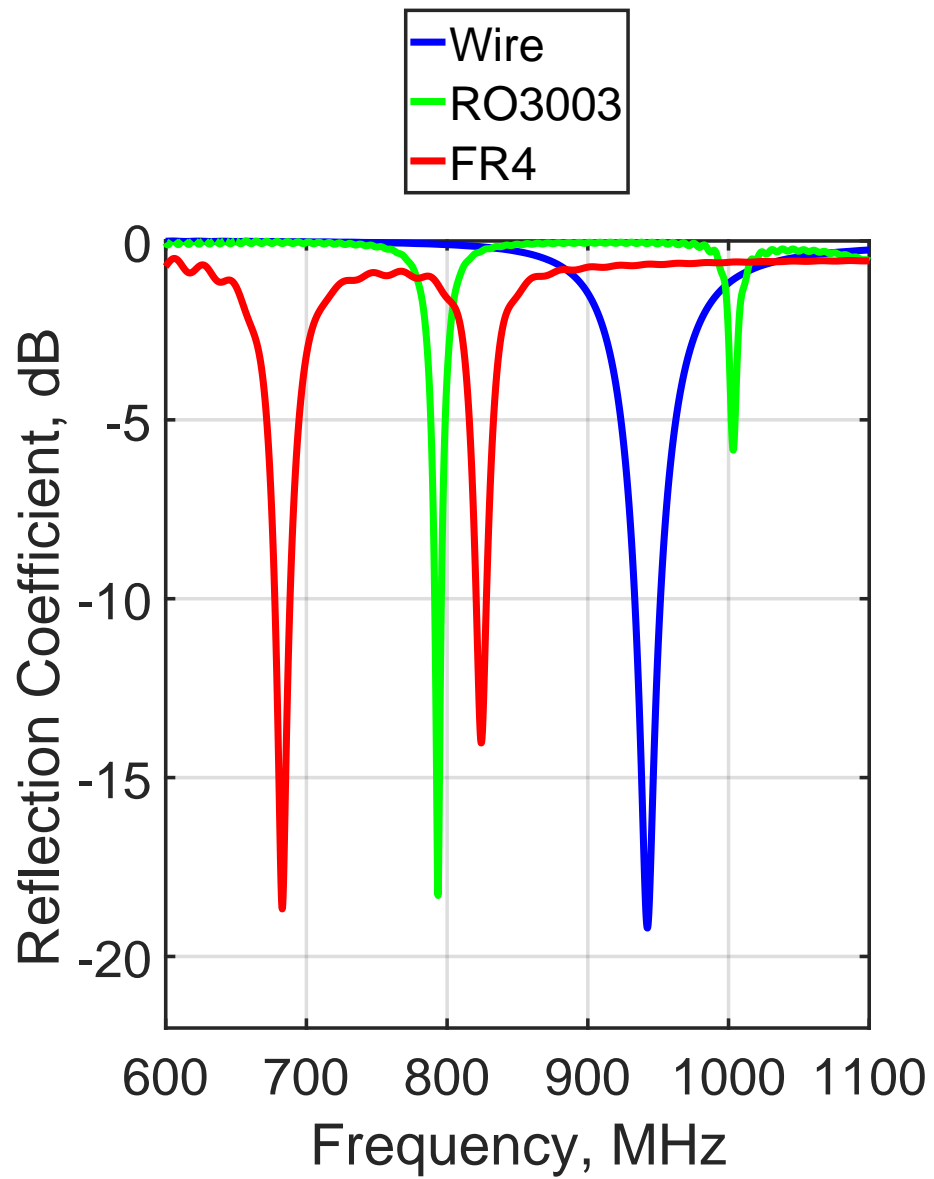
Figure 2.3: Simulated reflection coefficient for the three antennas.
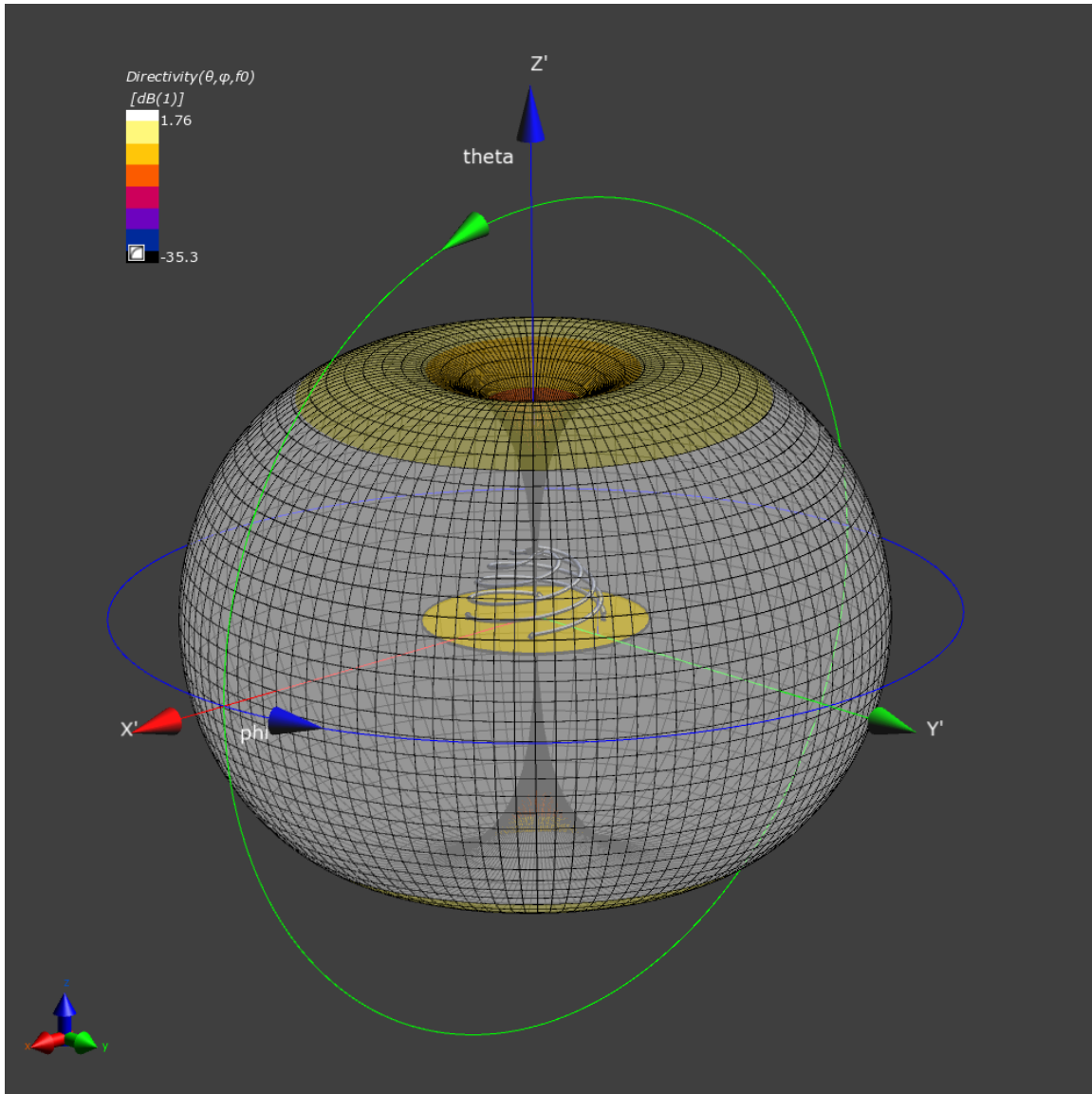
Figure 2.4: Directivity plot for the wire four-arm hemispherical helix antenna.
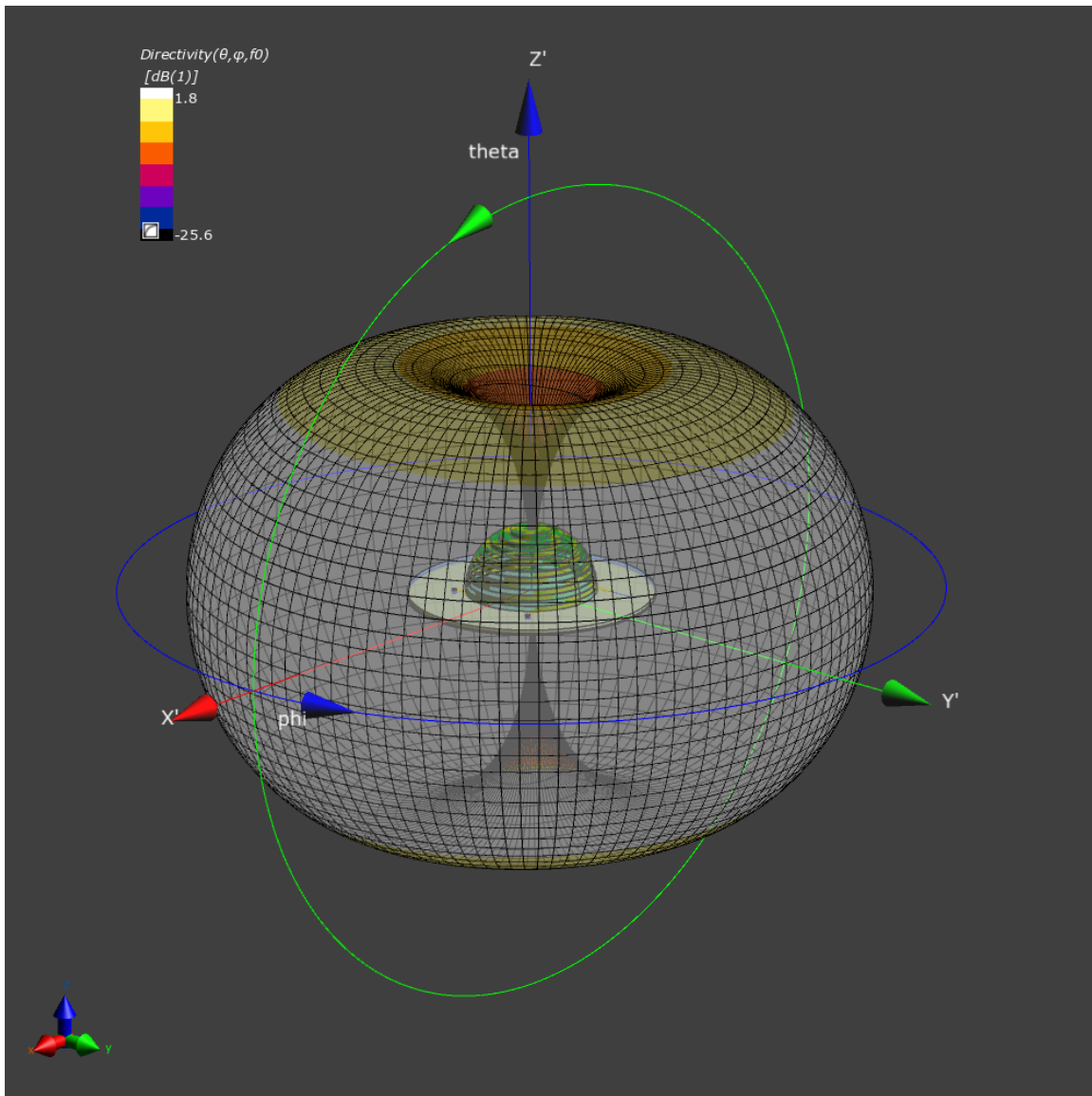
Figure 2.5: Directivity plot for the PCB stack four-arm hemispherical helix antenna.
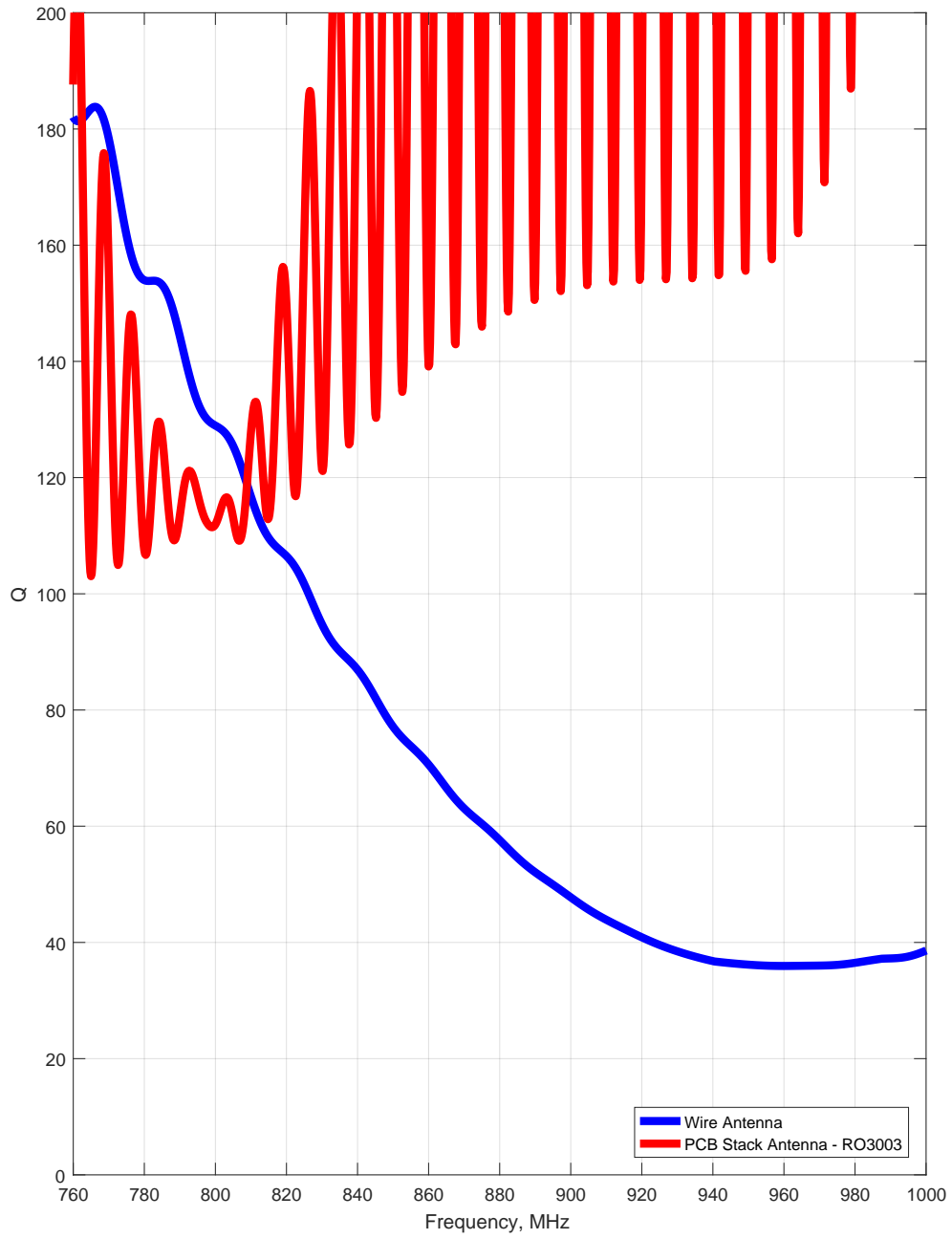
Figure 2.6: Quality factor for the wire-based and PCB stack antenna.

2.3   Discussion

A novel hemispherical four-arm helix antenna was developed based upon PCB stacking techniques and compared against a similar wire antenna design. The PCB stack antenna showed similar directivity performance and lower resonant frequency, due to the additional element length and dielectric loading of the antenna from the PCB substrate. The PCB antennas have comparable return loss but less radiation efficiency.

This method provides a simplified alternative to wire-based fabrication methods to realize complex antenna geometries. PCB stacked antennas can also be utilized for a variety of applications, including antenna in package solutions. Low Temperature Cofired Ceramic (LTCC) is a strong competitor for these applications, but PCB technology offers considerable cost savings, with LTCC technology being as much as 20 times the costs of PCB based designs [1].

CHAPTER 3

Electrically Small PCB Stack Hemispherical Helix Antenna with Air Core

Forthcoming in conference proceedings from *2017 International Workshop on Antenna Technology (iWAT)* [26].

Electrically small antennas continue to be the subject of much research attention due to the space savings offered when the electrical wavelengths of interest are comparable to or larger than the dimensions of the target application. This is especially valuable in devices such as mobile phones and other electronics that demand an optimization in device size, weight, and power consumption. A popular performance metric of the electrically small antenna is the quality factor, Q, of the antenna and its ratio to the minimum achievable Q. The theoretical minimum Q value of electrically small spherical antennas has been derived in the pioneering work of [4, 27]. This popular performance metric is typically expressed as a ratio of antenna Q and the minimum achievable Q, which is given by (2.1).

For the electric dipole antenna with a dielectric core of relative permittivity ϵ_r, the minimum Q can be determined by [28, 29]:

$$Q_e = \left(1 + \frac{\epsilon_r}{2}\right)\frac{1}{(ka)^3} \tag{3.1}$$

The spherical and hemispherical helix antenna have been known to achieve Q values that approach the lower bound (2.1) as presented in [20] for an air core and in [29] for a magnetic core. One setback of the hemispherical helix antenna is that it presents a challenging geometry to fabricate [18]. A alternative realization has been proposed in [30] that utilizes a printed circuit board (PCB) stack approach to the design of the antenna. This approach results in a hemispherical antenna with a solid dielectric core with a minimum Q that is defined by (3.1).

In order to maximally utilize all space afforded to the antenna, we turn our attention

to the volume available within the hemispherical helix antenna core. With an air core, this space can be utilized for circuit components in order to minimize the impact of the overall antenna volume on the design space claim. The aim of this research effort is to evaluate the impact on antenna performance for two core designs that allow the internal antenna volume to be better utilized. The antenna studied in this research effort is shown in Fig. 3.1 and is evaluated for two practical core configurations: an air core and a composite metal core. The composite metal core is designed to provide a Faraday cage integral to the air core of the antenna. This advantage was also leveraged in [31] to utilize the space within an antenna cube for multiple-input multiple-output (MIMO) technology. The two core configurations have been simulated in order to evaluate their impact on the following antenna performance metrics: radiation efficiency, Q, input impedance, and directivity.
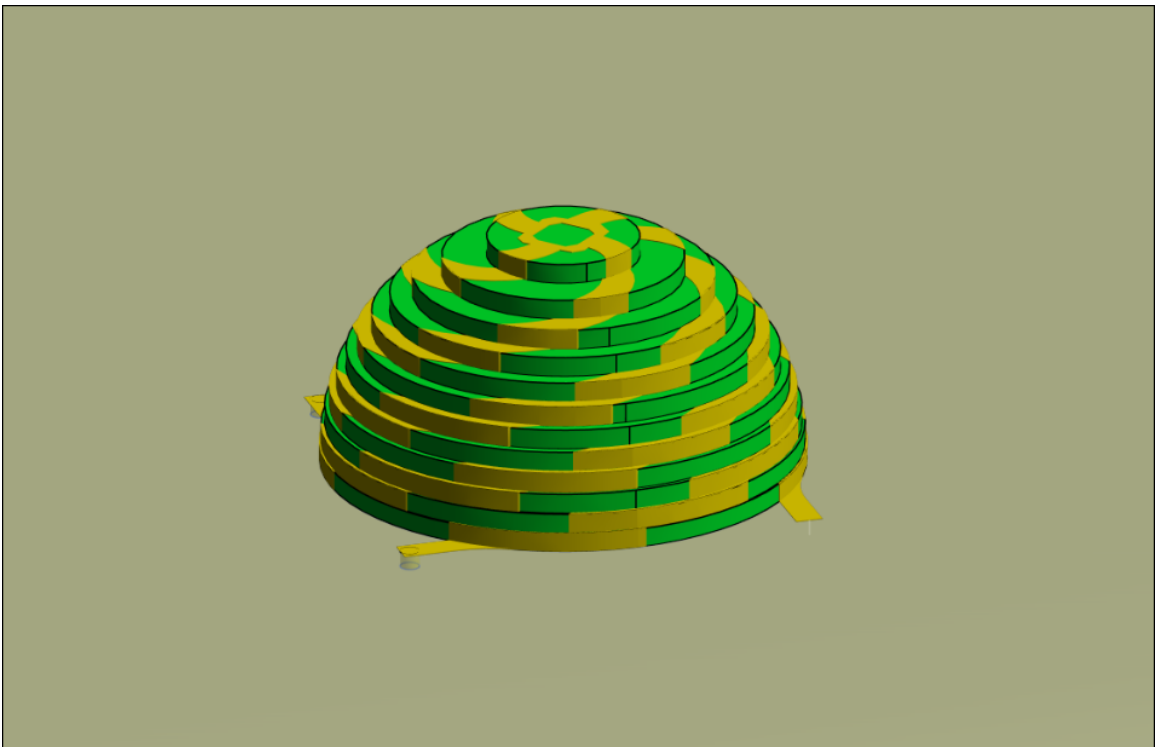
Figure 3.1: Model of the PCB stack based four-arm hemispherical helix antenna.

3.1 Design Formulation

As mentioned in the preceding section, one design criterion of interest is the antenna Q and its ratio to the minimum achievable limit. This is a popular metric used to evaluate the performance of an electrically small antenna. In order to determine the ratio of the antenna Q to the lower bound given by (2.1), the Q of an antenna can be determine by [32]:

$$Q = \frac{\omega}{2R_A} \sqrt{\left(\frac{dR_A}{d\omega}\right)^2 + \left(\frac{dX_A}{d\omega} + \frac{|X_A|}{\omega}\right)^2} \qquad (3.2)$$

Where ω is the angular frequency. R_A and X_A are the frequency-dependent resistance and reactance measured at the antenna feed.

The hemispherical helix antenna design is derived based upon methods outlined in [20, 21, 30]. A four-arm hemispherical helix antenna configuration was chosen for its ability to achieve a feed point resistance close to 50 Ω [20]. The antenna is first designed as a traditional wire-based implementation with a wire radius of 1.25 mm and remaining specifications as outlined in Table 3.1. The wire-based antenna is then spatially sampled and replicated onto a stack of twelve individual, two-layer PCBs [30]. Each of the PCBs has a thickness of 1.575 mm and a copper thickness of 71 µm. The hemispherical helix arms have a variable width, which decreases as they traverse up the PCB stack from roughly 3.2 mm to 2.5 mm. This is primarily due to the coarse spatial discretization achieved with the chosen PCB layer thickness.

The antenna feed consists of a 50 Ω microstrip that tapers to an intersection with copper

Table 3.1: Antenna specifications that are shared between the two antenna core designs.

Helix Turns	Antenna Radius (mm)	Ground Plane Radius (mm)	Dielectric Material	Conductor
1	19.1	128	RO3003 $\epsilon_r = 3$	Copper $\sigma = 5.8\mathrm{e}7\frac{S}{m}$

plating on the PCB stack antenna. This interface method is replicated for the remaining three helix arm connections with the addition of a via termination to the ground plane. The antenna is tuned to a target 50 Ω input impedance through the adjustment of the dielectric thickness between the PCB stack antenna and the ground plane over a range of 0.045 mm to 0.5 mm. This minimizes the need for antenna matching components. A top view of the antenna connections is shown in Figure 3.2.

The geometry of the hemispherical helix PCB stack antenna with an air core is shown in Fig. 3.3. The diameter of the air core radius was first chosen to maximize unoccupied volume within the antenna and was then adjusted in order to tune the antenna to an acceptable input impedance at the antenna's resonant frequency. The air core has a radius that is offset from outer PCB edge of each layer by a distance of 5 mm.

A similar approach was taken with the hemispherical helix PCB stack antenna with composite metal core shown in Fig. 3.4. The Faraday cage is realized through the application of copper plating to the inner PCB surface within the antenna core and is connected to the antenna ground plane. The radius of the Faraday cage is offset from the outer PCB edge of each layer by a distance of 7.5 mm. The top of the cage can be implemented through copper placed on the bottom layer of a contiguous PCB disk within the PCB stack. To simplify the developed antenna model for simulation, this feature was omitted and an air cavity was placed directly above a copper sheet at the top of the Faraday cage. The developed model was further simplified by making the Faraday cage a solid, homogeneous copper entity.
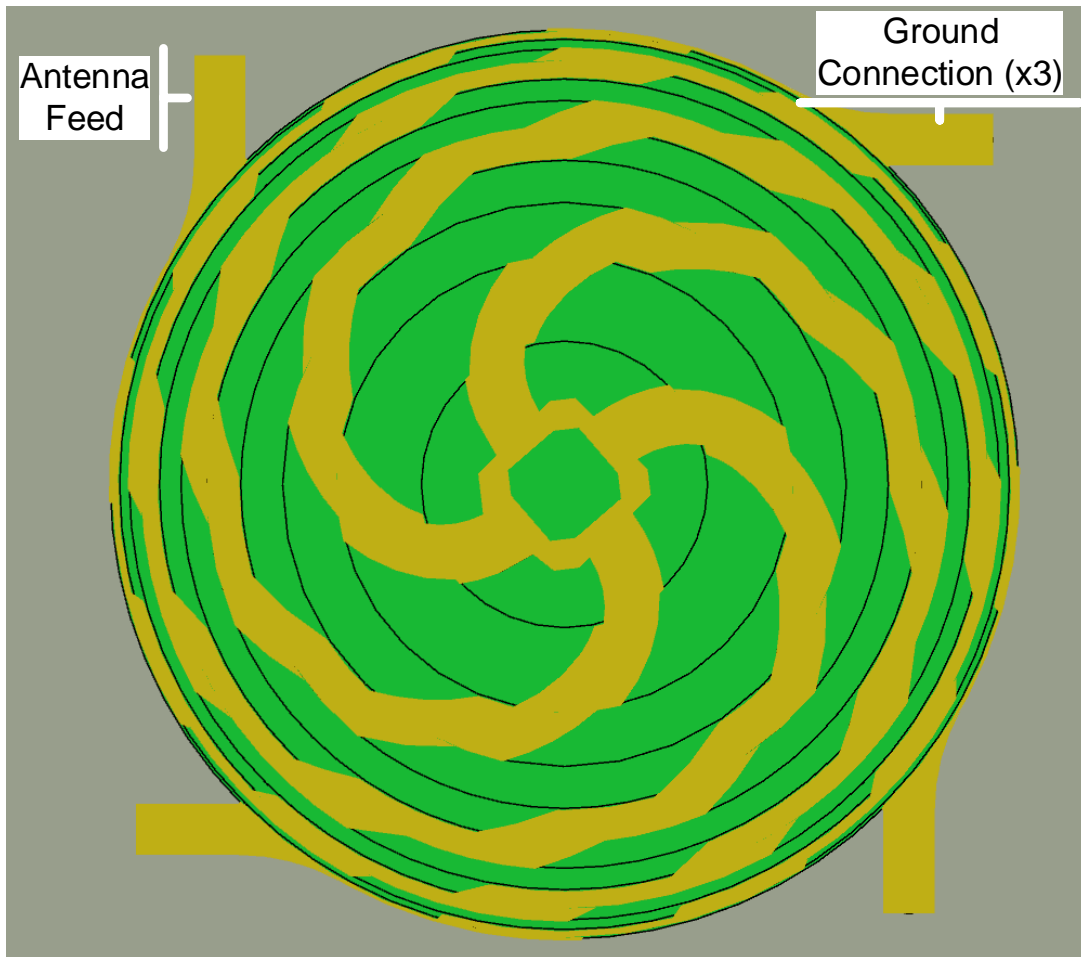
Figure 3.2: Top view of the antenna showing the antenna feed and ground plane connections.
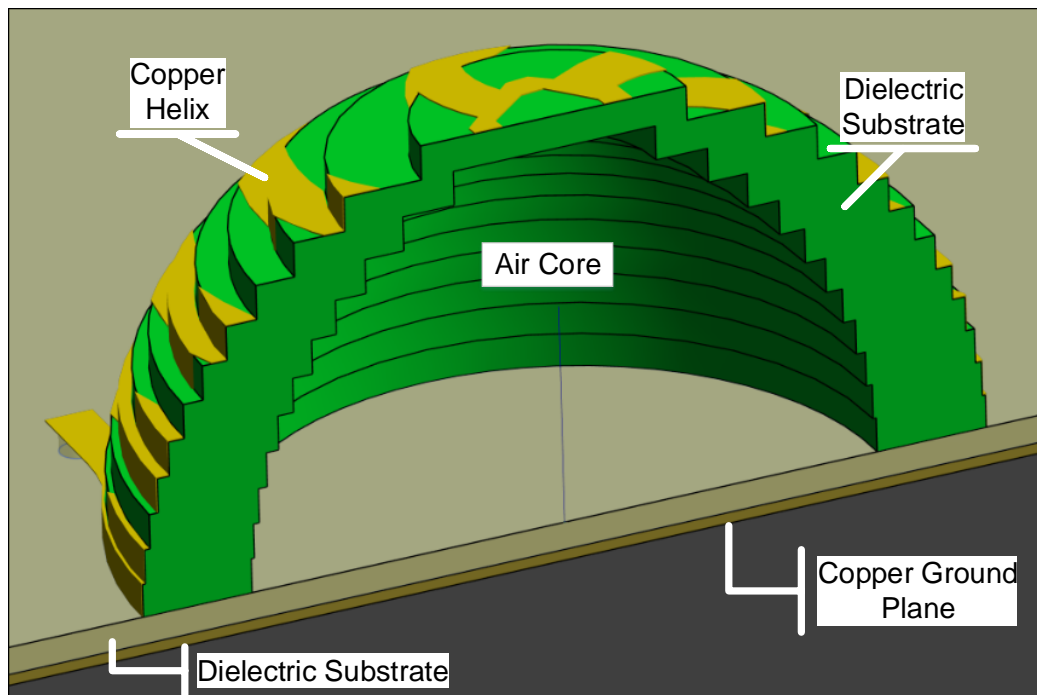
Figure 3.3: Section view of the PCB stack based hemispherical helix antenna with air core.
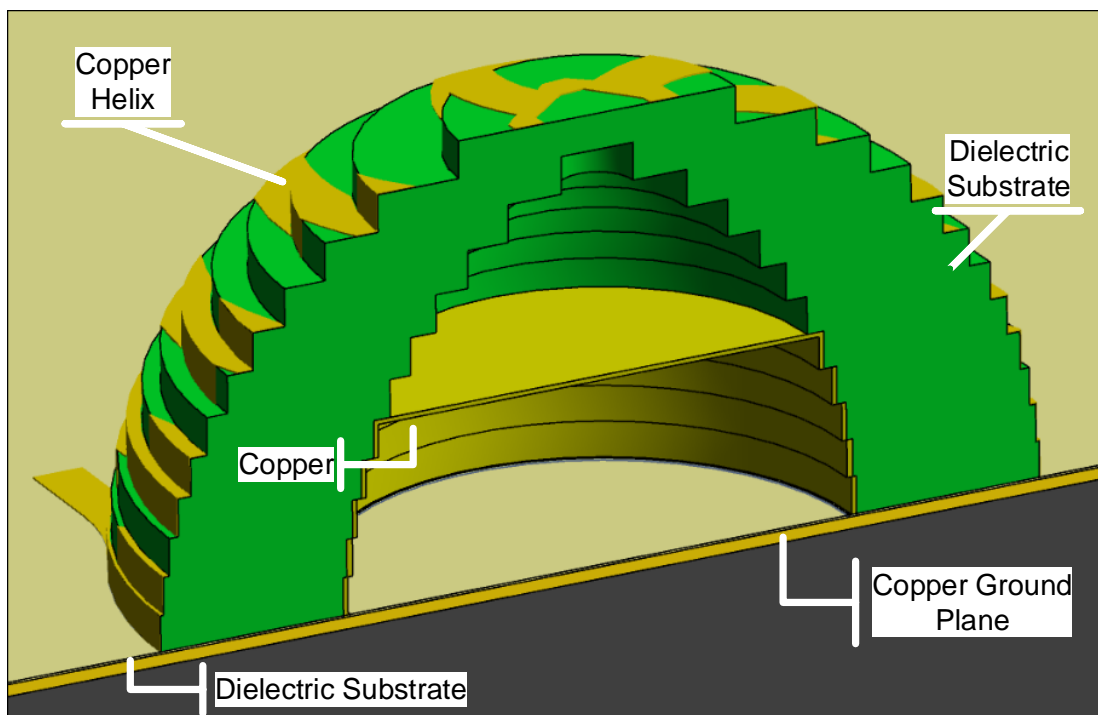
Figure 3.4: Section view of the PCB stack based hemispherical helix antenna with composite metal core that results in an integral Faraday cage.

Table 3.2: Simulation results for the two antenna core configurations

Antenna Core	Resonant Frequency (MHz)	Radiation Efficiency (%)	$\frac{Q}{Q_{min}}$	ka	Approximate Core Volume (mm^3)
Air	784	85	2.5	0.314	5871
Composite Metal	731.6	61	3.7	0.293	3028

3.2 Results

The antenna Q values have been computed using the equation provided in (3.2) and plotted in Fig. 3.7. The air core achieves a Q that is within ten percent of the limit defined by (3.1) for $ka = 0.314$. The Q of the air core antenna is then $2.5Q_{min}$, which is limited by the permittivity of the dielectric material used for the construction of the PCBs. Further Q enhancements can be realized by utilizing materials with a lower ϵ_r. If all other antenna design parameters are held constant, this will also result in a higher resonant frequency.

The input impedance of the air core antenna was optimized through adjustments in the dielectric layer thickness between the main antenna structure and the ground plane to achieve an input impedance close to 50 Ω. Fig. 3.5 shows a reflection coefficient value of about -30 dB, which results in minimal mismatch loss. There is also an increase in radiation efficiency of roughly 4% over a similar antenna with a solid dielectric core [30].

The composite metal core results in a notable impact on antenna performance. In order to achieve radiation efficiencies above 30%, the height of the Faraday cage was truncated so as to not occupy the full height available within the core of the antenna. An air cavity above the Faraday cage was left so as to realize some of the efficiency enhancements over a solid dielectric core. However, further simulation needs to be performed to verify effectiveness of the air cavity in this configuration.

The inner radius of the composite metal core was also reduced in an effort to tune the antenna to the desired input impedance. As can be seen in Fig. 3.5, improvements in the

reflection coefficient can be realized through further optimization of composite metal core geometry. The composite metal core also results in an increased Q to $3.7Q_{lim}$ and $1.6Q_e$. However, the directivity of the antenna remains nearly unchanged between the two antenna core configurations (Fig. 3.6).
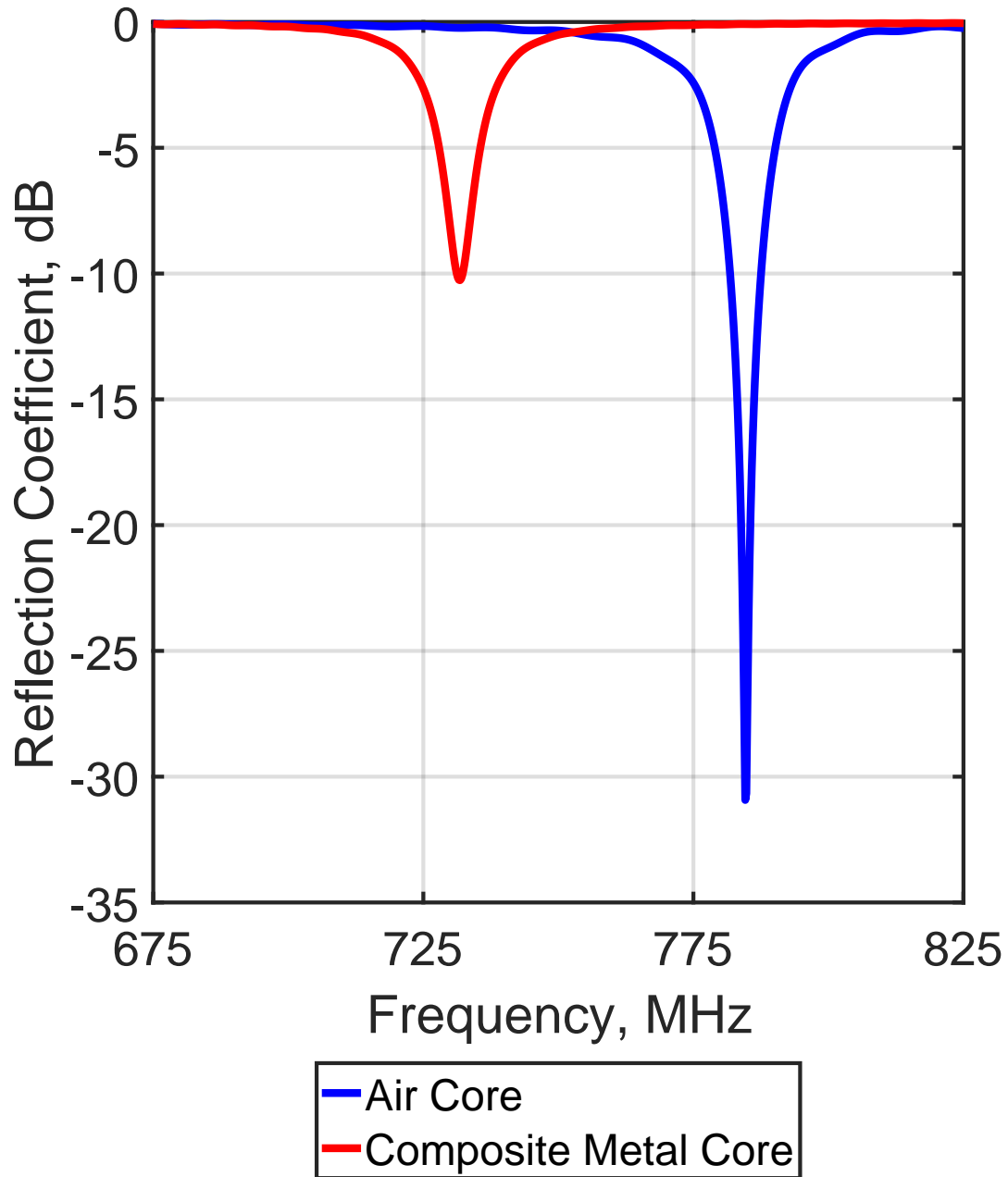
Figure 3.5: Reflection coefficient of the antenna for the two core configurations.
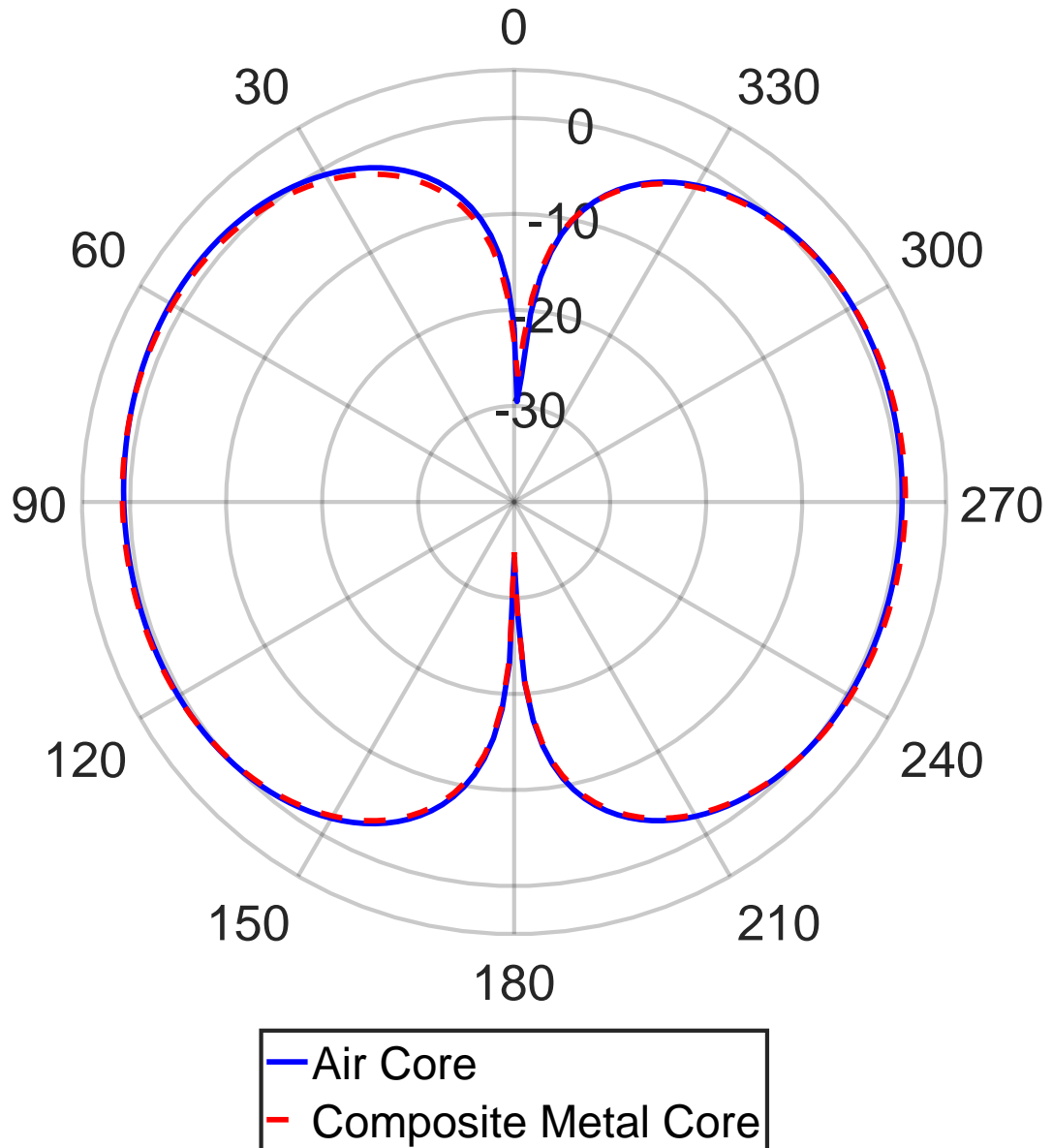
Figure 3.6: Antenna directivity, at resonance, for the two core configurations being investigated.
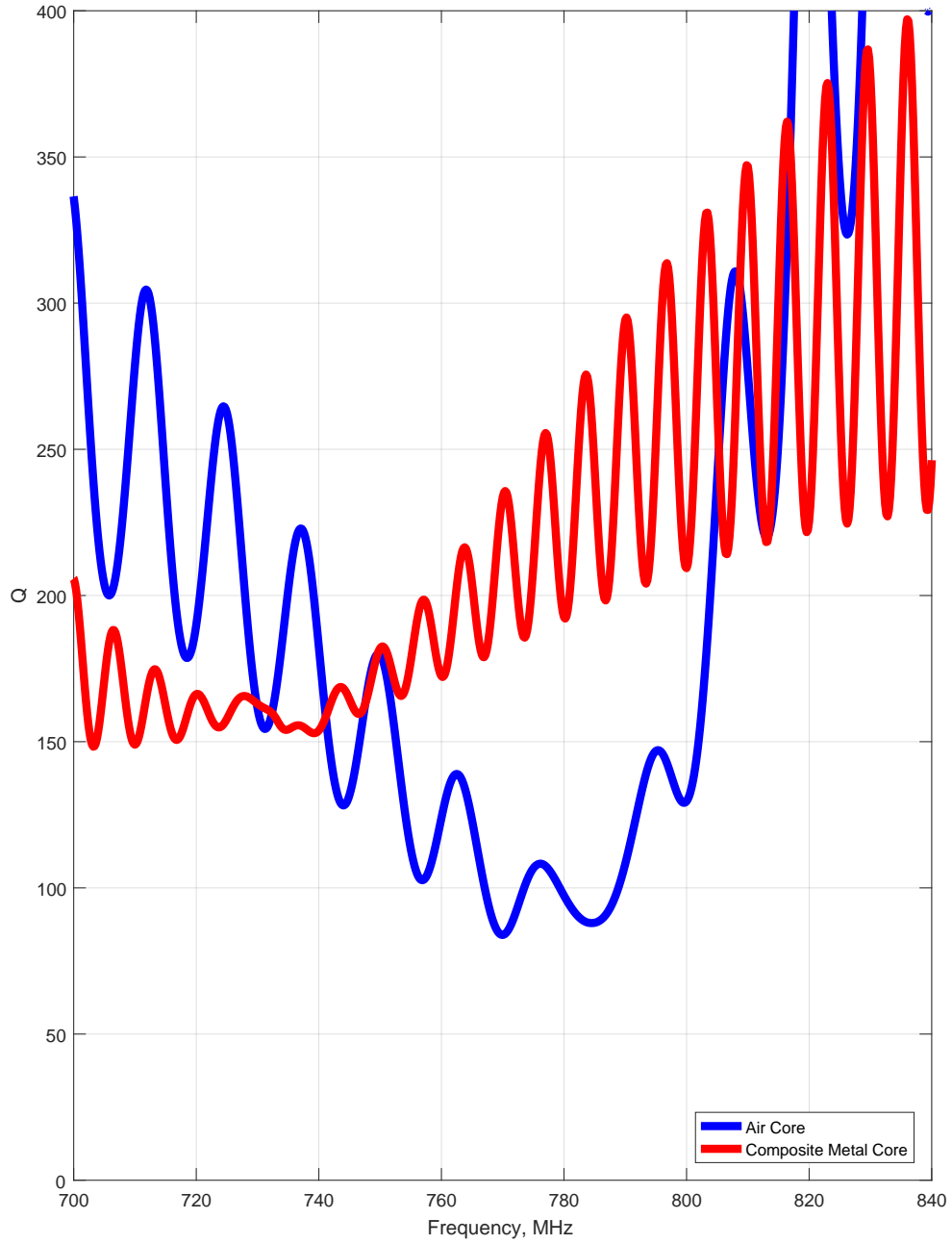
Figure 3.7: Quality factor for the PCB stack antenna with air core and composite metal core.

Although the antenna composite metal core with integral Faraday cage offers decreased antenna performance over that of the air core design, it offers greater utility for use in actual implementations. With the air core design, circuit board components and integrated circuits that are placed within the antenna core have the potential to impact antenna performance, such as the resonant frequency, radiation efficiency, and input impedance. This impact will be dependent upon the geometry and material properties of the components. The lack of shielding between the antenna and internal circuits also allows for the possibility of coupling unwanted signals onto the antenna. These concerns are mitigated with the addition of the Faraday cage to the antenna core by providing a shield between antenna elements and the housed components.

3.3 Discussion

Two different core compositions have been investigated for a hemispherical helix antenna constructed using a stack of PCBs as investigated in [30]. The purpose of this work was to understand the performance impacts of two different antenna core configurations, as compared with that of a solid dielectric antenna core, in order to realize performance improvements. Of the two core configurations investigated, the air core design showed an improvement in radiation efficiency of 4% with Q of $2.5Q_{min}$, which is the Chu lower bound [4].

In addition to the improvement to the antenna radiation efficiency, one significant benefit offered by the air core antenna is the opportunity to utilize the empty space within the antenna structure to house circuit components. The potential drawback is the impact to antenna performance, such as mutual coupling. As a means to mitigate this drawback, a antenna core design realization within an integral Faraday cage was also investigated. This provides a more practical realization of the space utilization within the antenna because the shield layer can mitigate the influence of intenral circuit components on the performance of the antenna, such as through the attenuation of radiated fields from noisy circuit components.

The composite metal core does impact the radiation efficiency of the antenna over that

of an air core, but it is believed that improvements can be realized through the optimization of antenna core geometry. Opportunities for future research work consists in refinement of the analytical methods used to quantify the antenna performance and the fabrication of prototype antennas in order to correlate the simulation data with laboratory measurements and evaluate the effectiveness of the composite metal core as a Faraday cage.

CHAPTER 4

A Sensitivity Analysis of a Printed Circuit Board Stack Based Hemispherical Helix Antenna

Submitted to the Transactions on Components, Packaging and Manufacturing Technology (CPMT) on April 8th, 2017.

The size of mobile phones, sensors, and a variety of other electronic devices continues to shrink as manufacturing processes advance to smaller scales. In contrast, the interconnectivity of devices has seen increased growth, with increasing applications for Internet of Things (IoT) devices. In some ways, these two technological trends compliment each other. As viewed from a electromagnetics perspective, as electronic devices decrease in physical size, their proportionate size to the wavelength of an electromagnetic wave, for a given frequency, also changes. Since the wavelength and frequency for an electromagnetic wave are inversely proportional, the physical size of circuits and devices becomes comparable to wavelengths of higher frequencies. For antenna design, this can be advantageous if the operational frequencies of the circuits and carrier frequencies of communications increase in a similar fashion, so as to ensure sufficient electrical length of the antenna elements for efficient operation. However, this is not the case for all devices, many of which are required to operate within the very high frequency (VHF) and ultra high frequency (UHF) ranges of spectrum bands [33]. For example, one new promising physical layer for low-power wide area networks (LPWAN), LoRa™, operates at frequencies below one gigahertz [34]. These LPWAN technologies are becoming attractive solutions for applications such as IoT and remote sensing, both of which can benefit from reductions of their spatial dimensions. With sub-gigahertz LPWAN psychical layers gaining momentum, the demand is likely to increase for advances in the field of electrically small antennas (ESA).

An antenna with spatial dimensions less than a tenth of the signal wavelength fits the general classification of being electrically small. Typical properties for ESAs consist of low

input resistance and high input reactance [3,35]. Much work has been done to determine the theoretical performance limits for ESAs and the figure of merit most often used is the quality factor, Q, which has an inverse relationship to the bandwidth of an antenna [4]. Different approaches have been taken to determine the lower bound for achievable antenna Q given a spatial volume allocated to the antenna. Two pioneering works for the determination of this lower Q bound are that of Wheeler [36] and Chu [4]. Both authors took the approach of modeling the antennas as equivalent circuits, but each took a slightly different approach to develop the circuit model. Wheeler used a cylinder to bound the antenna's volume, while Chu used a sphere and assumed an ideal condition of no internal stored energy within the sphere [29]. The Chu lower bound on Q is the most often used performance metric for an ESA and was later refined by Mclean into a succinct form given by [5]:

$$Q_{Chu} = \left(\frac{1}{(ka)^3} + \frac{1}{(ka)} \right) \tag{4.1}$$

Where k is the free space wavenumber of the electromagnetic wave and a is the radius of a sphere that bounds the volume afforded to the antenna. In order to apply the lower bound given in (4.1) to antennas with core materials with relative dielectric permittivity, ε_r, greater than one, we can use Wheeler's derivation for the minimum Q [29,37]:

$$Q_{Wheeler} = \left(1 + \frac{\varepsilon_r}{2} \right) \frac{1}{(ka)^3} \tag{4.2}$$

Within the field of ESAs, one popular antenna design has been shown to achieve Q values that approach the lower bound given by (4.1). The hemispherical helix antenna (HHA) aims to optimally utilize the space allocated by the spherical boundary of (4.1) by wrapping the antenna elements in a helical pattern that is conformal to a sphere or hemisphere. The design was first presented by Best [38] and subsequently thoroughly characterized in [20]. The resonance frequency and input impedance of the HHA can be adjusted through the number of helix arms and the number of helix turns. In addition, the HHA has demonstrated

the ability to achieve Q values within one and a half that of the limit in (4.1) [20]. As an ESA, the HHA has properties similar to that of a folded dipole antenna [39], including the radiation pattern, when the ground plan is small compared to the wavelength.

Since its first publication, the HHA has been influential in a number of subsequent ESA antenna designs, one of which expands upon the initial design by adding circular polarization [8] through equal radiated power of both transverse electric (TM_{10}) and transverse electric (TE_{10}) spherical modes. A novel design introduced in [40] consists of four-hemispherical arcs supporting helical wire coils. The antenna focuses only on exciting the TM_{10} mode to achieve a Q that is $2.3Q_{Chu}$.

A primary challenge with the HHA and its variants is the manufacturing of the antenna structure. Several approaches aim to address this problem. The authors in [41] and [42] investigated direct transfer patterning, but the fabricated antenna had low radiation efficiency attributed to the loss tangent of the dielectric substrate. Conductive ink printed onto a Duriod dielectric was used in [43] and measured results were compared to the minimum Q for spherical wire antennas, derived in [6]. A 3D printed antenna combined with copper paint was proposed in [18] and [17] which matched closely with results produced with solid wire-based designs. Similarly, 3D printing was used recently in [15] to replicate the HHA consisting of flat helical arms in order to increase the number of helical turns.

Most recently, the authors have proposed a new design methodology in [30, 44] which uses stacks of printed circuit boards (PCB) to create the desired antenna geometry. Copper traces and edge plating are then used to create the antenna elements which can be connected through the use of solder paste. To further increase the utility of the design, the authors have also investigated [26] different core geometries in order to maximize the volume afforded to the antenna. By creating a cavity within the antenna, the space within then becomes available to house circuit components. The PCB stack approach is not specific to the realm of ESAs, but its ability to utilize the volume within the antenna is well suited for applications where ESAs are sought.

The aim of this work is to understand design sensitivities of the PCB stack approach and the contributions are as follows: 1) quantified design parameter impacts on antenna performance, 2) determination of methods for tuning the antenna performance, and 3) proposed design enhancements to improve the efficacy of the PCB stack method. Because of the aforementioned desirable qualities of the HHA and fabrication difficulties, an HHA implementation will be the focus of this analysis. For PCB manufacturing, a number of manufacturing tolerances are of interest, especially the finished board thickness as it can be a large source of variability. In order to gain insight into the impact of these manufacturing variations on antenna performance, simulations will be run in which variation of the following antenna design parameters will occur:

- ground plane dielectric substrate thickness,

- antenna height,

- number of helix arms,

- number of helix turns,

- dielectric permittivity, and

- width of the antenna feed trace.

This analysis of antenna performance will be made using Sim4life SEMCAD X software [45]. Performance comparisons to prior works will be made, in addition to discussion on design choices to minimize performance impacts and opportunities for design enhancements.

4.1   Design and Analysis Methods

The HHA analyzed in this study was developed based upon the methods of [20] and [30]. A single-turn, four-arm HHA was chosen as the antenna to be studied due to its ability to achieve Q values that approach $1.5Q_{Chu}$ and achievable 50 ohm input impedance. The model

was developed according to the specifications in Table 4.1. The dielectric substrate chosen for both the ground plane PCB and the antenna PCBs was Rogers RO3003, primarily due to its low loss tangent. The thickness of each PCB within antenna stack was 1.591 millimeters in order to set the PCB stack height equal to the radius of the imaginary boundary sphere. The copper thickness is set to 71.1 micrometers for all copper entities. The ground plane for the antenna is constructed using a separate two-layer PCB, whose top layer consists of a feed trace for the antenna and three short traces with vias that connect to the contiguous ground plane on the bottom layer. The assembled antenna is shown in Fig. 4.1 and was tuned to resonance by adjusting the substrate thickness of the ground plane PCB.

Table 4.1: Antenna specifications for the four-arm hemispherical wire antenna

Number of Turns	Antenna Radius (mm)	Ground Plane Radius (mm)	Resonant Frequency (MHz)	Number of Layers	ka
1	19.1	30	775	12	0.310
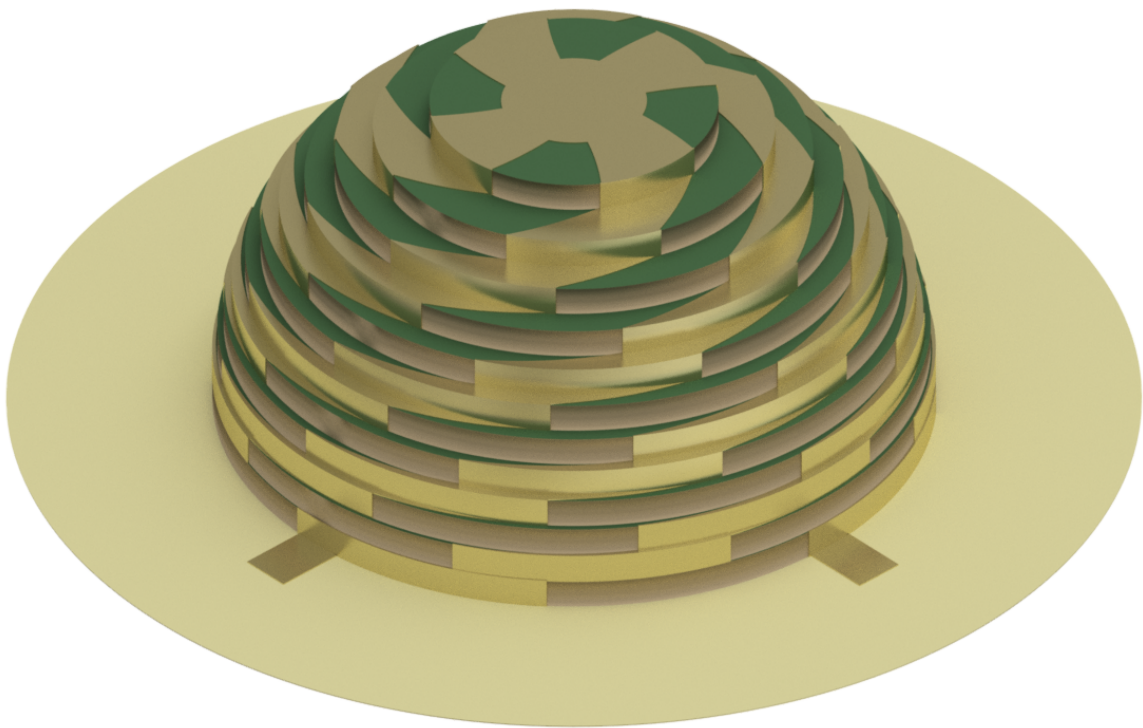
Figure 4.1: A four-arm hemispherical helix antenna created through a stack of 12 PCBs.

Figure 4.2: Two, three, five, and six arm hemispherical helix antennas created using a stack of 24 PCBs.

With the base antenna configuration established and simulated, numerous parametric adjustments were made to the antenna to understand the antenna's sensitivity to sources of manufacturing process variations. For standard PCB manufacturing, the PCB thickness is the largest source of uncertainty, with a typical tolerance variation of 10 percent [46]. As part of the sensitivity analysis performed on the antenna design of Table 4.1, four additional antenna models were created in order to evaluate the impact of adding additional helix arms. These antennas were based on a stack of 24 PCBs in order to increase the spatial resolution and separation of the helix arms for the five and six arm configurations. These antenna designs were otherwise consistent with the specifications in Table 2.2 and are shown in Fig. 4.2.

4.2 Results

4.2.1 Ground Plane Dielectric Substrate Thickness

The thickness of the dielectric ground served as the primary mechanism for tuning the antenna to achieve a 50 ohm input impedance at its resonant frequency. As can be seen in Fig. 4.3, a 50 ohm input impedance is achieved for the antenna when the ground plane substrate thickness is 0.12 millimeters. The dielectric thickness controls the capacitive loading of the antenna through a shunt capacitance to the ground plane, which works to compensate for the high reactance of the ESA. This technique was also utilized as an effective tuning mechanism in [47], which also noted its minimal impact to the antenna Q. The Q values listed in Table 4.2 support this finding.

Figure 4.3: S_{11} Smith chart plot of the four-arm hemispherical helix antenna normalized complex reflection coefficient for different thicknesses of the dielectric substrate above the ground plane. The markers indicate the location of the antenna's resonant frequency on the Smith chart. Decreasing the thickness of the dielectric substrate causes an increase in the parasitic capacitance, which combined with input resistance increase of the four-helical arms, allows the the antenna impedance to reach 50Ω.
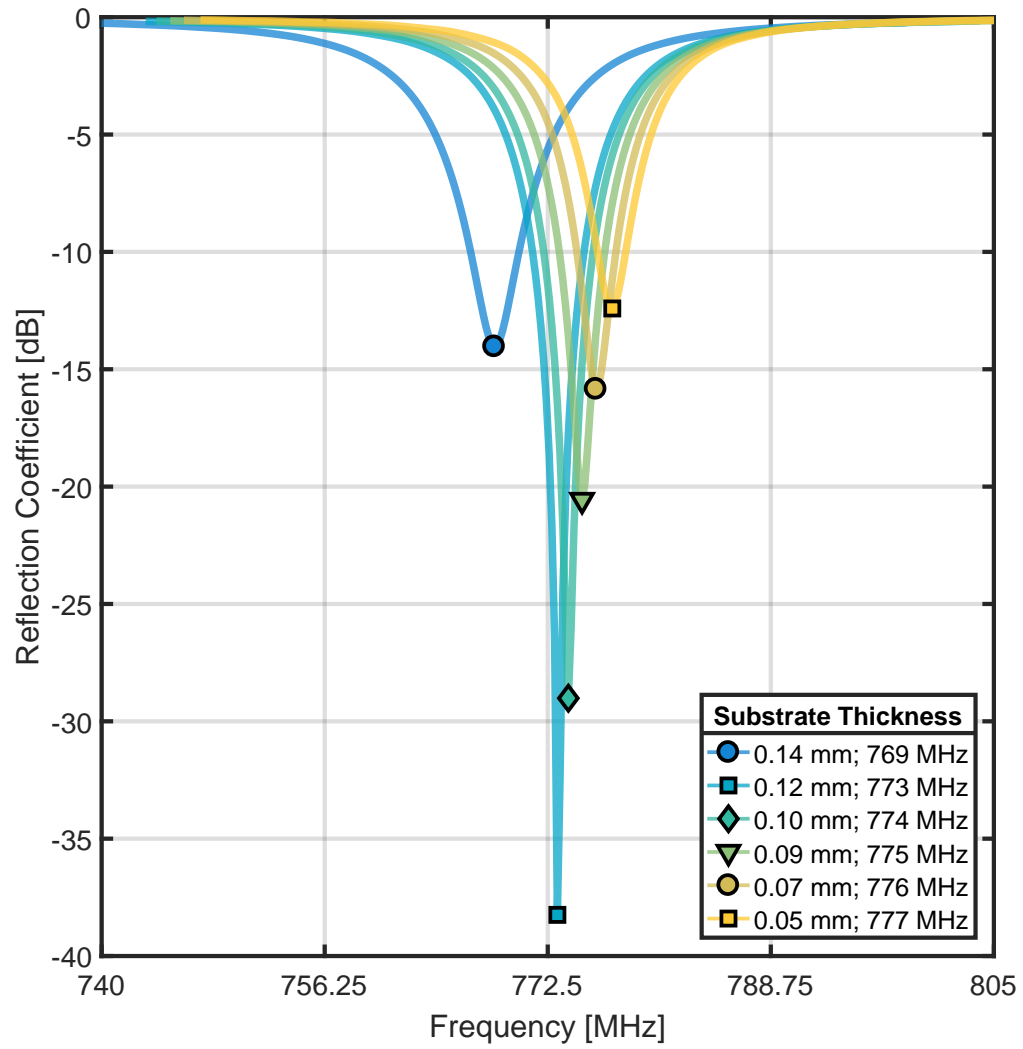
Figure 4.4: S$_{11}$ reflection coefficient variation of the four-arm HHA for different ground plane dielectric substrate thicknesses.
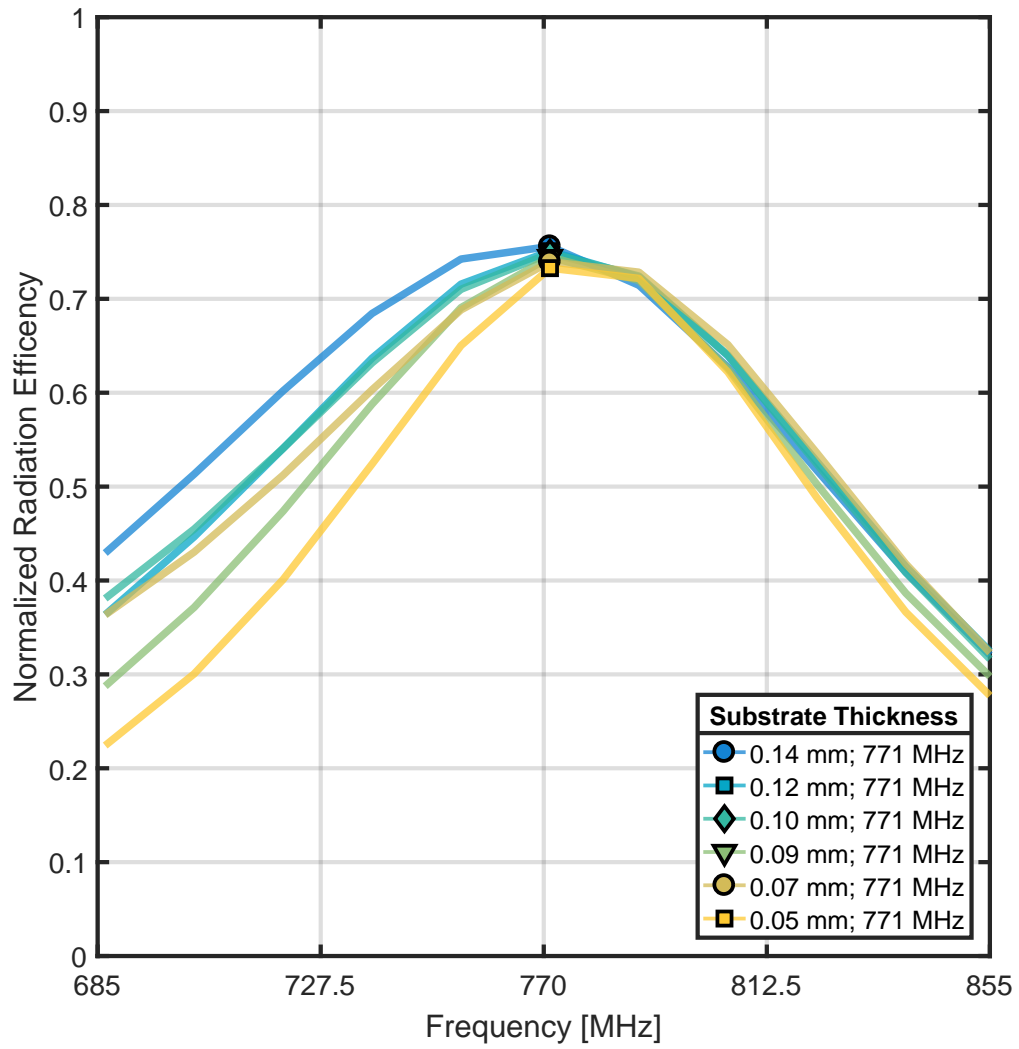
Figure 4.5: Radiation efficiency of the of the four-arm HHA for different ground plane dielectric substrate thicknesses.

The radiation efficiency is shown in Fig. 4.5 for the antenna and averages about 74 percent across the six dielectric thickness values, which is lower than reported in [20], likely due to the dielectric losses associated with the dielectric core of the antenna. However, radiation efficiency is comparable to other designs implemented on dielectric substrates, such as the 71 percent reported in [47] for a ka of 0.29 and greater than the 35.2 percent measured in [42]. It should be noted that the radiation efficiency and directivity figures in this analysis were coarsely sampled, which is the reason for the discrepancy in frequency values between those plots and the values reported for the reflection coefficient and input impedance.

It's interesting and worth noting the difference in bandwidth between the reflection coefficient in Fig. 4.4 and the radiation efficiency in Fig. 4.5. Due to the resonant nature of the HHA, the impedance bandwidth is exceedingly narrow but could be improved through the use of a broad-band impedance matching network, as in [48], which could be integrated into the antenna's feed trace or bottom PCB with PCB antenna stack.
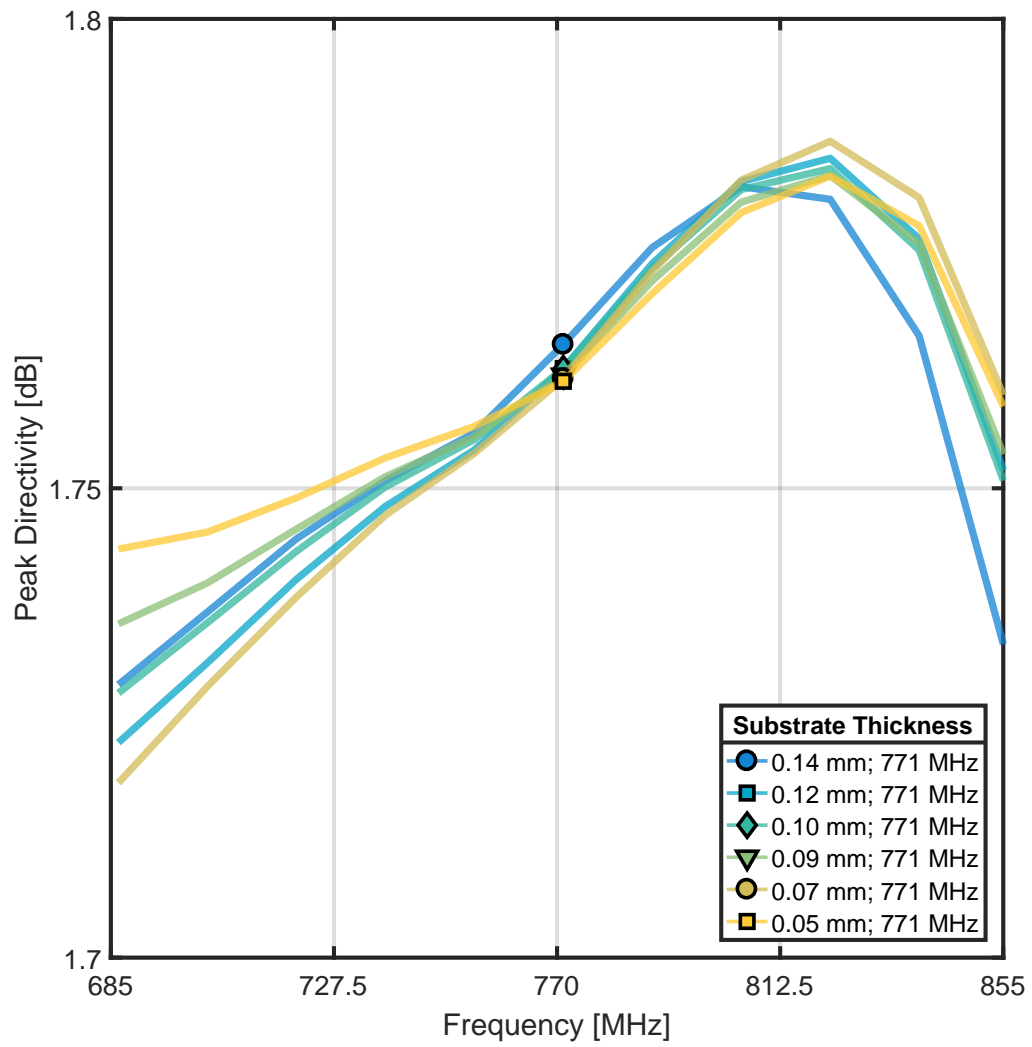
Figure 4.6: Directivity of the four-arm HHA for different ground plane dielectric substrate thicknesses.

Table 4.2: Quality factor of the four-arm HHA for different ground plane dielectric substrate thicknesses.

Substrate Thickness (mm)	Resonant Frequency (MHz)	ka	Q	$\frac{Q}{Q_{Wheeler}}$	$\frac{Q}{Q_{Chu}}$
0.14	768.6	0.31	147	1.7	3.9
0.12	773.2	0.31	141.3	1.7	3.8
0.1	774	0.31	140.2	1.7	3.8
0.09	775	0.31	138.5	1.7	3.8
0.07	776	0.31	136.3	1.6	3.7
0.05	777.2	0.31	133.8	1.6	3.7

The antenna directivity resembles that of a dipole antenna, achieving an average of 1.76 decibels across the dielectric thickness variations, as shown in Fig. 4.6. A peak gain of -1.63 decibels was measured in [42], which can be converted to a directivity of roughly 2.9 decibels using the measured radiation efficiency. The HHA's peak directivity has remained relatively constant in the results of this analysis has been omitted from other discussions for brevity.

The antenna Q does not achieve the $1.5Q_{Chu}$ value that the HHA design has been shown to be capable of, likely due to the dielectric loading of the PCB substrate, according to (4.2). The average Q is $3.8Q_{Chu}$ and $1.7Q_{Wheeler}$, which is higher than the reported Q in [14,15,20], but comparable to the Q value reported in [47] for a ka of 0.29.

4.2.2   Antenna Height

The finished thickness stability of a PCB varies by manufacturer and is a function of the materials used and their coefficient of thermal expansion [49]. This specification varies by manufacturer and its impact is dependent upon the geometry of the antenna. With a modeled PCB thickness of 1.591 millimeters, a finished thickness tolerance of 10 percent is typical for a standard PCB build [46], which results in maximum and minimum heights of 21.01 and 17.19 millimeters. The overall height of the HHA antenna is varied, while holding all other design parameters constant. A ground plane dielectric substrate thickness of 0.10 millimeters was chosen based upon the results in the previous section.

The variation of the antenna height predominately impacts the height of the copper plated edges of the PCBs, which translates to a change in the helix arm width and in turn impacts the resistance of the antenna element. At an antenna height of 17.19 millimeters, the input resistance increases to a value of 57.1 ohms and decreases to 45.1 ohms at a height of 21.01 millimeters. The impedance change is illustrated in Fig. 4.7, and the associated impact on the resonant frequency in Fig. 4.8. The resonant frequency of the antenna changes from a minimum value of 748 MHz to a maximum value of 813 MHz, which is significant for a narrow-band, resonant antenna.
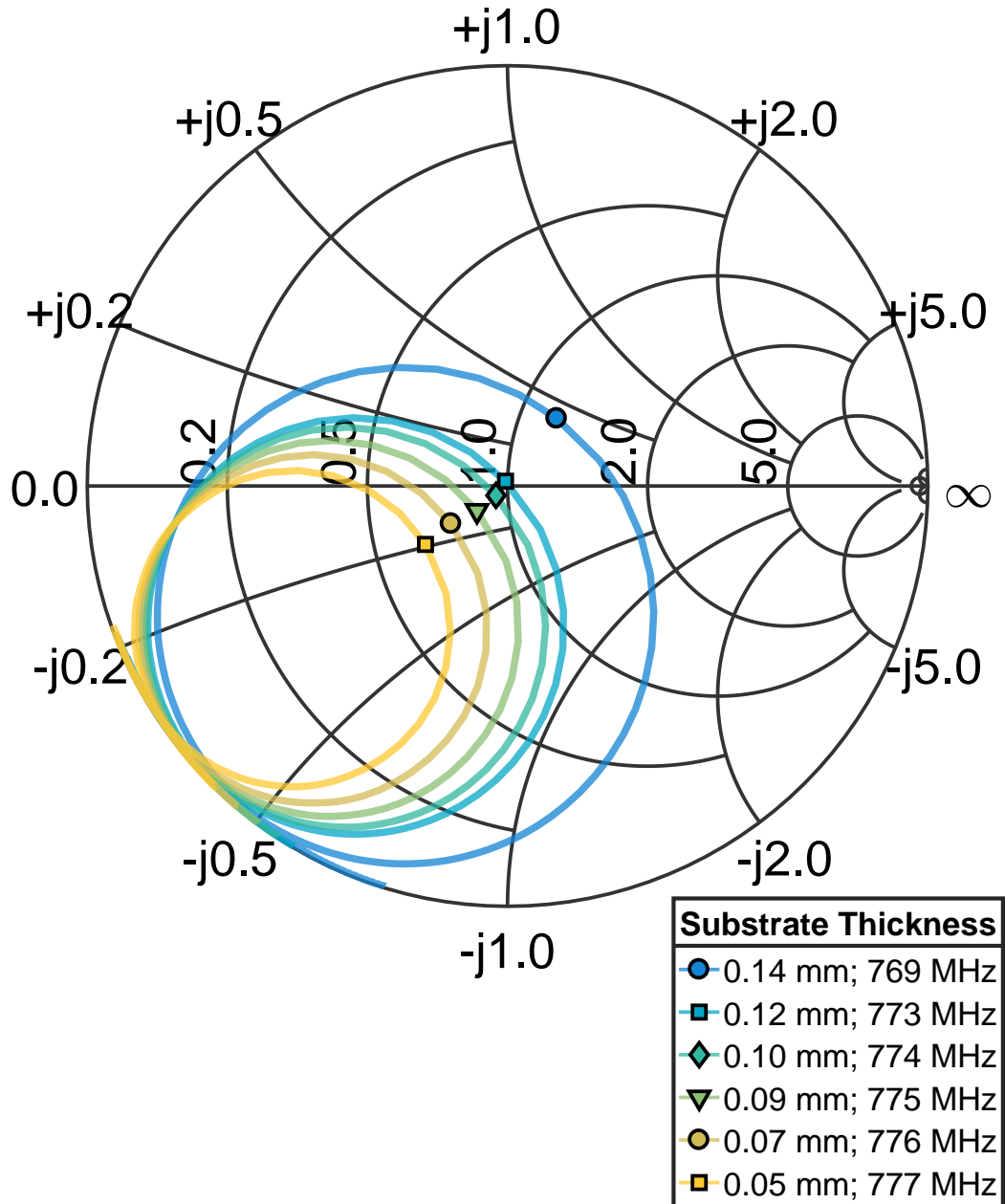
Figure 4.7: S$_{11}$ Smith chart plot of the four-arm hemispherical helix antenna normalized complex reflection coefficient for changes in HHA height.

Figure 4.8: S$_{11}$ reflection coefficient variations for changes in HHA height.

Table 4.3: Radiation efficiency variations for changes in HHA height.

Antenna Height (mm)	Resonant Frequency (MHz)	ka	η (%)
17.19	754.2	0.30	68
18.46	754.2	0.30	73
19.74	805.1	0.32	80
21.01	805.1	0.32	82

Table 4.4: Quality factor variations for changes in HHA height.

Antenna Height (mm)	Resonant Frequency (MHz)	ka	Q	$\frac{Q}{Q_{Wheeler}}$	$\frac{Q}{Q_{Chu}}$
17.19	747.8	0.30	170.9	1.8	4.2
18.46	761.6	0.30	152.4	1.7	3.9
19.74	801.6	0.32	133.1	1.8	4.0
21.01	813.2	0.33	116.8	1.6	3.6

The radiation efficiency, η, of the antenna decreases to 68 percent and increases to 82 percent for the minimum and maximum antenna heights, as shown in Table 4.3. The antenna height variations effectively changed the ka product for the HHA antenna. As also observed in [47], the change in radiation efficiency is proportional to the change in the ka product. The change in Q values show a trend of being inversely proportional to the ka product, as shown in Table 4.4.

4.2.3   Number of Helix Arms

To analyze the effect of changing the number of helix arms, the number of PCB layers was increased to 24 in order to provide greater spatial resolution of the helix arms and to reduce capacitive coupling between adjacent helix arms. The total number of helix arms was varied from 2 to 6 and the impact to resonant frequency behavior was significantly more noticeable than as reported in [20]. As shown in Fig. 4.9 and 4.10, the resonant frequency decreases as the number of turns decrease. It is suspected that the dielectric loading of the antenna is responsible for the increased sensitivity to the number of helix arms and difference in impedance behavior. The impedance loop behavior better matches the results in [47], which is also loaded with dielectric material.

The radiation efficiency in Fig. 4.11 decreases with the resonant frequency of the antenna, due to the associated decrease in ka product. In turn, the Q in Table 4.5 increases with decreasing ka, as discussed in the previous section. However, the proximity of Q to the lower bounds remains relatively unaffected.

Figure 4.9: S$_{11}$ Smith chart plot of the four-arm hemispherical helix antenna normalized complex reflection coefficient for changes in the number of helix arms.

Figure 4.10: S$_{11}$ reflection coefficient variations for changes in the number of helix arms.
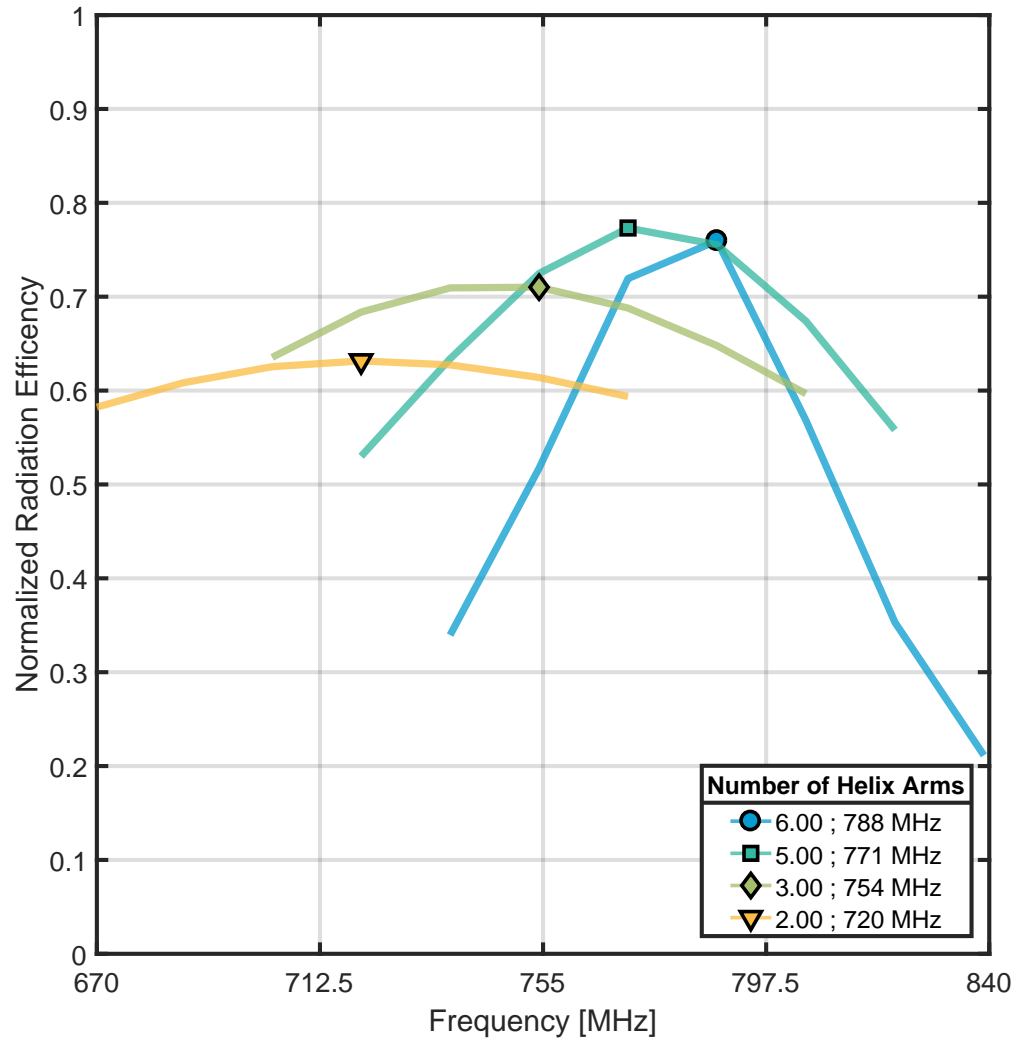
Figure 4.11: Radiation efficiency variations for changes in the number of helix arms.

Table 4.5: Quality factor variations for changes in the number of helix arms.

Number of Helix Arms	Resonant Frequency (MHz)	ka	Q	$\frac{Q}{Q_{Wheeler}}$	$\frac{Q}{Q_{Chu}}$
6	783	0.31	136.1	1.7	3.8
5	776.2	0.31	142.1	1.7	3.9
3	746.6	0.3	163.7	1.7	4
2	716	0.29	185.9	1.7	4

4.2.4   Number of Helix Turns

In order to evaluate the impact of adjusting the number of turns for the helix arms, the number of PCB layers was set to 24, as was done for the number of helix arms analysis. The reason for the change was to increase the distance between adjacent helical arms so as to minimize the effects of parasitic coupling between arms so as to not skew the results of the analysis through the addition of another variability source. The changing of helix turns results in coarse adjustment of the resonant frequency of the antenna, as shown in Fig. 4.13, which is in agreement with the results of [20]. However, changes to the input impedance of the antenna are minor, which allows for a fine adjustment of the antenna's input impedance through varying the number of helix turns. This property could be leveraged and used to integrate an impedance tuning feature into the structure of the HHA PCB stack. If the lowest PCB in the antenna stack is fixed in position, relative to the ground plane PCB, then the remaining PCB stack structure could be rotated, changing the amount of overlap for PCB plated edges between the bottom layer and one adjacent to it. This would provide a means to effectively adjust the number of helix turns for the HHA and tune the resonant frequency of the antenna.
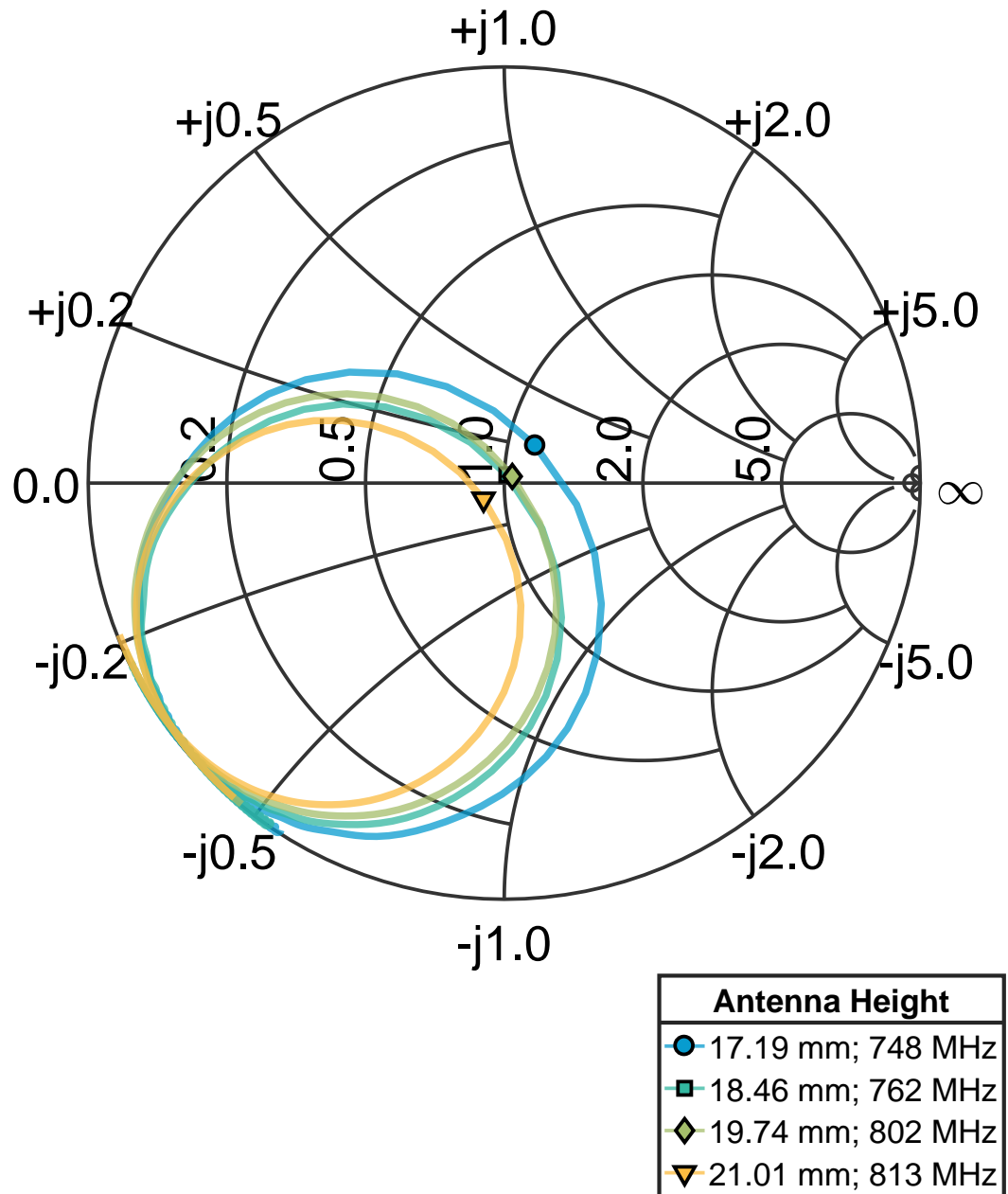
Figure 4.12: S$_{11}$ Smith chart plot of the four-arm hemispherical helix antenna normalized complex reflection coefficient for changes in the number helix turns.
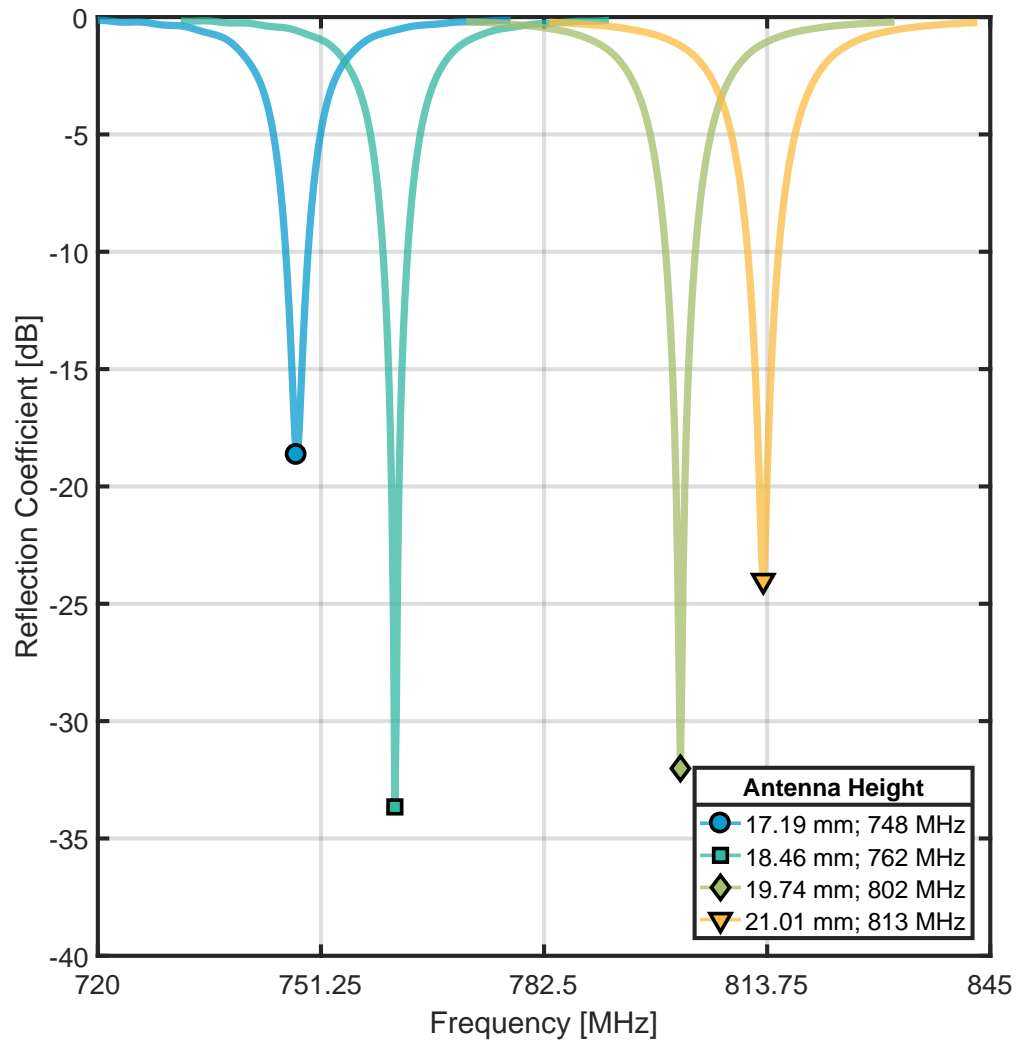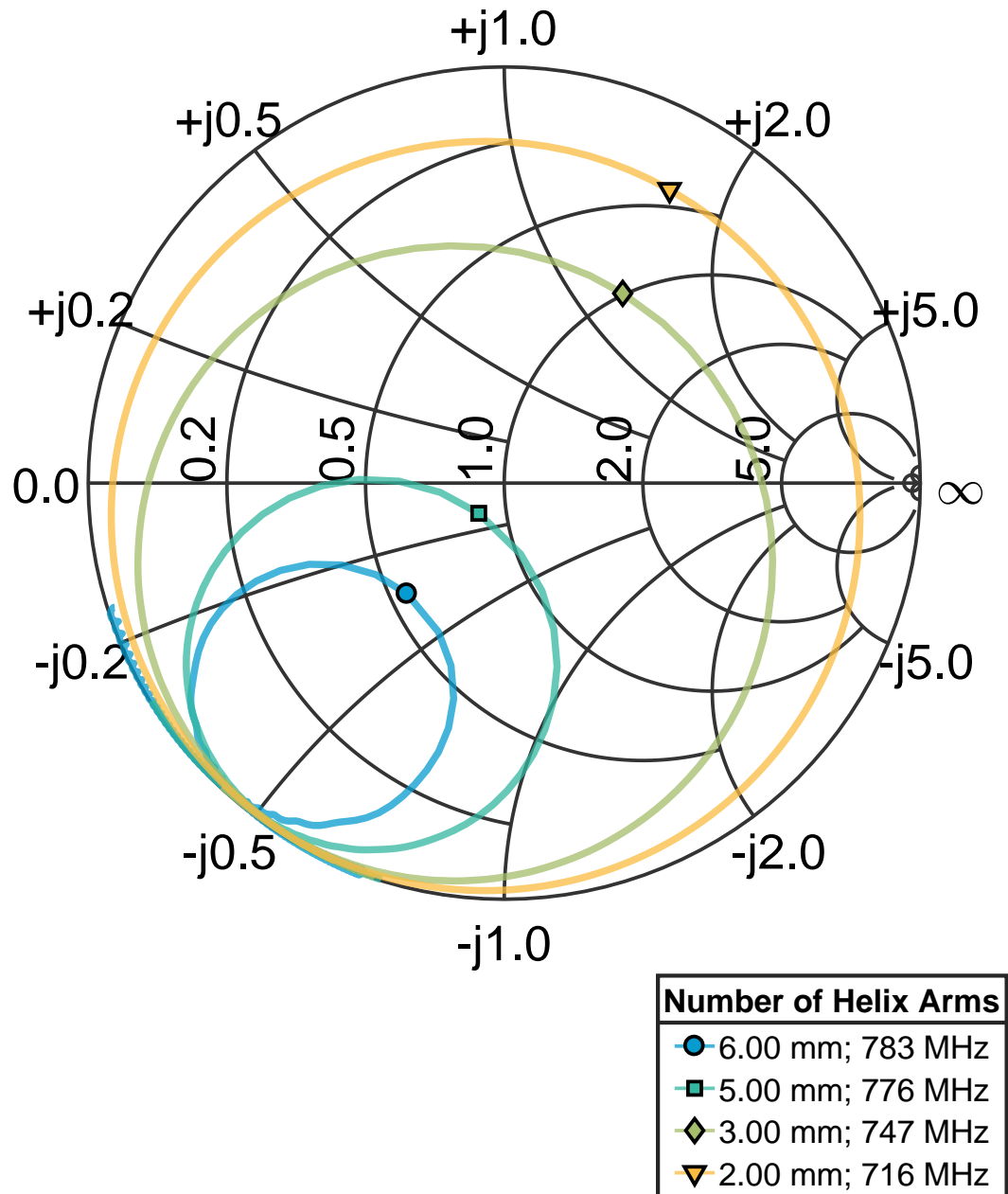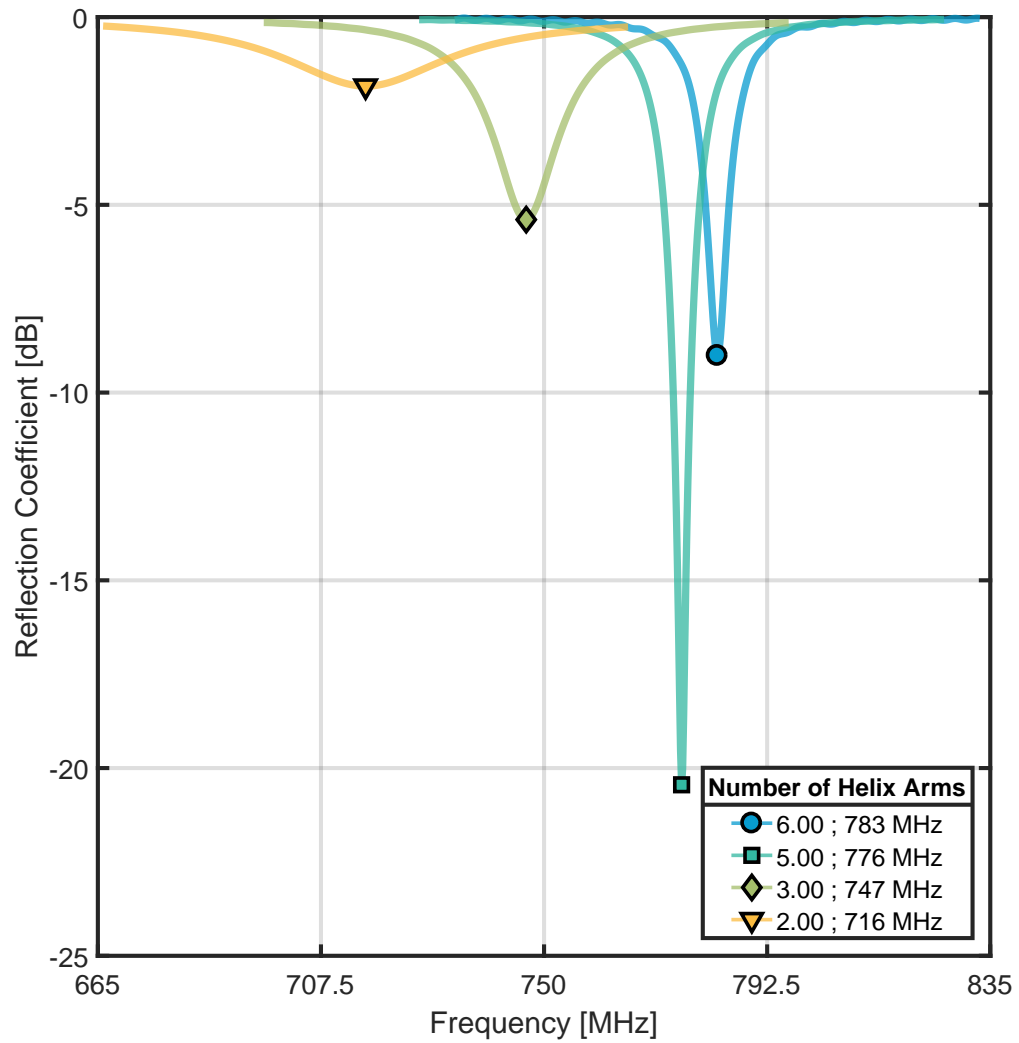
Figure 4.13: S$_{11}$ reflection coefficient variations for changes in the number of helix turns.

Table 4.6: Radiation efficiency variations for changes in the number of helix turns.

Antenna Height (mm)	Resonant Frequency (MHz)	ka	η (%)
0.85	872.9	0.35	81
0.91	822	0.33	79
1.09	703.4	0.28	70
1.15	686.4	0.27	66

Table 4.7: Quality factor variations for changes in the number of helix turns.

Number of Helix Turns	Resonant Frequency (MHz)	ka	Q	$\frac{Q}{Q_{Wheeler}}$	$\frac{Q}{Q_{Chu}}$
0.85	873.2	0.35	111.8	1.9	4.2
0.91	824.2	0.33	127.6	1.8	4.1
1.09	711.2	0.28	171.9	1.6	3.7
1.15	682.4	0.27	181.3	1.5	3.4

The radiation efficiency is listed in Table 4.6 and the Q values are listed in Table 4.7. The variation in the number of helix turns corresponds to minimum and maximum ka values of 0.27 and 0.35 respectively. The Q values range from $1.5Q_{Wheeler}$ and $3.4Q_{Chu}$ for a ka of 0.27 to $1.9Q_{Wheeler}$ and $4.2Q_{Chu}$ for a ka of 0.35. As observed previously, the radiation efficiency is proportional to ka, with a radiation efficiency of 66 percent achieved for a resonant frequency of 682 megahertz.

4.2.5 Dielectric Permittivity

The dielectric substrate used for these simulations is Rogers RO3003 and was selected because of its low loss tangent and stable dielectric properties over frequency. The dielectric constant was varied over a range much greater than the advertised tolerance of RO3003. This was done in order to gain a better understanding of the trade offs associated with materials

Table 4.8: Radiation efficiency variations for changes in the dielectric permittivity of the PCB substrate.

Antenna Height (mm)	Resonant Frequency (MHz)	ka	η (%)
1.5	906.8	0.36	77
2.5	839	0.34	82
3.5	754.2	0.30	74
4.5	686.4	0.27	68

of different dielectric permittivites. The dielectric conductivity remained unchanged at a value of 0.00022 Siemens per meter.

The change in resonant frequency of the antenna is inversely proportional to the change in dielectric permittivity, which is to be expected due to the reduced electrical wavelengths of waves propagating within the dielectric medium. As the relative permittivity increases, the wavelength decreases, which in turn increases the effective electrical length of the antenna. This behavior can be observed through changes in the antenna's resonant frequency and is illustrated in Fig. 4.15, with impedance variations in Fig. 4.14.

Changing the dielectric permittivity also has a dramatic impact on the ka values for the antenna, which have minimum and maximum values of 0.27 and 0.36. Of particular interest is the impact on the radiation efficiency and the Q values. In looking at Table 4.8, it can be seen that the radiation efficiency for a ka of 0.27 is 68 percent and 82 percent for a ka of 0.384. In looking at Table 4.9, the Q values range from $1.9Q_{Wheeler}$ and $4.3Q_{Chu}$ for a ka of 0.28 to $2.1Q_{Wheeler}$ and $4.5Q_{Chu}$ for a ka of 0.36. Note that (4.2) is only plotted for $\varepsilon_r = 3.0$, but the previously presented $Q_{Wheeler}$ values were calculated using the appropriate ε_r.

4.2.6 Feed Trace Width

As utilized in [47], the feed trace for the HHA is an effective mechanism for tuning the input impedance of the antenna. The nominal width of the trace is 2.8 millimeters with a
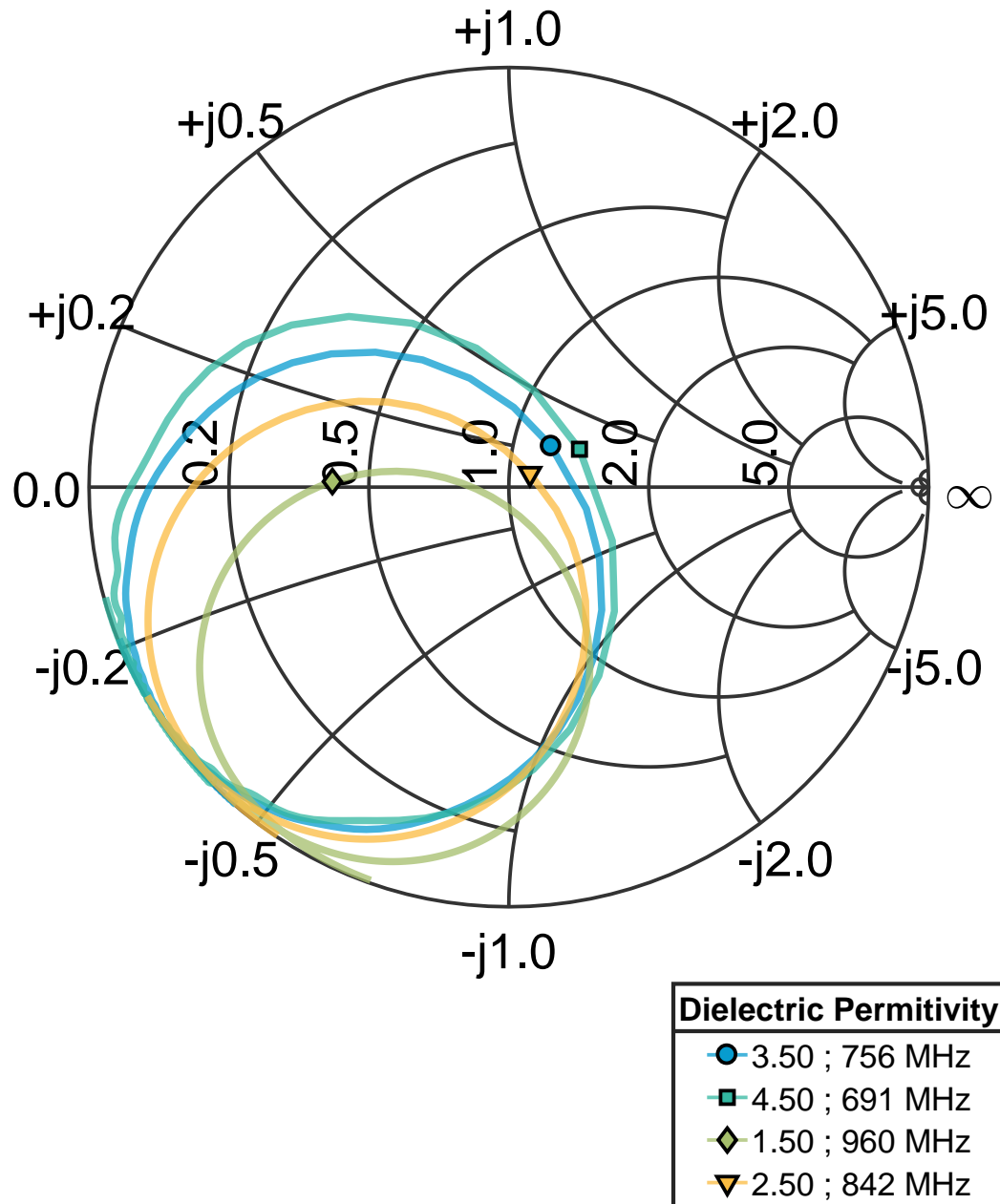
Figure 4.14: S$_{11}$ Smith chart plot of the four-arm hemispherical helix antenna normalized complex reflection coefficient for changes in the dielectric permittivity of the PCB substrate.

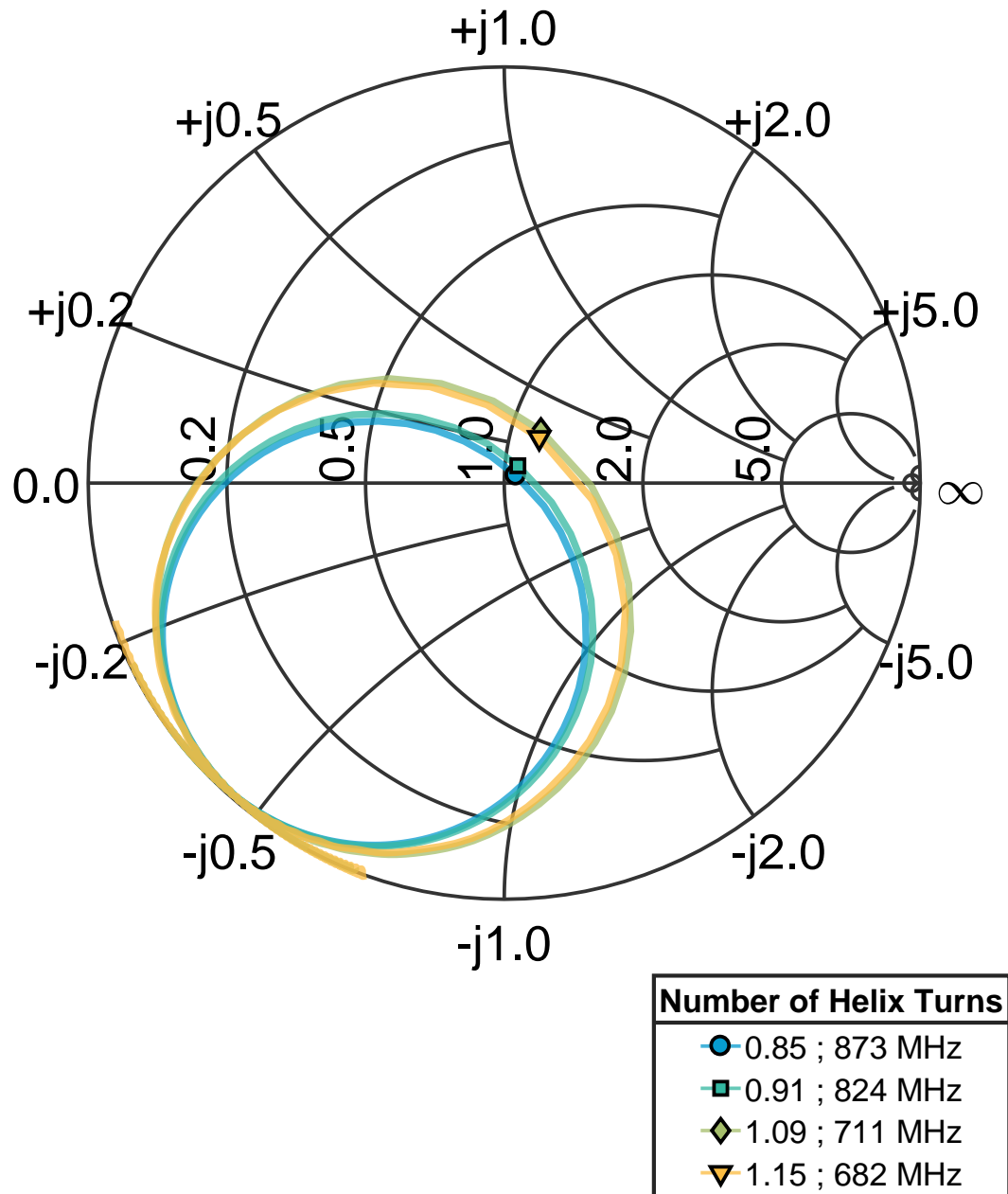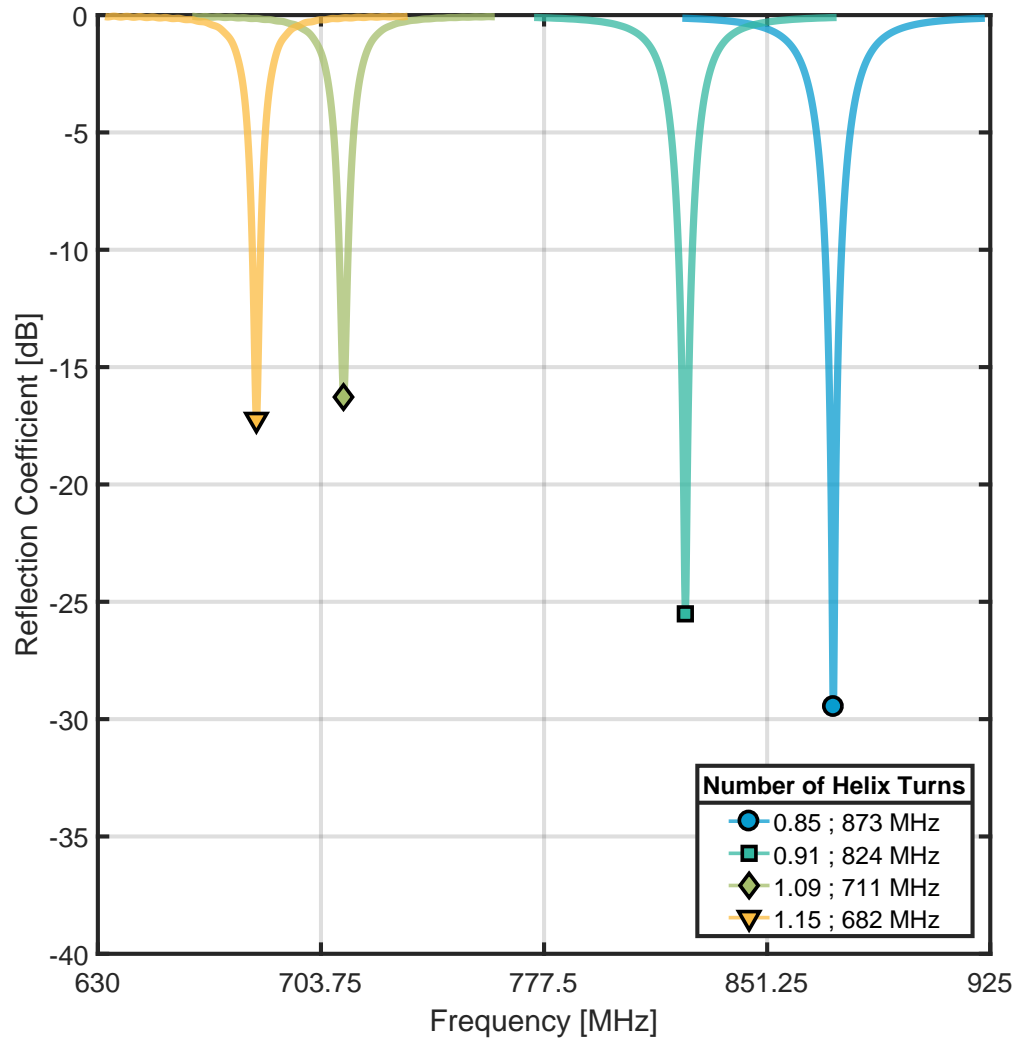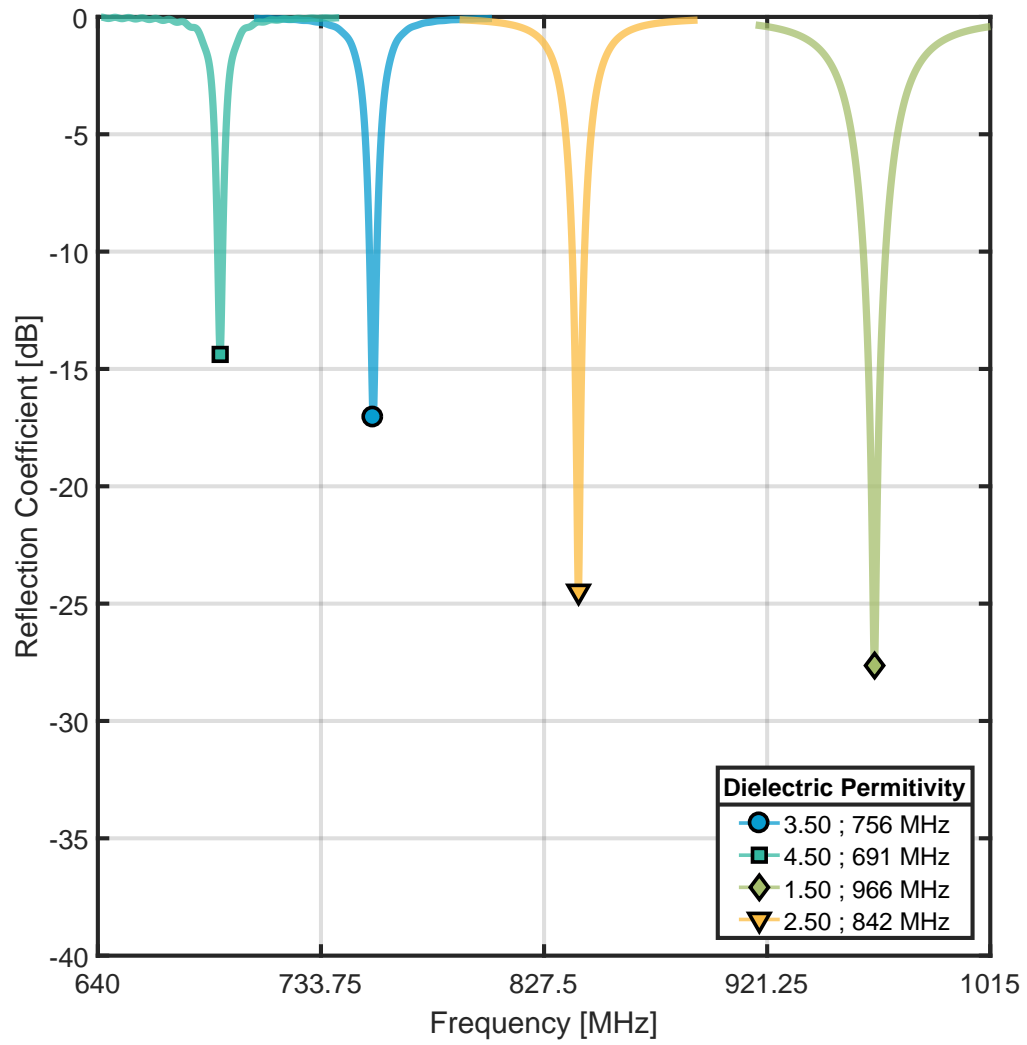Figure 4.15: S$_{11}$ reflection coefficient variations for changes in the dielectric permittivity of the PCB substrate.

Table 4.9: Quality factor variations for changes in the dielectric permittivity of the PCB substrate.

Dielectric Permittivity	Resonant Frequency (MHz)	ka	Q	$\frac{Q}{Q_{Wheeler}}$	$\frac{Q}{Q_{Chu}}$
1.5	899.8	0.36	109.9	2.1	4.5
2.5	842.0	0.34	115.5	1.8	4.0
3.5	755.6	0.3	171.3	1.9	4.3
4.5	691.4	0.28	218.8	1.9	4.3

constant length of 3.82 millimeters.

The increase in trace width causes a proportional increase in the capacitive loading of the antenna, illustrated in Fig. 4.16, similar to the effect of reducing the thickness of the ground plane dielectric substrate, as shown in Fig. 4.3. The resonant frequency is negligibly impacted by feed trace width adjustments, which is desirable when trying to impedance match the antenna.

The radiation efficiency achieves a average value of 77 percent and is minimaly impacted by the feed trace width, as can be seen in Fig. 4.18. The Q values shown in Table 4.10 exhibit similar behavior and achieve values of $1.7Q_{Wheeler}$ and $3.9Q_{Chu}$ for a ka of 0.31.

Due to these negligible impacts, adjustments to the antenna feed trace are well-suited for tuning of the input impedance for the antenna, although the tuning range is limited to primarily adding or removing capacitive reactance.
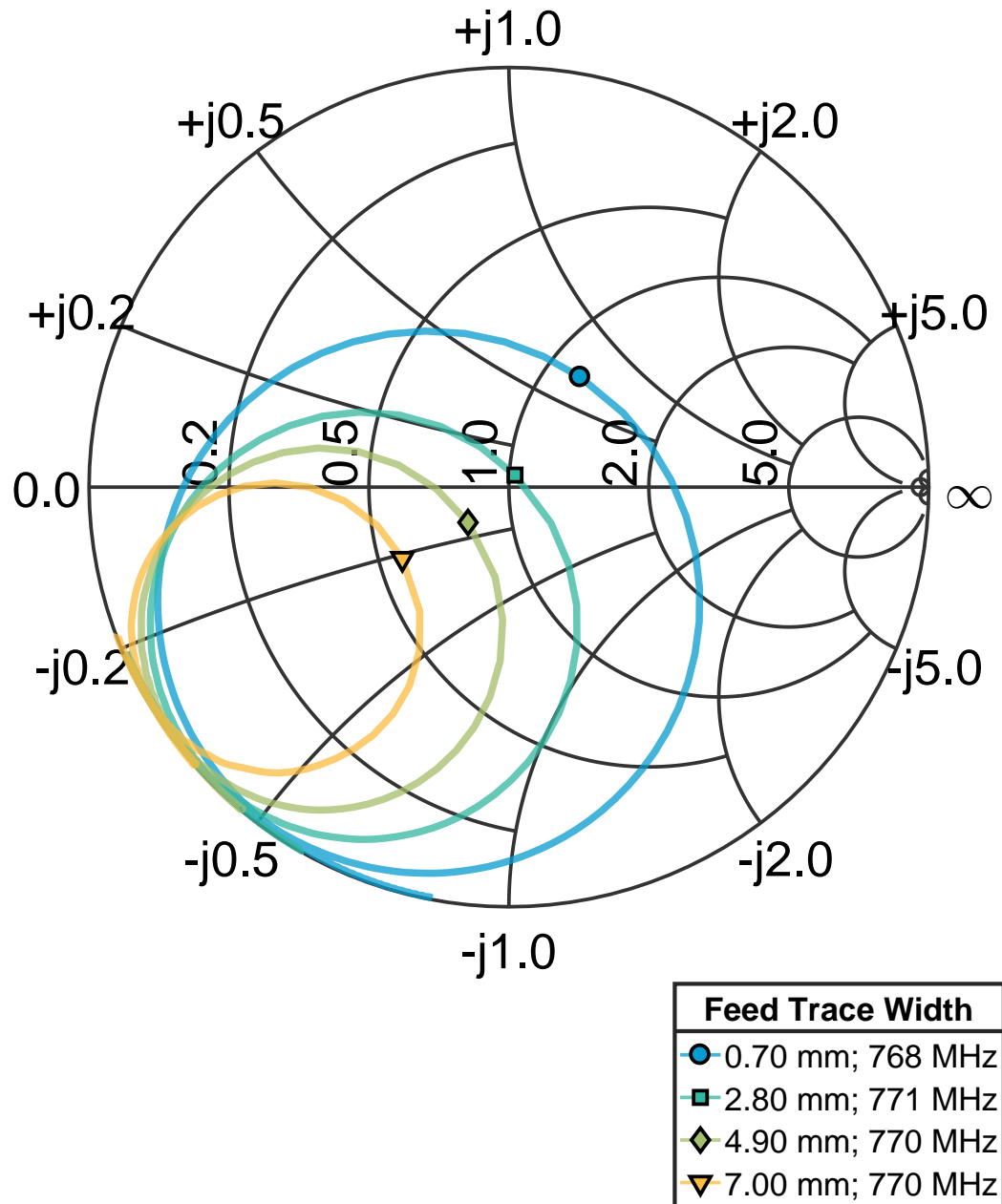
Figure 4.16: S_{11} Smith chart plot of the four-arm hemispherical helix antenna normalized complex reflection coefficient for changes in the width of the feed trace for the antenna.
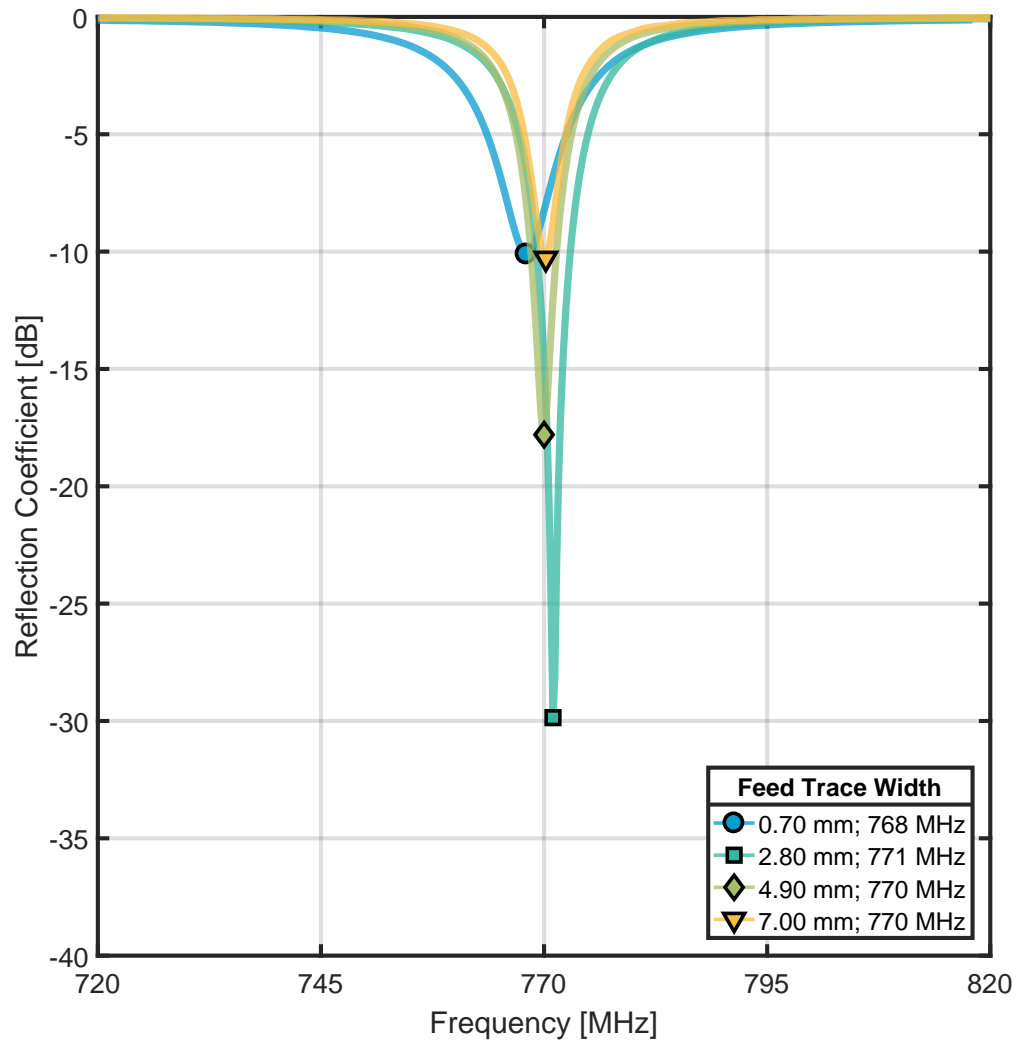
Figure 4.17: S_{11} reflection coefficient variations for changes in the width of the feed trace for the antenna.
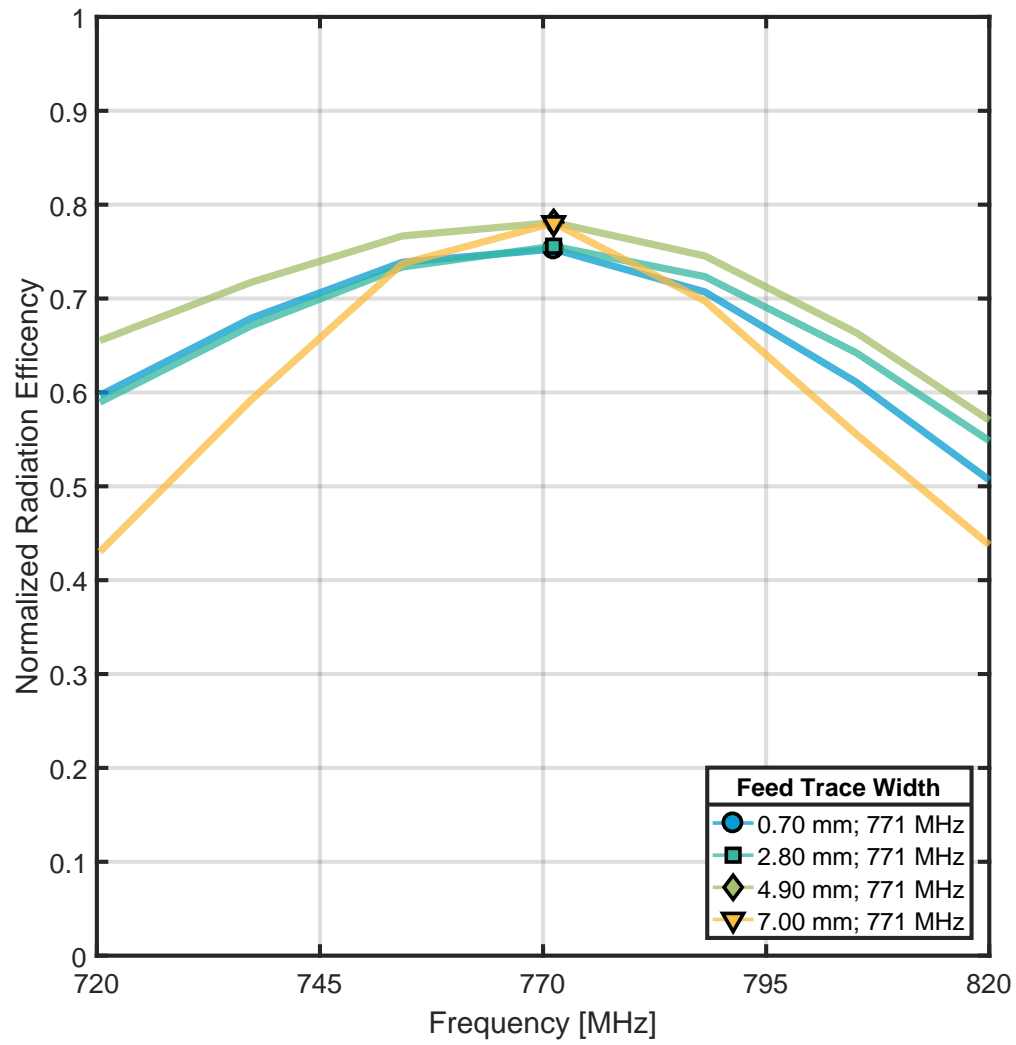
Figure 4.18: Radiation efficiency variations for changes in the width of the feed trace for the antenna.
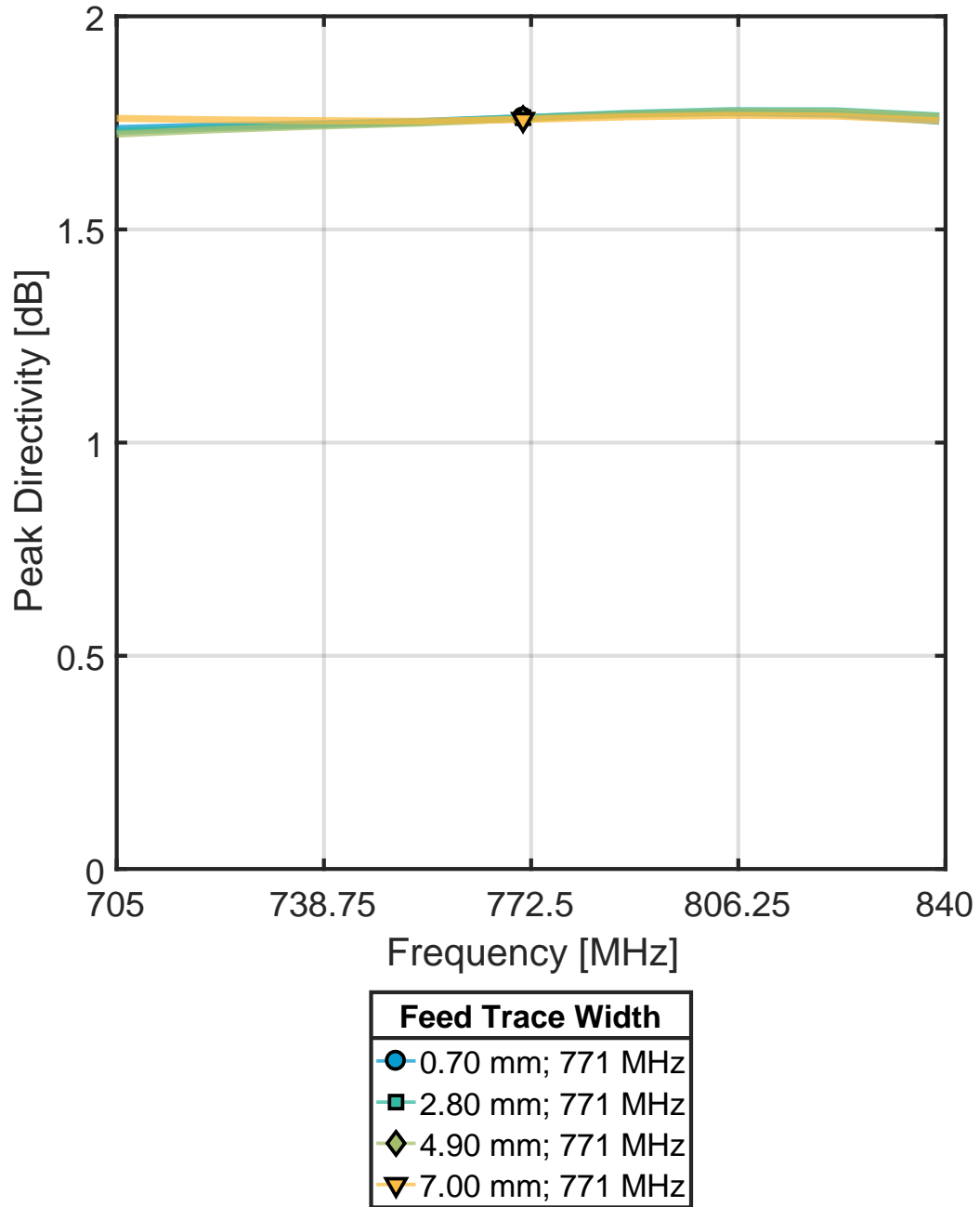
Figure 4.19: Directivity variations for changes in the width of the feed trace for the antenna.

Table 4.10: Quality factor variations for changes in the width of the feed trace for the antenna.

Feed Trace Width (mm)	Resonant Frequency (MHz)	ka	Q	$\frac{Q}{Q_{Wheeler}}$	$\frac{Q}{Q_{Chu}}$
0.7	768	0.31	148.6	1.7	3.9
2.8	771	0.31	143.1	1.7	3.8
4.9	770	0.31	146.3	1.7	3.9
7.0	770.2	0.31	143.1	1.7	3.8

Table 4.11: Summary of the one sigma standard deviations for antenna performance to parameter variations.

Parameter	Parameter Change	Resonant Frequency (MHz)	ka	η (%)	$\frac{Q}{Q_{Wheeler}}$	$\frac{Q}{Q_{Chu}}$
Dielectric Spacing	0.03 mm (3%)	3.0	0.001	0.8	0.03	0.08
Antenna Height	1.64 mm (8.5%)	31.3	0.013	6.4	0.09	0.23
# of Helix Arms	1.8	30.7	0.012	6.4	0.04	0.11
# of Helix Turns	0.14 (14%)	90.7	0.036	7.3	0.2	0.38
Dielectric Permittivity	1.29 (43%)	92.1	0.037	6.0	0.12	0.24
Feed Trace Width	2.71 mm (100%)	1.3	0.001	1.5	0.02	0.06

4.3   Conclusion

This work has investigated an alternative antenna design methodology which utilizes a PCB stack to create an antenna. The focus of the analysis was on understanding design parameter sensitivities to sources of variation within the PCB manufacturing process. From the data developed in this analysis, opportunities have been proposed for leveraging the PCB implementation to make unique design enhancements, which are not afforded to traditional wire-based fabrication methods. An electrically small HHA was chosen as the candidate antenna design for this study due to its prevalence in the realm of ESAs and challenging geometry to fabricate.

The summary of the chosen parameter variations on antenna performance is presented in Table 4.11. The impact of most parameters is highly dependent upon the value of the other parameters. For example, as the dielectric spacing increases, the capacitive loading on the feed trace is reduced, which diminishes the impact of changing the feed trace width.

One of the largest sources of variation in the PCB manufacturing process is the finished thickness of the PCB, with typical tolerances of 10 percent. For the HHA studied, this PCB thickness tolerance can cause the resonant frequency of the HHA to shift by as much as 39 megahertz. For the HHA, which has a narrow-band resonant impedance match, this design variation is unacceptable for optimum antenna performance. However, the PCB stack approach can mitigate this impact through the integration of an antenna resonant frequency tuning mechanism. The PCB stack can be made to rotate separately from the PCB on the bottom of the stack, allowing for an adjustment in the turns of the helix arms. As indicated by Table 4.11, variation of the helix turns by 14 percent can shift the resonant frequency by about 90 megahertz. With the addition of the appropriate alignment and keying features, this would be an effective method of tuning the resonant frequency of the HHA. In addition to resonant frequency tuning, this sensitivity analysis has also shown that the antenna's input impedance can be tuned through changes in the geometry of the feed

trace and through adjustments in the distance between the antenna stack and the ground plane, without significantly impacting the resonant frequency.

One primary limitation of the PCB stack approach for ESAs is the increase in antenna Q due to the dielectric material. Future work involves optimizations of the antenna structure to improve antenna Q and the integration of a broadband matching network to further improve the impedance bandwidth. Additionally, the application of this method outside the realm of ESAs and the characterization of fabricated prototypes is of interest.

CHAPTER 5

The Green's Function Method

The investigative work performed in the previous three sections leveraged commercial simulation software in order to evaluate the antenna designs. The software chosen uses the Finite-Difference Time Domain (FDTD) numerical method to solve the electromagnetic boundary value problem. The FDTD method involves the discretization of Maxwell's equations, in both time and space, so that they can be solved directly. In order to accomplish this, the temporal and spatial derivatives are approximated using the central difference. The electric and magnetic fields are then solved in an interleaved fashion by using the method developed by Yee [50]. Because Maxwell's equations are solved in the time domain, there exists requirements on the minimum temporal step needed to ensure numerical stability. The FDTD simulation time is therefore a function of many factors, including grid size and the source signal [51].

The FDTD is a very powerful method and is suited for solving electromagnetic boundary value problems in which the geometry is on the order of an electrical wavelength. However, as the problem space grows to a region that is electrically large compared to the wavelength of the frequencies being simulated, the size of the problem increases significantly, which can lead to high computational costs [52]. The other disadvantage is that, unlike analytic methods, when applicable, there is a lack of physical insight that is often gained when developing a mathematical model to describe an electromagnetic boundary value problem.

Inspired by a desire to gain deeper psychical insight of the mechanics behind electromagnetic boundary value problems, an analytic method approach has been sought for further study. One method that has garnished much attention over the years is the Green's function. The remainder of this thesis will explore the Green's function method through: 1) a brief summary of the history, 2) a description of methods used to develop the Green's function, 3) and one-dimensional Green's function examples with results comparison to the results from the FDTD method.

5.1 Background

Important coursework for students in electrical engineering is a class on signals and systems. One of the fundamental topics discussed is the transfer function for linear time invariant (LTI) systems. The transfer function describes the behavior of an LTI system to a given input and can be written as [53]:

$$h(t) = \frac{y(t)}{x(t)} \tag{5.1}$$

When the input of the system, $x(t)$, is the impulse function, the output, $y(t)$, will be the transfer function, $h(t)$, of the system. The system response can then be evaluated for any input through a convolution of the input signal with the transfer function. This fundamental concept is leveraged in a variety of engineering disciplines (e.g. signal processing and control systems) and is very useful in characterizing a system as a black box, which is only a function of time.

Since electromagnetic boundary value problems can be functions of both time and space, they require a more general concept of the transfer function, the Green's function, which can handle both temporal and spatial domains [54]. Electromagnetic boundary value problems, in a general form, can be written as a linear equation of the form [55]:

$$\mathcal{L}f = g \tag{5.2}$$

In this form, $\mathcal{L}$ is a linear operator that maps the domain of f into the range of $\mathcal{L}f$, which is equal to g [55]. In the context of electromagnetics, $\mathcal{L}$ is typically a differential operator, such as in the scalar and vector wave equations. f represents the unknown quantity that is to be solved for, typically the value of the electric or magnetic field. g is a forcing function and represents the source function, with an example being an electric current density. Boundary conditions for (5.2) can range from Dirichlet and Neummann conditions to

radiation conditions [56].

Since the typical goal in solving an electromagnetic boundary value problem is to determine the electric and magnetic fields, within a region, due to a source, the main challenge is to find the inverse of the linear operator $\mathcal{L}$ as in [55]:

$$f = \mathcal{L}^{-1}g \tag{5.3}$$

Often, it is desirable to obtain f for a variety of different source functions. For example, in antenna design it is desirable to evaluate antenna radiation characteristics for a range of frequencies, so as to determine the operational bandwidth. It is then desirable to have a formulation of (5.3) that is not dependent on the source, g. Similar to the transfer function concept of (5.1), this formulation of the inverse linear operator can be obtained by determining f when g is the Dirac delta function. The inverse linear operator, when the source function is the Dirac delta function, is referred to the Green's function for the electromagnetic boundary value problem. Using the scalar Green's function, (5.3) can then be written as [55]:

$$f(\mathbf{r}) = \mathcal{L}^{-1}g(\mathbf{r}) = \int_V G(\mathbf{r}|\mathbf{r}')g(\mathbf{r}')dV' \tag{5.4}$$

Where $\mathbf{r}$ is a solution or field point defined by the spatial components $\mathbf{x}, \mathbf{y}, \mathbf{z}$ and $\mathbf{r}'$ is the position of the source. The similarity to (5.1) is illustrated in Fig. 5.1.

As explained by Tazzioli in [57], the Green's function was developed in 1828 by George Green, a mathematical physicist [57]. The initial development was published in an essay entitled, "An Essay on the Application of Mathematical Analysis to the Theories of Electricity and Magnetism." The initial derivation was developed and applied to potential theory. The work performed by George Green was as a influential resource for many nineteenth century mathematicians, such as Hermann von Helmholtz and Bernhard Riemann. A Green's function for a given boundary value problem doesn't always exist, which means a developed Green's function needs to be proven.
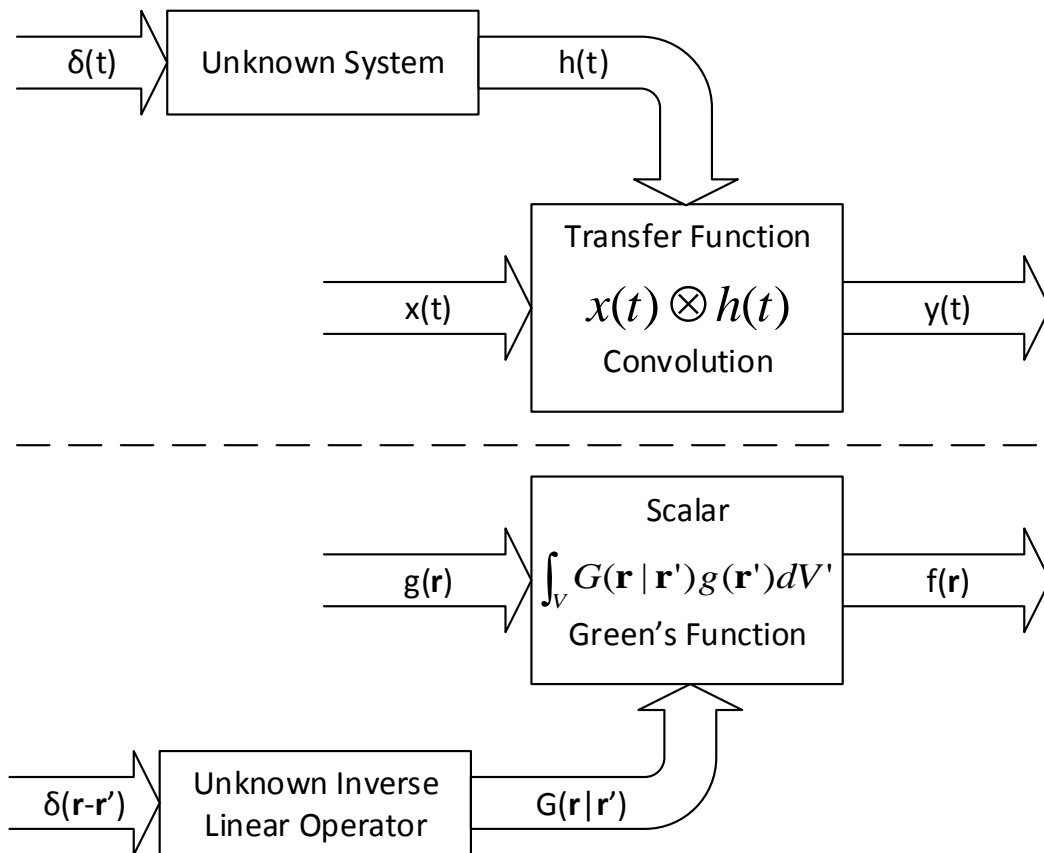
Figure 5.1: Similarity of the transfer function in LTI systems to the Green's function method.

As an example application of (5.4), would be for use in the scalar Helmholtz wave equation, which can be written as [58]:

$$\nabla^2 G(\mathbf{r}, \mathbf{r}') + \beta^2 G(\mathbf{r}, \mathbf{r}') = \delta(\mathbf{r}, \mathbf{r}') \tag{5.5}$$

Where $G(\boldsymbol{r}, \boldsymbol{r}')$ is the Green's function and β is the phase constant of the wave. Once the Green's function for the system is known, the system can be evaluated for any input by an integration of the input signal (source function) and the Green's function. This allows a given system to be evaluated for a number of different forcing functions without having to recompute the entire problem space, unlike computational methods such as the FDTD method [59]. This advantage is beneficial in antenna design as part of the design process typically involves the characterization of a device over a variety of frequency ranges and, in the case of phased antenna arrays, the phasing of the antenna current.

One limitation of (5.4) is that it is not directly applicable to vector problems. Since most general electromagnetic boundary value problems involve vectors, a more general form of the Green's function is the dyadic Green's function [60].

The dyadic Green's function form is able to satisfy the general vector form of a differential vector equation, such as the vector Helmholtz wave equation. The dyadic form is needed because, in the scalar formulation (5.5), the technique of separation of variables is used in order to determine the solution [24]. For the vector Helmholtz wave equation, a different approach is needed as the relations developed apply only to scalar field quantities. The reason can be seen through inspection of the vector potential A and the inhomogeneous Helmholtz wave equation, for time-harmonic and lossless fields, subject to an impressed current source, given as [58]:

$$\nabla^2 \mathbf{A}(x, y, z) + \beta^2 \mathbf{A}(x, y, z) = -j\omega\mu \mathbf{J}_i(x, y, z) \tag{5.6}$$

Application of (5.4) would result in:

$$\mathbf{A}(x, y, z) \neq -j\omega\mu \int_V G(\mathbf{r}|\mathbf{r}')\mathbf{J}_i(\mathbf{r}')dV' \tag{5.7}$$

Which implies that a component of $\mathbf{J}_i$ produces a component in $\mathbf{A}$, which is parallel to the component of the former, which in general is not correct [58].

The dyadic Green's function can be developed for the general vector form of a differential, written as [58]:

$$\mathcal{L}\mathbf{f} = \mathbf{g} \tag{5.8}$$

Where the the Sturm-Louville operator L is no longer used, but rather $\mathcal{L}$ a general differential operator. The solution to (5.8) can be written as [58]:

$$\mathbf{h}(\mathbf{r}) = \int \int \int_V \mathbf{f}(\mathbf{r}) \cdot \bar{\mathbf{G}}(\mathbf{r}, \mathbf{r}')dv' \tag{5.9}$$

Where $\bar{\mathbf{G}}(\mathbf{r}, \mathbf{r}')$ is the dyadic Green's function and is given by [58]:

$$\bar{\mathbf{G}}(\mathbf{r}, \mathbf{r}') = \hat{\mathbf{a}}_x \mathbf{G}_x(\mathbf{r}, \mathbf{r}') + \hat{\mathbf{a}}_y \mathbf{G}_y(\mathbf{r}, \mathbf{r}') + \hat{\mathbf{a}}_z \mathbf{G}_z(\mathbf{r}, \mathbf{r}') \tag{5.10}$$

The dyadic Green's function given in (5.10) can be written in matrix form as:

$$\begin{bmatrix} G_{xx} & G_{xy} & G_{xz} \\ G_{yx} & G_{yy} & G_{yz} \\ G_{zx} & G_{zy} & G_{zz} \end{bmatrix} \tag{5.11}$$

To develop the Green's function for a given problem, a number of methods exist whose selection and application are dependent upon the problem to be solved, with the representation of the source being one such consideration [58].

5.2   Dimensional Analysis

To gain further insight into properties of the Green's function, we first perform a dimensional analysis on the general Green's function form and then apply the general case to a couple of specific examples. In order to perform this analysis, we take note of the dimensions for the Dirac delta function, which can be derived by the property given by [61]:

$$\int_{-\infty}^{+\infty} \delta(x)dx = 1 \tag{5.12}$$

In order for (5.12) to be dimensionless, the following dimensional analysis must be true, assuming a x is a single spatial variable with units of meters:

$$\int_{-\infty}^{+\infty} \delta(x)dx = \left[\frac{1}{m}\right] \cdot \left[\frac{m}{1}\right] = 1 \tag{5.13}$$

The Dirac delta function then takes on units that are the inverse of its spatial dimension. In order to determine the dimensions for a general scalar Green's function, (5.2) is first rewritten in terms of the Green's function [55]:

$$\mathcal{L}G(\mathbf{r}|\mathbf{r}') = \delta(\mathbf{r} - \mathbf{r}') \tag{5.14}$$

$$G(\mathbf{r}|\mathbf{r}') = \mathcal{L}^{-1}\delta(\mathbf{r} - \mathbf{r}') \tag{5.15}$$

The dimensions for the scalar Green's function can then be derived as:

$$G(\mathbf{r}|\mathbf{r}') = \left[\frac{1}{dim(\mathcal{L})}\right] \cdot \left[\frac{dim(\mathbf{r})}{1}\right] \tag{5.16}$$

Where the notation $dim()$ refers to the dimensions of the physical quantities associated with the argument. From inspection of (5.16), it can be seen that the units of the Green's function depend both on the spatial dimensions of the problem and the dimension of the

operator.

This property can be confirmed through a dimensional analysis of the Green's function for Poisson's equation given by [62]:

$$\nabla^2 V = -\frac{q_v}{\varepsilon} \tag{5.17}$$

Where V is the voltage and q_v is the charge density. The dimensional analysis of (5.17) results in:

$$\left[\frac{1}{m^2}\right] \cdot \left[\frac{V}{1}\right] = \left[\frac{C}{m^3}\right] \cdot \left[\frac{m}{F}\right] \tag{5.18}$$

$$\left[\frac{1}{m^2}\right] \cdot \left[\frac{V}{1}\right] = \left[\frac{C}{\cancel{m^3}m^2}\right] \cdot \left[\frac{\cancel{m}}{F}\right] \tag{5.19}$$

$$\left[\frac{1}{m^2}\right] \cdot \left[\frac{V}{1}\right] = \left[\frac{\cancel{C}}{m^2}\right] \cdot \left[\frac{V}{\cancel{C}}\right] \tag{5.20}$$

$$\left[\frac{V}{m^2}\right] = \left[\frac{V}{m^2}\right] \tag{5.21}$$

The integration of the Green's function and the right hand side of (5.17) will yield the voltage, as described by [58]:

$$V(x, y, z) = -\frac{1}{\varepsilon} \int \int \int q(x', y', z') G(x, y, z; x', y', z') dx' dy' dz' \tag{5.22}$$

The dimensional analysis for (5.17) is repeated for the Green's function, with the source set to the Dirac delta function:

$$\nabla^2 G(x, y, z; x', y', z') = \delta(x - x')\delta(y - y')\delta(z - z') \tag{5.23}$$

The scalar Laplacian is a second-order differential operator and since the differentiation

is with respect to the spatial components, the units will be meters^{-2}. Using the units for the Dirac delta function determined in (5.13) The dimensions can then be written as:

$$\left[\frac{1}{m^2}\right] G = \left[\frac{1}{m^3}\right] \tag{5.24}$$

$$G = \left[\frac{1}{\cancel{m^3} m}\right] \cdot \left[\frac{\cancel{m^2}}{1}\right] = \left[\frac{1}{m}\right] \tag{5.25}$$

Thus for the three-dimensional Poisson's equation, the Green's function has units that are the inverse of the spatial units, meters^{-1}. This result can be confirmed through an evaluation of the dimensions for (5.22), using the results of (5.25):

$$\left[\frac{V}{1}\right] = \left[\frac{m}{F}\right] \cdot \left[\frac{C}{m^3}\right] \cdot \left[\frac{1}{m}\right] \cdot \left[\frac{m^3}{1}\right] \tag{5.26}$$

$$\left[\frac{V}{1}\right] = \left[\frac{\cancel{m} V}{\cancel{C}}\right] \cdot \left[\frac{\cancel{C}}{\cancel{m^3}}\right] \cdot \left[\frac{1}{\cancel{m}}\right] \cdot \left[\frac{\cancel{m^3}}{1}\right] \tag{5.27}$$

$$\left[\frac{V}{1}\right] = \left[\frac{V}{1}\right] \tag{5.28}$$

5.3 Examples in One-Dimension

In order to provide an illustration of the Green's function, two one-dimensional examples of the closed form Green's function are investigated in this section. Both examples consist of plane waves propagating in free space due to a time harmonic source, whose position is denoted by z'. The plane waves are incident upon a dielectric medium, with relative permittivity and permeability denoted by ε_1 and μ_1. The Green's function results are then correlated against results obtained from a FDTD simulation of the same problem.
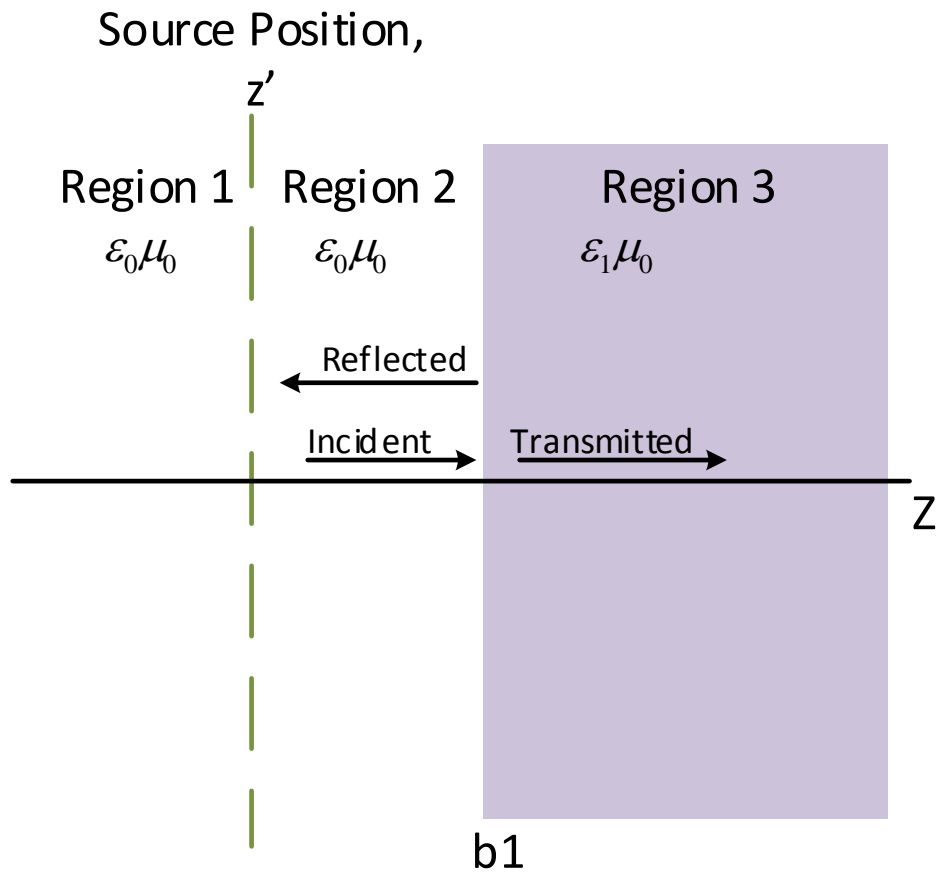
Figure 5.2: First example Green's function problem consisting of a single dielectric interface.

The first example problem is depicted in Fig. 5.2. The x component of the electric field is sought for a time harmonic plane wave as a function of position. The governing differential equation for this problem can be written as:

$$\nabla^2 E_x(z; z') + k^2 E_x(z; z') = j\omega\mu J_x(z; z') \tag{5.29}$$

Where E_x is the x component of the electric field and J_x is the impressed current density [63]. The problem consists of a single material interface boundary, which has a permittivity of $\varepsilon_1 = \varepsilon_r\varepsilon_0$ and permeability of $\mu_1 = \mu_0$. This problem can be viewed as solving (5.29) for an inhomogeneous, layered medium, which will result in an incident, reflected, and transmitted wave at each material boundary [64]. An approach to solving this problem is to leverage the Green's function property of superposition [65] in order to develop a Green's function for each region. Because the tangential components of the electric field must be continuous across the material boundary [66], the associated boundary conditions can be written as:

$$E_x{}^{R2}(z = b_1) = E_x{}^{R3}(z = b_1) \tag{5.30}$$

$$\frac{d}{dz}E_x{}^{R2}(z = b_1) = \frac{d}{dz}E_x{}^{R3}(z = b_1) \tag{5.31}$$

The Green's function for (5.29) can then be written as:

$$\nabla^2 G_x(z; z') + k^2 G_x(z; z') = \delta(z - z') \tag{5.32}$$

The boundary conditions for (5.32) at the dielectric interface then become:

$$G_x{}^{R2}(z = b_1) = G_x{}^{R3}(z = b_1) \tag{5.33}$$

$$\frac{d}{dz}G_x{}^{R2}(z = b_1) = \frac{d}{dz}G_x{}^{R3}(z = b_1) \tag{5.34}$$

The Green's function requires continuity of G_x at the source location which results in:

$$G_x{}^{R2}(z = z') = G_x{}^{R3}(z = b_1) \tag{5.35}$$

The derivative G_x, $\frac{d}{dz}G_x$, will be discontinuous at the source location [67]. The value of the discontinuity is dependent upon the Sturm-Liouville form of (5.32) and this problem can be written as:

$$\frac{d}{dz}G_x{}^{R2}(z = z') - \frac{d}{dz}G_x{}^{R1}(z = z') = 1 \tag{5.36}$$

Using (5.4), the electric field for this problem can be written as:

$$E_x(z; z') = j\omega\mu \int J_x(z; z')G_x(z; z')dz' \tag{5.37}$$

Leveraging the property of superposition, the Green's function for the problem can be written as a superposition of Green's functions describing each region:

$$E_x(z; z') = j\omega\mu \left[\int_z^{z+z'-zmin} J_x(z; z')G_x(z; z')dz' \right.$$
$$\left. + \int_{z+z'-b1}^z J_x(z; z')G_x(z; z')dz' + \int_{z+z'-zmax}^{z+z'-b_1} J_x(z; z')G_x(z; z')dz' \right] \tag{5.38}$$

Then, the homogeneous solution of the Green's function, for each region, needs to be determined. The homogeneous form of (5.32) can be written as:

$$\nabla^2 G_x(z; z') + k^2 G_x(z; z') = 0 \tag{5.39}$$

Since G_x describes time harmonic waves that are propagating along the z direction, the

solution form of (5.39) that represents traveling waves is chosen [24]. The solution represents two sets of traveling waves, one in the positive z direction and one in the negative z direction. For the first region, there will only be waves propagating away from the source in the minus z direction, which can be written as:

$$y_1 = A_1 e^{-jk_0 z} + B_1 e^{+jk_0 z} \qquad for \quad z < z' \tag{5.40}$$

Region two will consist of waves traveling in both directions, due to the reflected wave at the material boundary denotes by b_1. This reflected wave will produce standing wave whose magnitude is dependent on the permittivity of the medium in region three. The solution for (5.39) within region 2 can be written as:

$$y_2 = A_2 e^{-jk_0 z} + B_2 e^{+jk_0 z} \qquad for \quad z' < z < b_1 \tag{5.41}$$

Since region three is assumed to extend to infinity in the positive z direction, there will only be a wave traveling in the positive z direction, which can be written as:

$$y_3 = A_3 e^{-jk_1 z} + B_3 e^{\pm jk_1 z} \qquad for \quad z > b_1 \tag{5.42}$$

The remaining step in finding the Green's function for the problem is the determination of the amplitude coefficients in (5.40), (5.41), and (5.42). The amplitude coefficients can be determined by writing the Green's functions, representing each region, as a system of equations in matrix form as:

$$
\begin{bmatrix}
e^{+jk_0 z'} & -e^{-jk_0 z'} & -e^{+jk_0 z'} & 0 \\
-jk_0 e^{+jk_0 z'} & -jk_0 e^{-jk_0 z'} & jk_0 e^{+jk_0 z'} & 0 \\
0 & e^{-jk_0 b_1} & e^{+jk_0 b_1} & -e^{-jk_1 b_1} \\
0 & -jk_0 e^{-jk_0 b_1} & jk_0 e^{+jk_0 b_1} & jk_1 e^{-jk_1 b_1}
\end{bmatrix}
\begin{bmatrix}
B_1 \\ A_2 \\ B_2 \\ A_3
\end{bmatrix}
=
\begin{bmatrix}
0 \\ 1 \\ 0 \\ 0
\end{bmatrix}
\tag{5.43}
$$

The solution for (5.43) can be determined by multiplying each side by inverse of the first matrix. This results in the following Green's functions for each region:

$$G_x(z; z') = j\frac{1}{2k_0}\left[\left(\frac{k_0 - k_1}{k_0 + k_1}\right)e^{-jk_0(2b_1 - z')} + e^{-jk_0 z'}\right]e^{+jk_0 z} \qquad for \quad z < z' \qquad (5.44)$$

$$G_x(z; z') = j\frac{1}{2k_0}\left[e^{jk_0 z'}e^{-jk_0 z} + \left(\frac{k_0 - k_1}{k_0 + k_1}\right)e^{-jk_0(2b_1 - z')}e^{jk_0 z}\right] \qquad for \quad z' < z < b_1 \quad (5.45)$$

$$G_x(z; z') = j\frac{1}{k_1 + k_0}e^{-jk_1 b_1}e^{-jk_1(b_1 - z')}e^{-jk_1 z} \qquad for \quad z > b_1 \qquad (5.46)$$

The Green's function for each region are illustrated in Fig. 5.3. The source is set to a frequency of 150 megahertz, which is used to determine the wavenumber for reach region. The Green's function is plotted in the time harmonic phasor form, with both real and imaginary components. It can be seen that there exists standing waves in region two as a result of the combination of the incident and reflected wave at the dielectric boundary, b_1. The Green's function is continuous across the interface at b_1 and at the source location z'. Units for the Green's function in this example are per meter.

By substituting (5.44), (5.45), and (5.46) into (5.38), the electric field intensity can be solved. The results of (5.38) are plotted in Figs. 5.4 and 5.5 for the real and imaginary components of the phasor form of the electric field. These values can be converted to their time domain equivalents by multiplying the phasor form by e^{jwt}, taking the real part, and multiplying by $\sqrt{2}$ to get the time domain solution [24]. The time domain solution is plotted in Fig. 5.6.
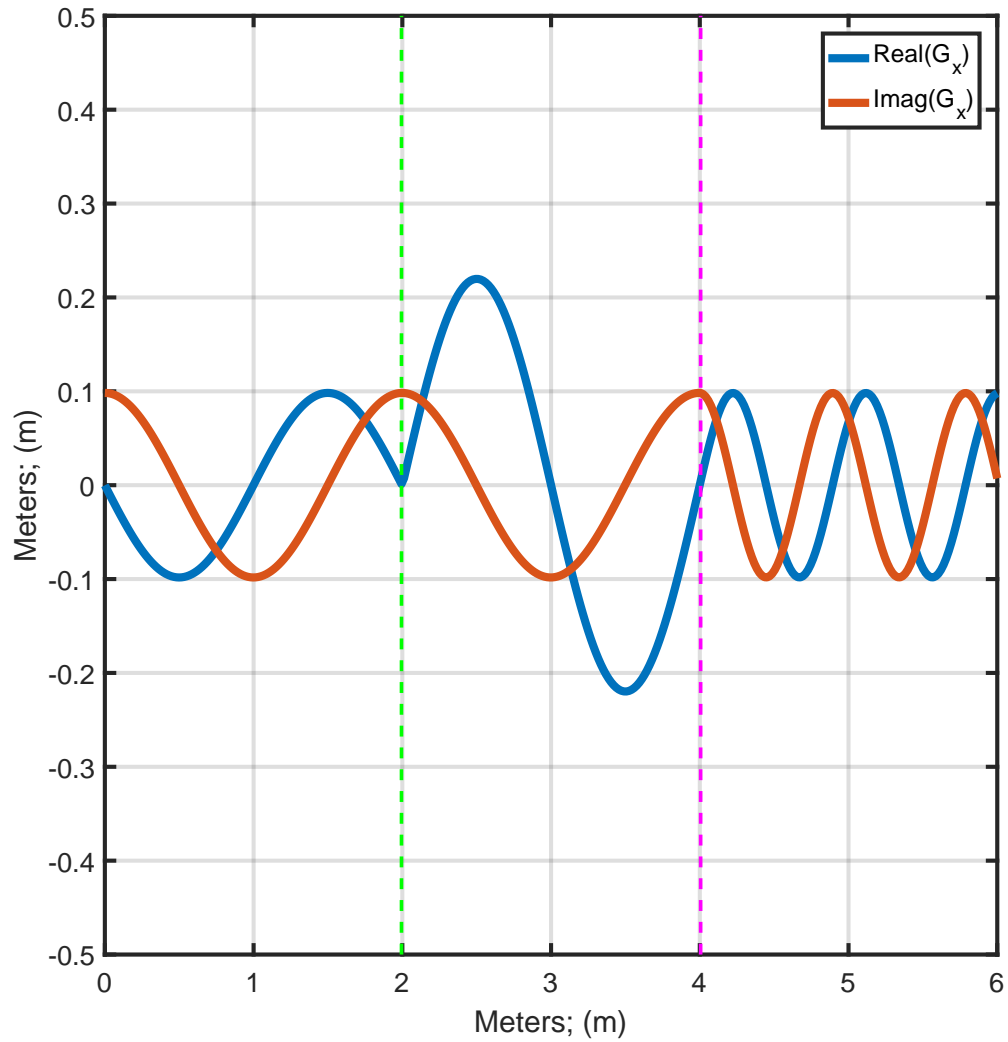
Figure 5.3: Plot of the Green's function real and imaginary components of the first example problem in the phasor domain.
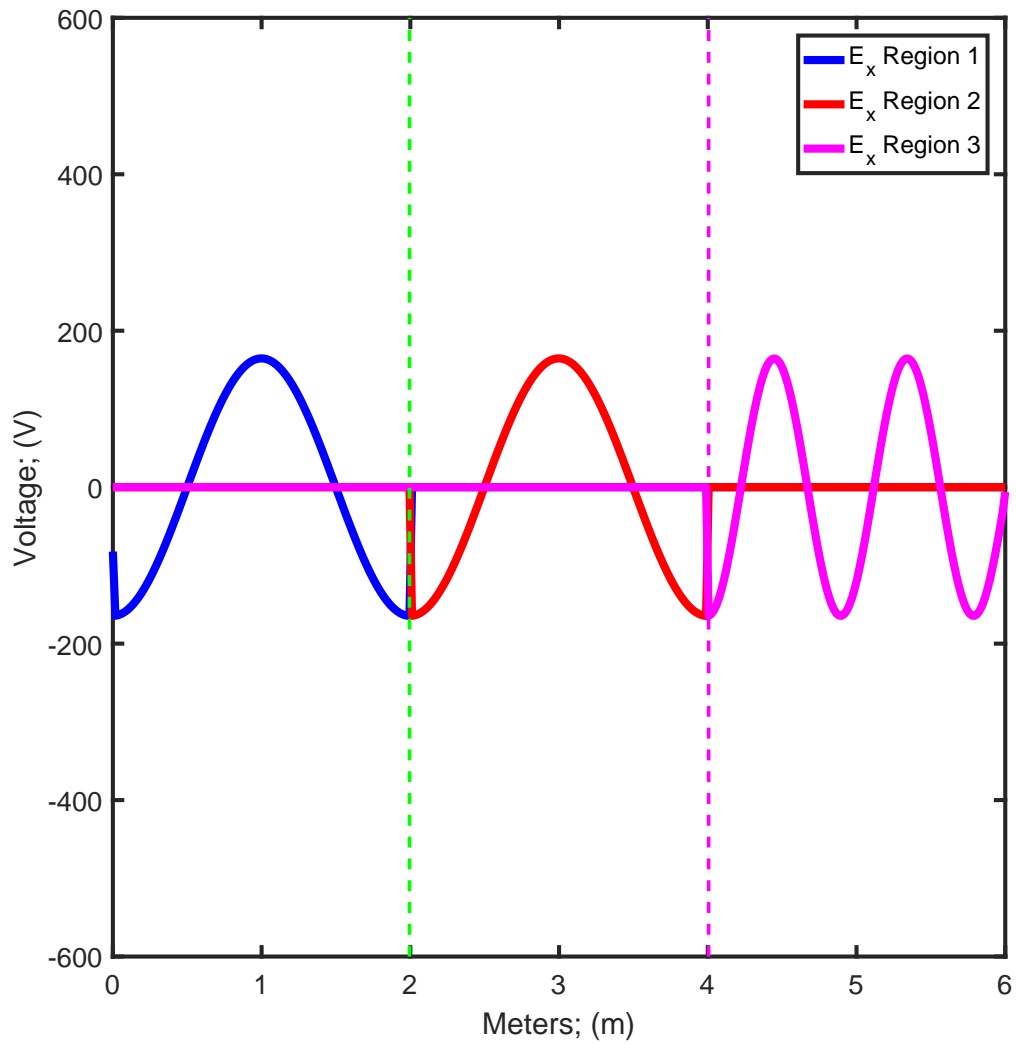
Figure 5.4: Plot of the phasor domain real component of the electric field intensity for the first example problem.
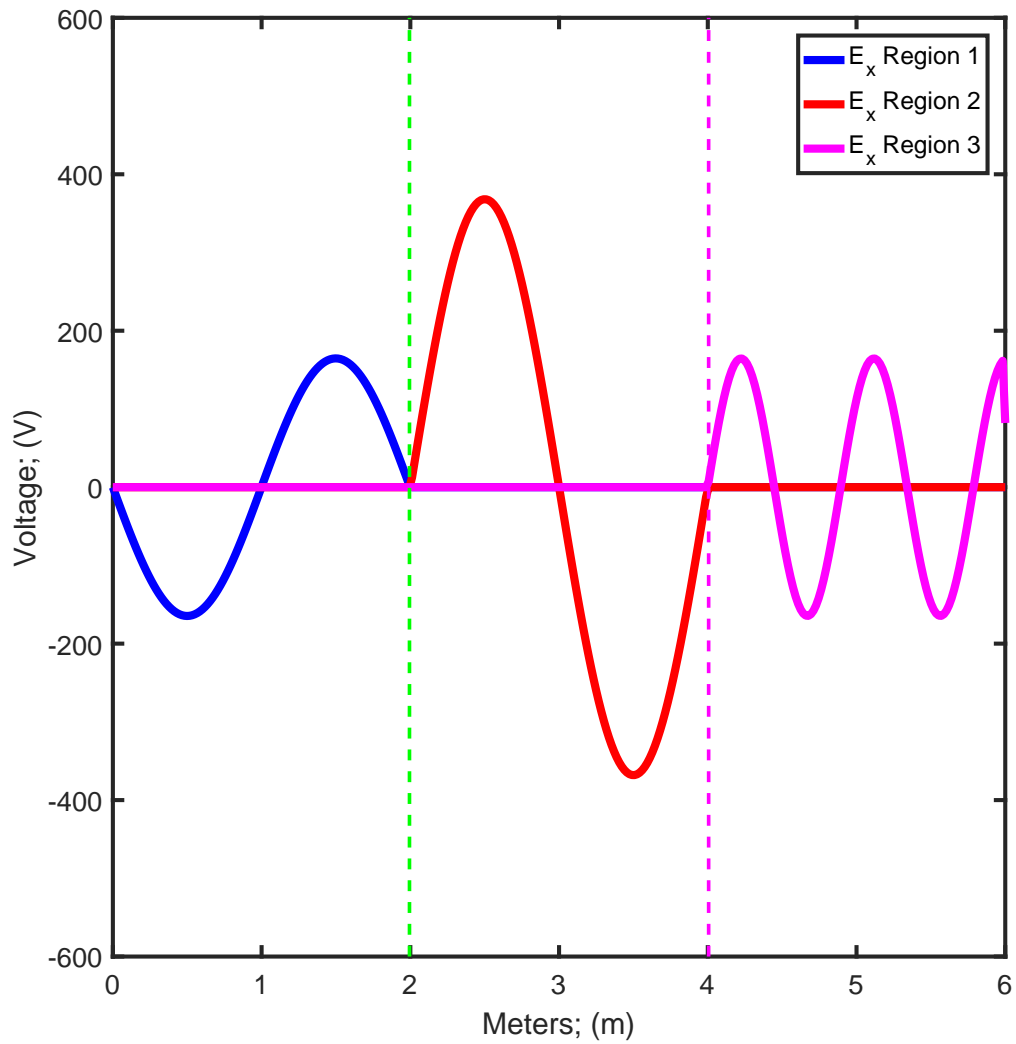
Figure 5.5: Plot of the phasor domain imaginary component of the electric field intensity for the first example problem.

Figure 5.6: Plot of the time domain electric field intensity for the first example problem.

Figure 5.7: FDTD solution of the time domain electric field intensity for the first example problem.

Figure 5.8: Correlation of the electric field intensity results for the FDTD and Green's function methods for the first example problem.

The same problem was also solved using the FDTD method with the simulation results plotted in Fig. 5.7. The Green's function and FDTD results are then correlated in Fig. 5.8 with good agreement. One advantage of the G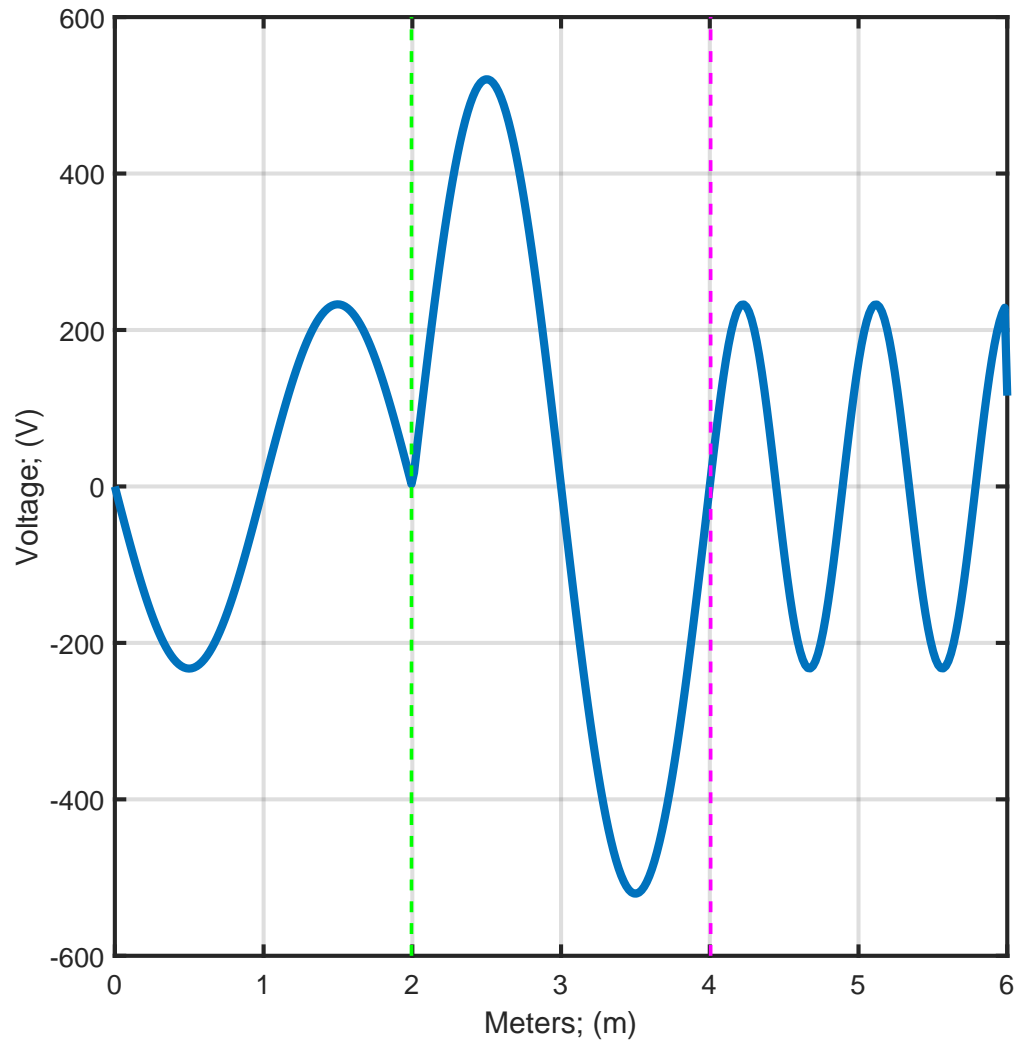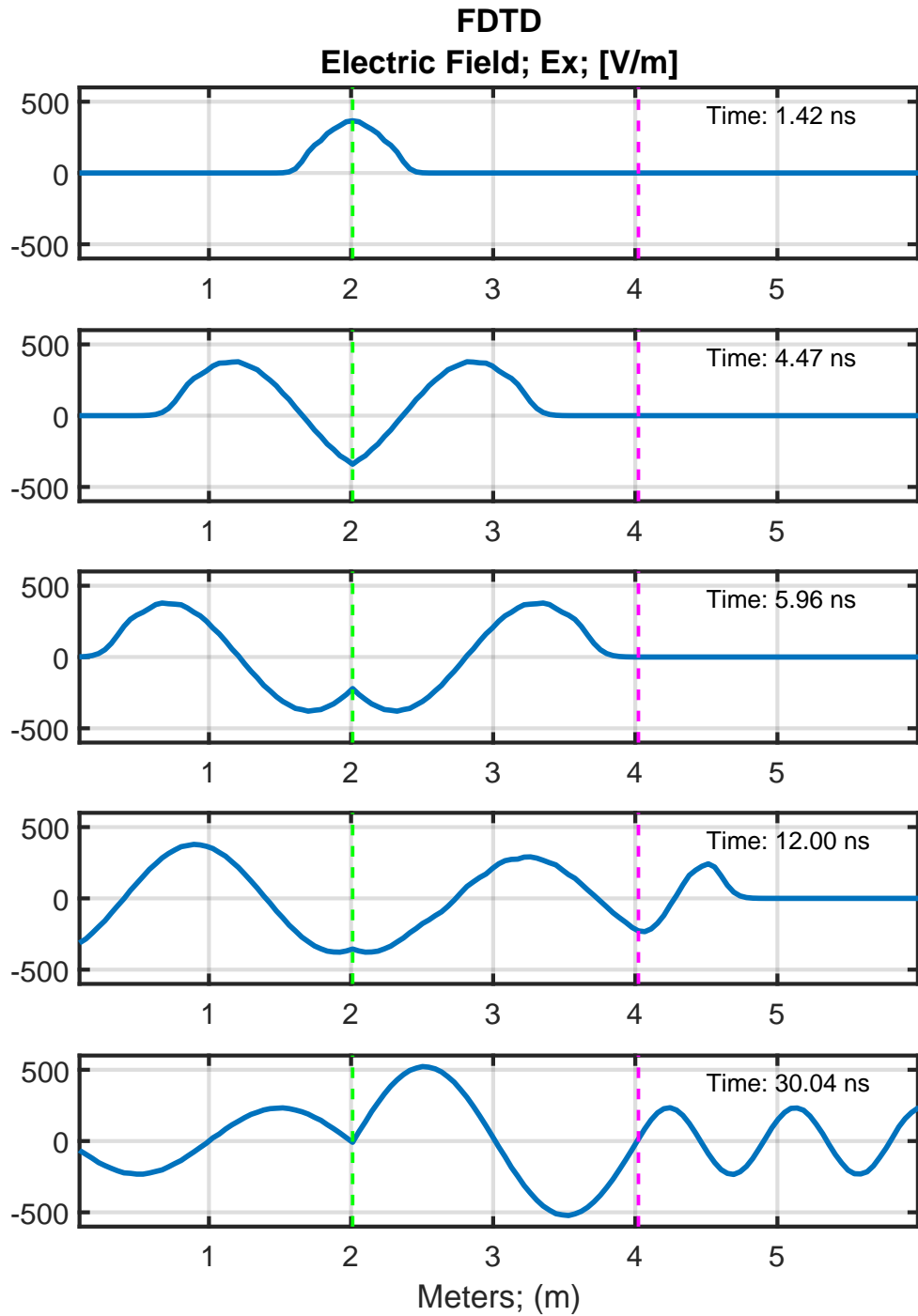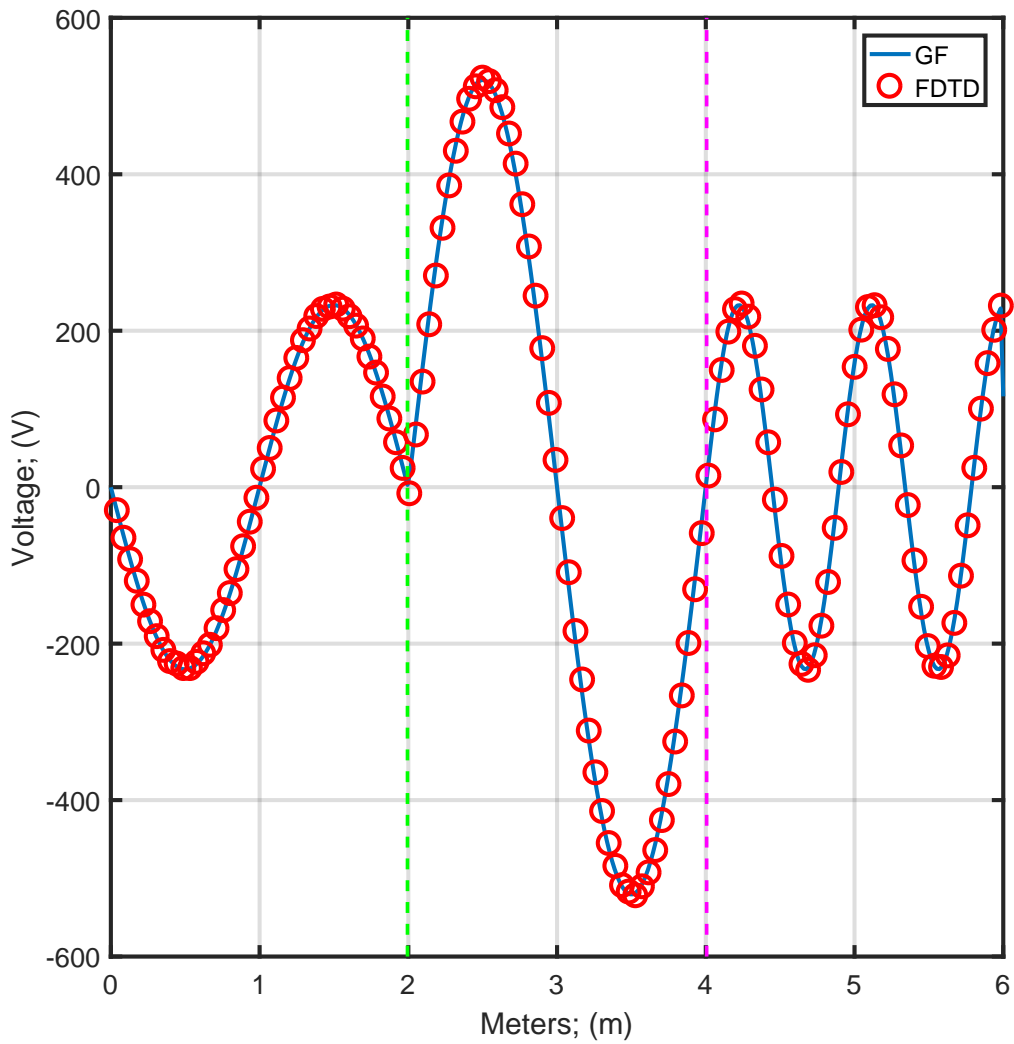reen's function method over the FDTD method is that the FDTD simulation would need to be repeated for a new source signal, which is in contrast to the Green's function method. Once the Green's function for a problem is found, it can be used to solve a boundary value problem for any input. However, there is no guarantee that a Green's exists for the problem [67].

The second example is similar to the first but includes additional regions, as shown in Fig. 5.9. The process for solving the second problem is the same and simply needs to include the Green's functions for the additional regions. Modification of (5.38) to include the additional regions results in:

$$
\begin{aligned}
E_x(z; z') = j\omega\mu \Bigg[&\int_z^{z+z'-zmin} J_x(z; z')G_x(z; z')dz' \\
&+ \int_{z+z'-b1}^z J_x(z; z')G_x(z; z')dz' + \int_{z+z'-b2}^{z+z'-b_1} J_x(z; z')G_x(z; z')dz' \\
&+ \int_{z+z'-b3}^{z+z'-b_2} J_x(z; z')G_x(z; z')dz' + \int_{z+z'-b4}^{z+z'-b_3} J_x(z; z')G_x(z; z')dz' \\
&+ \int_{z+z'-zmax}^{z+z'-b_4} J_x(z; z')G_x(z; z')dz' \Bigg]
\end{aligned}
$$

(5.47)

With the additional regions added to the problem, the system of equations in (5.43) needs to be modified in order to incorporate the boundary conditions of the additional regions. The new form can be written as:

$$
\begin{bmatrix}
e^{+jk_0z'} & -e^{-jk_0z'} & -e^{+jk_0z'} & 0 & 0 & 0 & 0 & 0 & 0 & 0 \\
-jk_0e^{+jk_0z'} & -jk_0e^{-jk_0z'} & jk_0e^{+jk_0z'} & 0 & 0 & 0 & 0 & 0 & 0 & 0 \\
0 & e^{-jk_0b_1} & e^{+jk_0b_1} & -e^{-jk_1b_1} & -e^{+jk_1b_1} & 0 & 0 & 0 & 0 & 0 \\
0 & -jk_0e^{-jk_0b_1} & jk_0e^{+jk_0b_1} & jk_1e^{-jk_1b_1} & -jk_1e^{+jk_1b_1} & 0 & 0 & 0 & 0 & 0 \\
0 & 0 & 0 & e^{-jk_1b_2} & e^{+jk_1b_2} & -e^{-jk_0b_2} & -e^{+jk_0b_2} & 0 & 0 & 0 \\
0 & 0 & 0 & -jk_1e^{-jk_1b_2} & jk_1e^{+jk_1b_2} & jk_0e^{-jk_0b_2} & -jk_0e^{+jk_0b_2} & 0 & 0 & 0 \\
0 & 0 & 0 & 0 & 0 & e^{-jk_0b_3} & e^{+jk_0b_3} & -e^{-jk_2b_3} & -e^{+jk_2b_3} & 0 \\
0 & 0 & 0 & 0 & 0 & -jk_0e^{-jk_0b_2} & jk_0e^{+jk_0b_3} & jk_2e^{-jk_2b_3} & -jk_2e^{+jk_2b_3} & 0 \\
0 & 0 & 0 & 0 & 0 & 0 & 0 & e^{-jk_0b_3} & e^{+jk_0b_3} & -e^{-jk_2b_3} \\
0 & 0 & 0 & 0 & 0 & 0 & 0 & -jk_0e^{-jk_0b_2} & jk_0e^{+jk_0b_3} & jk_2e^{-jk_2b_3}
\end{bmatrix}
\begin{bmatrix}
B_1 \\ A_2 \\ B_2 \\ A_3 \\ B_3 \\ A_4 \\ B_4 \\ A_5 \\ B_5 \\ A_6
\end{bmatrix}
=
\begin{bmatrix}
0 \\ 1 \\ 0 \\ 0 \\ 0 \\ 0 \\ 0 \\ 0 \\ 0 \\ 0
\end{bmatrix}
\tag{5.48}
$$

Using the same procedure as before of multiplying both sides of (5.48) by the inverse of the first matrix results in the solution of the amplitude coefficients for the Green's functions.

The composite Green's function for the second example is illustrated in Fig. 5.10. Both the real and imaginary parts of the phasor form are plotted. It is evident that standing waves exist within each region, except regions 1 and 6 due to their extension to infinity. Next, the amplitude coefficients from (5.48) are substituted into (5.47) and integrated to yield the electric field. The real component of the electric field is illustrated in Fig. 5.11 and the imaginary component in Fig. 5.12. The phasor form is then converted to the time domain and plotted in Fig. 5.13.

As done in the previous example, the same problem is solved using the FDTD method, with result plotted in Fig. 5.14. Finally the Green's function solution is correlated to the FDTD solution in Fig. 5.15. The results correlate well, but there is more error than that observed in the first problem. Some of this error is believed to be tied to the time step resolution chosen for the FDTD problem. The other suspicion is that it is due to the two solutions not being in phase with each other. The Green's function, in these examples, represents the more accurate solution.
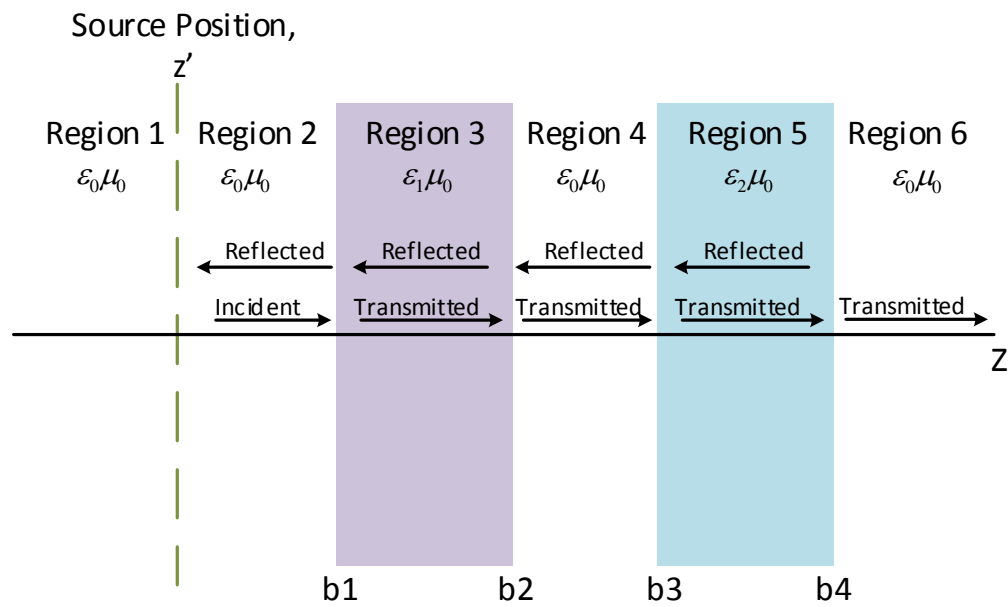
Figure 5.9: Second example Green's function problem consisting of a multiple dielectric interfaces.
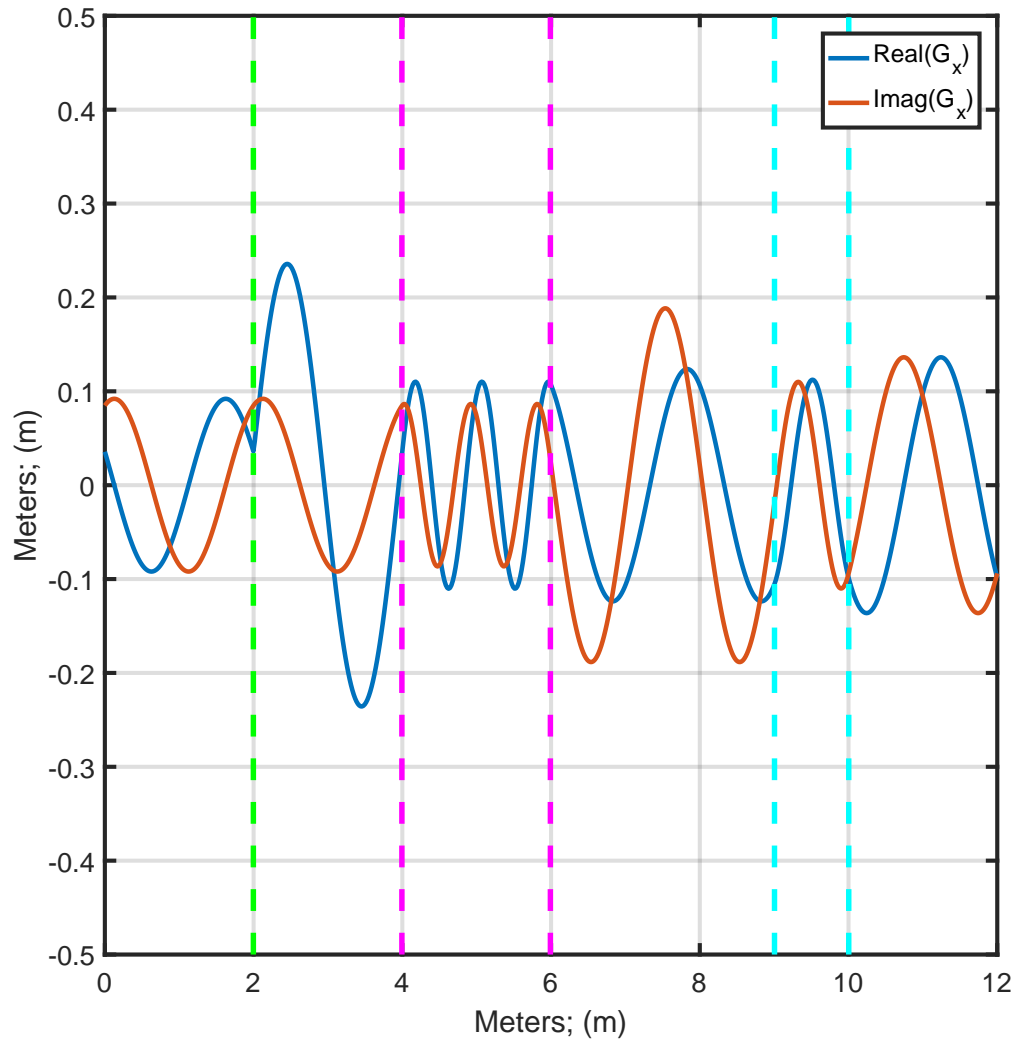
Figure 5.10: Plot of the phasor domain real component of the electric field intensity for the second example problem.
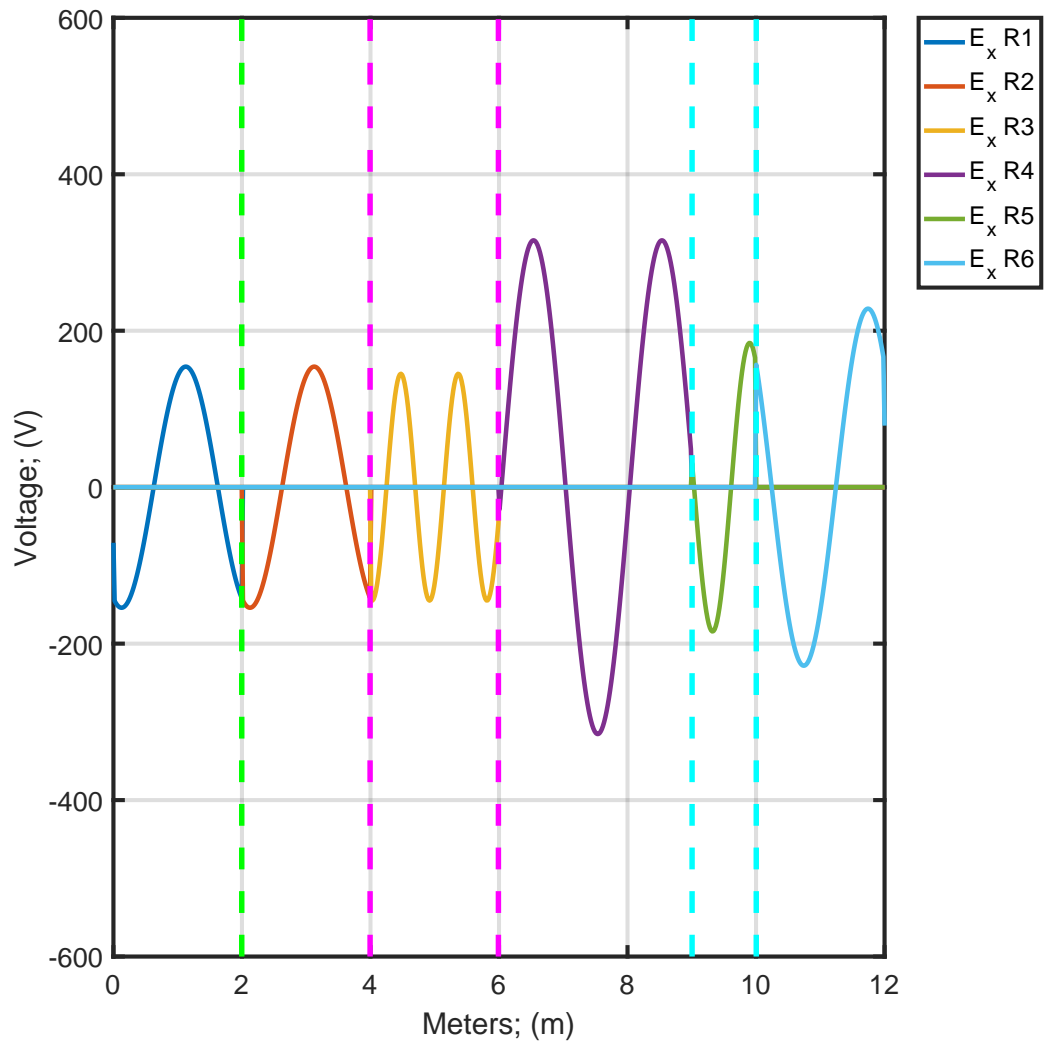
Figure 5.11: Plot of the phasor domain real component of the electric field intensity for the second example problem.
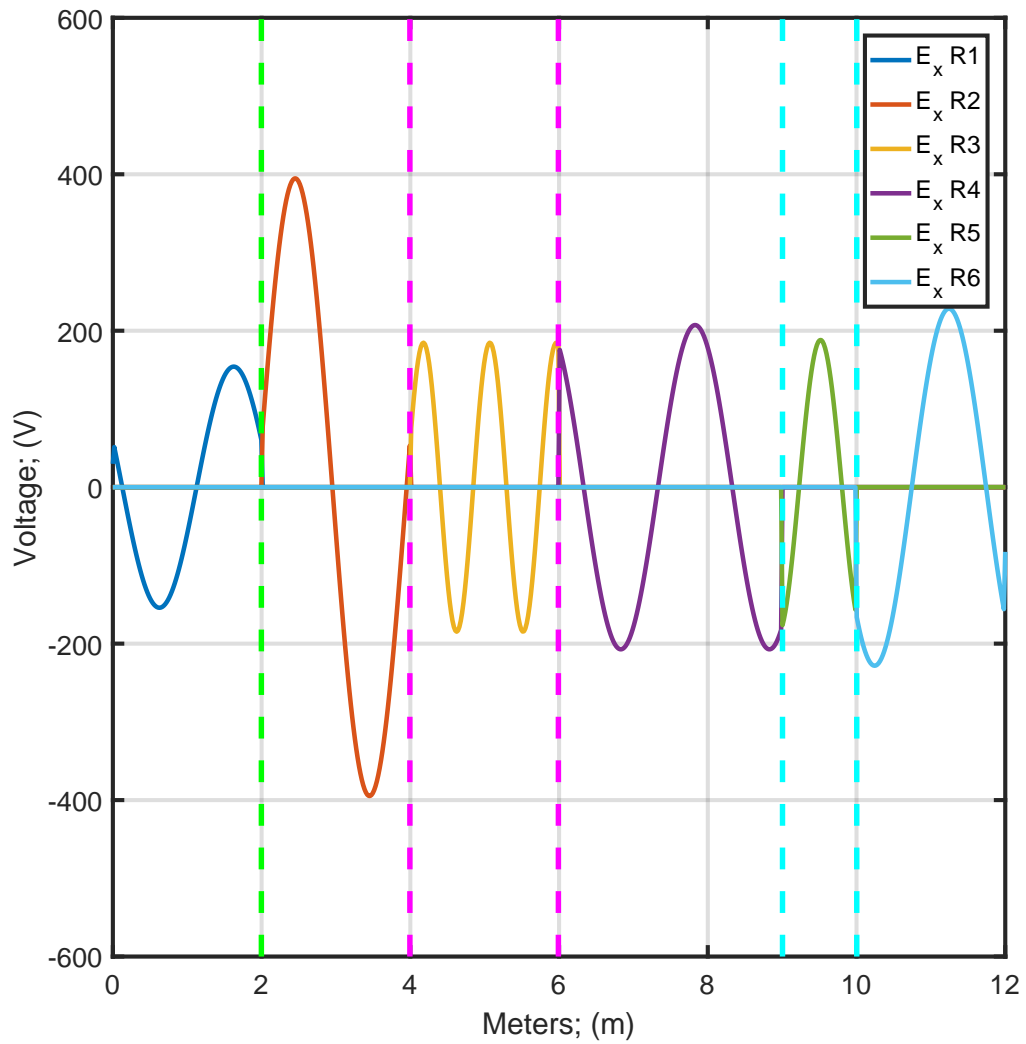
Figure 5.12: Plot of the phasor domain imaginary component of the electric field intensity for the second example problem.
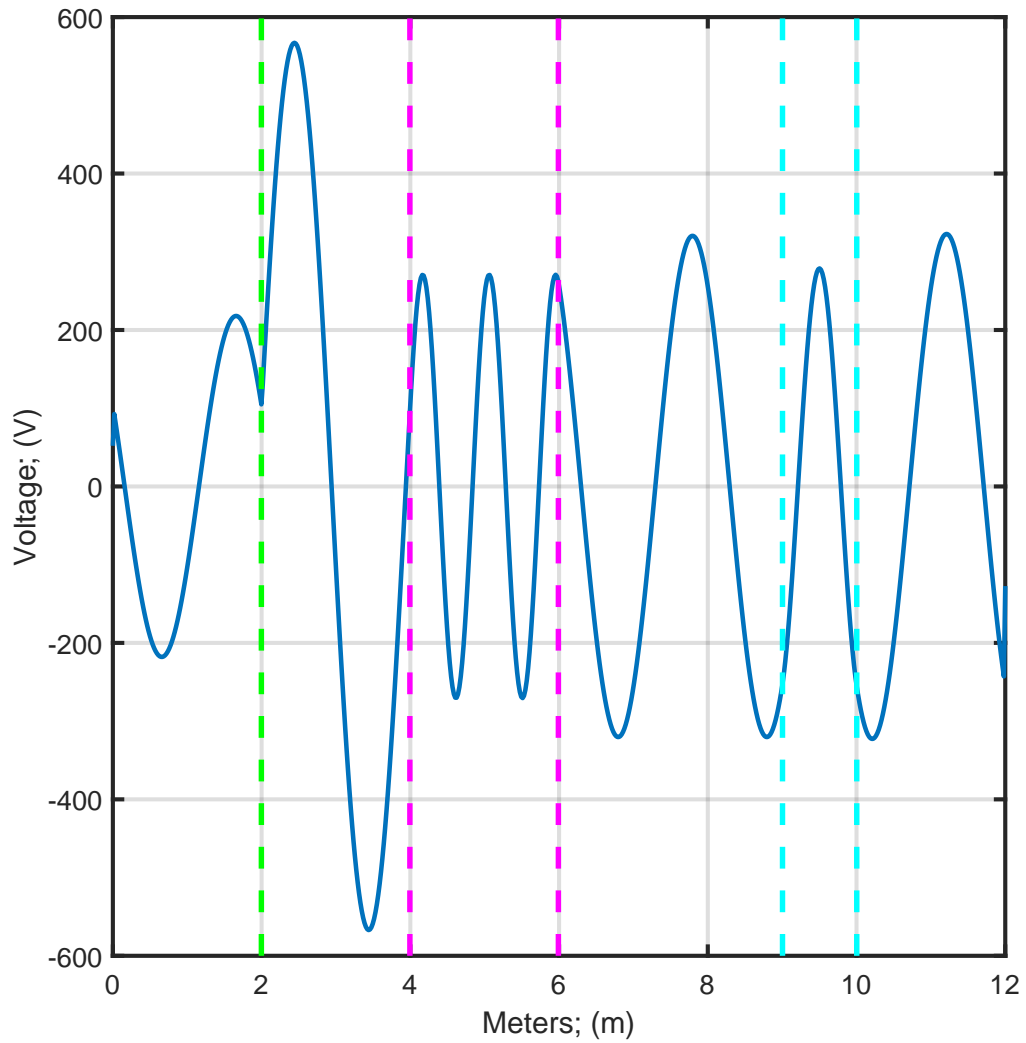
Figure 5.13: Plot of the time domain electric field intensity for the second example problem.

Time: 69.62 ns
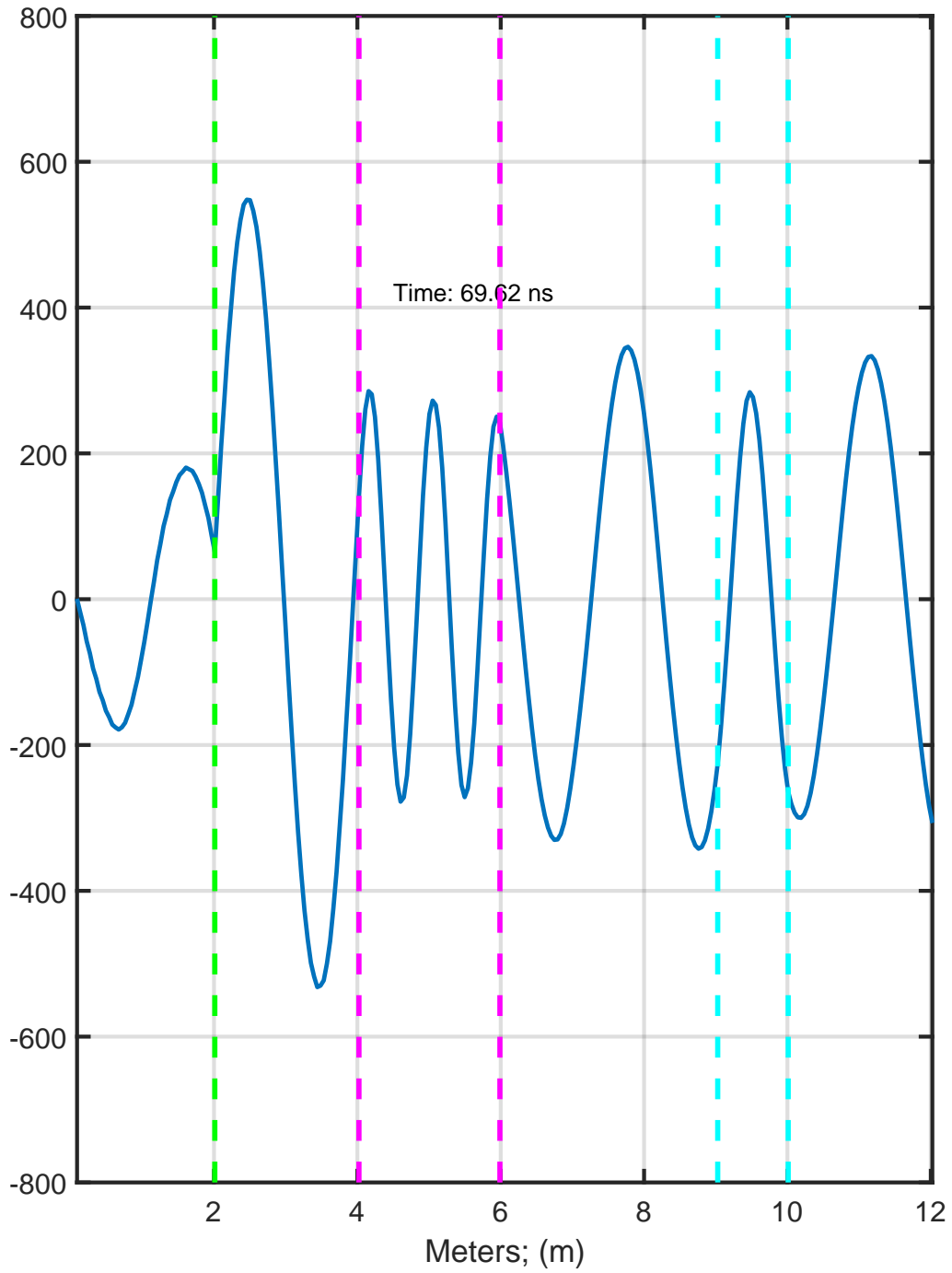
Figure 5.14: FDTD solution of the time domain electric field intensity for the second example problem.
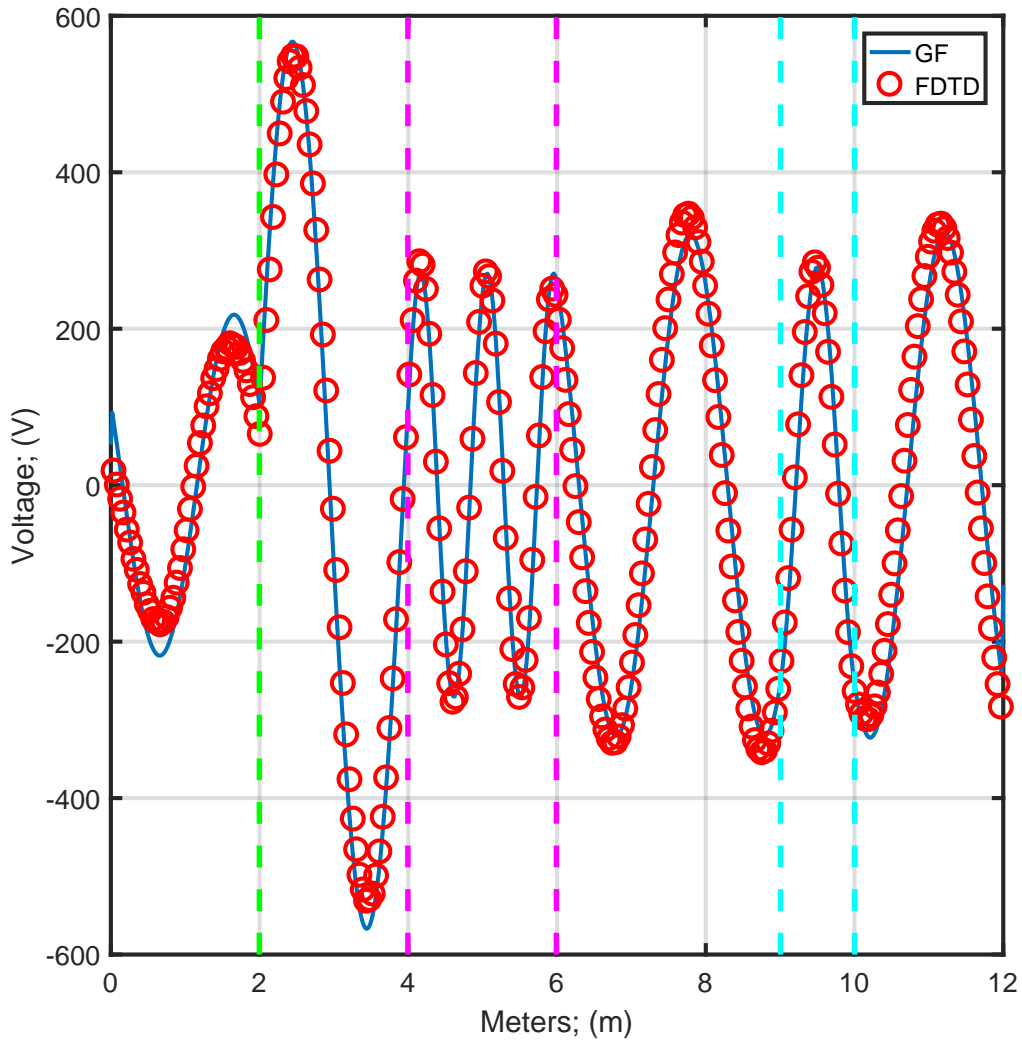
Figure 5.15: Correlation of the electric field intensity results for the FDTD and Green's function methods for the second example problem.

5.4 Conclusion

In this chapter, the Green's function method was investigated and illustrated using two one-dimensional examples. The motivation for this investigation comes from the desire to develop a more analytical approach to solving antenna problems and the Green's function method has beneficial qualities for this task. One of the primary benefits is that when a Green's function exists for a problem and is found, the response of the system to any input can be found. Often it is desirable to characterize an antenna over a broad frequency range or multiple bands. The issue of needing to run multiple lengthy FDTD simulations can be mitigated by applying a semi-analytic, Green's function approach. There can also be more physical insight gained with the Green's function approach.

Of interest to the author, as a result of this research effort, is the development of efficient simulation methods for antennas. More recently, the method of characteristic modes has been gaining momentum, due to the work of [68–71], as a promising method of simulating antennas and gaining physical insight into the governing physics [72]. This approach has been used to solve a variety of problems, ranging from an unmanned aerial vehicle antenna design [73] to the hemispherical helix antenna [74]. Most recently, work has been done to integrate the capabilities of the Green's function into characteristic mode theory [75–77]. The power of the Green's function and characteristic mode theory makes for an exciting research opportunity that would help to provide intuition for antenna designers and make a departure from guess and check methods.

CHAPTER 6

Conclusion

The development and presentation of a novel PCB stack design technique for antennas has been the primary contribution of this thesis. This method is well-suited for the design of ESAs and has been applied to the hemispherical helix antenna. Design enhancements were presented for the utilization of the volume within the antenna structure for housing PCB components. Then, a sensitivity analysis was performed on the PCB stack antenna to quantify the impact of manufacturing tolerances on antenna performance and to identify opportunities for additional design enhancements, such as the addition of a broadband impedance matching network to increase operational bandwidth.

The aforementioned PCB stack approach was evaluated using commercial simulation software based on the FDTD method. While the FDTD method is a powerful technique, the approach can leave the user with a lack of physical insight for a given antenna design. This motivated a research effort into more analytical methods that could be utilized. The Green's function method is often taught as part of graduate courses in electromagnetics and is one such analytic approach for solving inhomogeneous boundary value problems. However, Green's functions are generally presented in literature with a lack of illustrative examples, which can be critical in the understanding of the topic. A secondary contribution of this thesis is a discussion on the Green's function method and the presentation of illustrative examples.

In order to realize further enhancements to the PCB stack method, such as lower Q, future work involves the development of an analytic model. It is hypothesized that the physical insight gained through an analytic model could be used to identify methods of exciting higher-order resonant modes of the HHA. Decreasing the separation of these modes could lead to increases in operational bandwidth. The Green's function method could be used in conjunction with characteristic modes analysis to achieve an antenna simulation approach that is a departure from more common place guess and check design methods.

References

[1] P. M. Słobodzian, "Challenges of design and practical application of ltcc chip antennas," in *Telecommunication in Modern Satellite, Cable and Broadcasting Services (TELSIKS), 2015 12th International Conference on*, Oct 2015, pp. 147–155.

[2] J. Ziegler and A. Zadehgol, "Design and simulation of a four-arm hemispherical helix antenna realized through a stacked printed circuit board structure," in *2016 IEEE Electrical Design of Advanced Packaging and Systems (EDAPS)*, Dec. 2016.

[3] W. Stutzman and G. Thiele, *Antenna Theory and Design*, 3rd ed.   Wiley, 2012.

[4] L. J. Chu, "Physical limitations of omni-directional antennas,," *J. Appl. Phys.*, vol. 19, no. 12, pp. 1163–1175, 1948.

[5] J. S. McLean, "A re-examination of the fundamental limits on the radiation q of electrically small antennas," *IEEE Transactions on Antennas and Propagation*, vol. 44, no. 5, pp. 672–, May 1996.

[6] H. L. Thal, "New radiation q limits for spherical wire antennas," *IEEE Transactions on Antennas and Propagation*, vol. 54, no. 10, pp. 2757–2763, Oct 2006.

[7] O. S. Kim, O. Breinbjerg, and A. D. Yaghjian, "Electrically small magnetic dipole antennas with quality factors approaching the chu lower bound," *IEEE Transactions on Antennas and Propagation*, vol. 58, no. 6, pp. 1898–1906, June 2010.

[8] O. S. Kim, "Electrically small circularly polarized spherical antenna with air core," in *Antennas and Propagation (EuCAP), 2013 7th European Conference on*, April 2013, pp. 233–236.

[9] O. S. Kim, O. Breinbjerg, and A. D. Yaghjian, "Electrically small magnetic dipole antennas with quality factors approaching the chu lower bound," *IEEE Transactions on Antennas and Propagation*, vol. 58, no. 6, pp. 1898–1906, June 2010.

[10] O. S. Kim, "Minimum q circularly polarized electrically small spherical antennas," in *Antennas and Propagation (APSURSI), 2011 IEEE International Symposium on*, July 2011, pp. 750–752.

[11] S. R. Best, "A comparison of electrically small spherical helix and spherical resonator antennas," in *Antennas and Propagation, 2007. EuCAP 2007. The Second European Conference on*, Nov 2007, pp. 1–6.

[12] N. Jastram and D. S. Filipovic, "Pcb-based prototyping of 3-d micromachined rf sub-systems," *IEEE Transactions on Antennas and Propagation*, vol. 62, no. 1, pp. 420–429, Jan 2014.

[13] J. A. Brister and R. M. Edwards, "Design of a balanced ball antenna using a spherical helix wound over a full sphere," in *Antennas and Propagation Conference (LAPC), 2011 Loughborough*, Nov 2011, pp. 1–4.

[14] J. J. Adams, E. B. Duoss, T. F. Malkowski, J. A. Lewis, and J. T. Bernhard, "Design of spherical meanderline antennas," in *Antennas and Propagation (APSURSI), 2011 IEEE International Symposium on*, July 2011, pp. 765–768.

[15] M. Kong, G. Shin, S. H. Lee, and I. J. Yoon, "Electrically small folded spherical helix antennas using copper strips and 3d printing technology," *Electronics Letters*, vol. 52, no. 12, pp. 994–996, 2016.

[16] H. R. Stuart and C. Tran, "Small spherical antennas using arrays of electromagnetically coupled planar elements," *IEEE Antennas and Wireless Propagation Letters*, vol. 6, pp. 7–10, 2007.

[17] O. S. Kim, "Rapid prototyping of electrically small spherical wire antennas," *IEEE Transactions on Antennas and Propagation*, vol. 62, no. 7, pp. 3839–3842, July 2014.

[18] ——, "3d printing electrically small spherical antennas," in *2013 IEEE Antennas and Propagation Society International Symposium (APSURSI)*, July 2013, pp. 776–777.

[19] S. Oshima, K. Matsunaga, H. Morimura, and M. Harada, "3d integration techniques using stacked pcbs and small dipole antenna for wireless sensor nodes," in *CPMT Symposium Japan, 2012 2nd IEEE*, Dec 2012, pp. 1–4.

[20] S. R. Best, "The radiation properties of electrically small folded spherical helix antennas," *IEEE Transactions on Antennas and Propagation*, vol. 52, no. 4, pp. 953–960, April 2004.

[21] ——, "The performance properties of electrically small resonant multiple-arm folded wire antennas," *IEEE Antennas and Propagation Magazine*, vol. 47, no. 4, pp. 13–27, Aug 2005.

[22] T. V. Hansen, O. S. Kim, and O. Breinbjerg, "Stored energy and quality factor of spherical wave functions-in relation to spherical antennas with material cores," *IEEE Transactions on Antennas and Propagation*, vol. 60, no. 3, pp. 1281–1290, March 2012.

[23] S. R. Best, "A discussion on electrically small antennas loaded with high permittivity and permeability materials," in *2011 International Workshop on Antenna Technology (iWAT)*, March 2011, pp. 90–93.

[24] R. F. Harrington, *Time-harmonic electromagnetic fields*, ser. IEEE press series on electromagnetic wave theory. Piscataway, NJ: J. Wiley and sons New York Chichester Weinheim, 2001.

[25] M. S. Smith, "Properties of dielectrically loaded antennas," *Electrical Engineers, Proceedings of the Institution of*, vol. 124, no. 10, pp. 837–839, October 1977.

[26] J. Ziegler and A. Zadehgol, "Electrically Small PCB Stack Hemispherical Helix Antenna with Air Core," in *2017 International Workshop on Antenna Technology (iWAT)*, Mar. 2017.

[27] H. A. Wheeler, "Fundamental limitations of small antennas," *Proceedings of the IRE*, vol. 35, no. 12, pp. 1479–1484, Dec 1947.

[28] ——, "The spherical coil as an inductor, shield, or antenna," *Proceedings of the IRE*, vol. 46, no. 9, pp. 1595–1602, Sept 1958.

[29] O. S. Kim, "Minimum q electrically small antennas," *IEEE Transactions on Antennas and Propagation*, vol. 60, no. 8, pp. 3551–3558, Aug 2012.

[30] J. Ziegler and A. Zadehgol, "Design and simulation of a four-arm hemispherical helix antenna realized through a stacked printed circuit board structure," in *2016 IEEE Electrical Design of Advanced Packaging and Systems (EDAPS)*, Dec 2016, pp. 83–85.

[31] J. Zheng, X. Gao, Z. Zhang, and Z. Feng, "A compact eighteen-port antenna cube for mimo systems," *IEEE Transactions on Antennas and Propagation*, vol. 60, no. 2, pp. 445–455, Feb 2012.

[32] A. D. Yaghjian and S. R. Best, "Impedance, bandwidth, and q of antennas," *IEEE Transactions on Antennas and Propagation*, vol. 53, no. 4, pp. 1298–1324, April 2005.

[33] "FCC Online Table of Frequency Allocations," https://transition.fcc.gov/oet/spectrum/table/fcctable.pdf, Aug. 2016.

[34] L. Krupka, L. Vojtech, and M. Neruda, "The issue of LPWAN technology coexistence in IoT environment," in *2016 17th International Conference on Mechatronics - Mechatronika (ME)*, Dec. 2016, pp. 1–8.

[35] C. A. Balanis, *Antenna theory: analysis and design.* John Wiley & Sons, 2016.

[36] H. A. Wheeler, "Fundamental Limitations of Small Antennas," *Proceedings of the IRE*, vol. 35, no. 12, pp. 1479–1484, Dec. 1947.

[37] ——, "The Spherical Coil as an Inductor, Shield, or Antenna," *Proceedings of the IRE*, vol. 46, no. 9, pp. 1595–1602, Sep. 1958.

[38] S. R. Best, "The performance properties of an electrically small folded spherical helix antenna," in *IEEE Antennas and Propagation Society International Symposium (IEEE Cat. No.02CH37313)*, vol. 4, 2002, pp. 18–21 vol.4.

[39] J. W. Kuo and Y. E. Wang, "The folded dipole perspective of electrical small spherical helix antennas," in *2008 IEEE Antennas and Propagation Society International Symposium*, Jul. 2008, pp. 1–4.

[40] J. J. Adams and J. T. Bernhard, "A low Q electrically small spherical antenna," in *2008 IEEE Antennas and Propagation Society International Symposium*, Jul. 2008, pp. 1–4.

[41] C. Pfeiffer, X. Xu, S. R. Forrest, and A. Grbic, "A printed spherical helix antenna," in *2010 14th International Symposium on Antenna Technology and Applied Electromagnetics the American Electromagnetics Conference*, Jul. 2010, pp. 1–4.

[42] C. Pfeiffer, A. Grbic, X. Xu, and S. R. Forrest, "Novel methods to analyze and fabricate electrically small antennas," in *2011 IEEE International Symposium on Antennas and Propagation (APSURSI)*, Jul. 2011, pp. 761–764.

[43] J. J. Adams, S. C. Slimmer, T. F. Malkowski, E. B. Duoss, J. A. Lewis, and J. T. Bernhard, "Comparison of Spherical Antennas Fabricated via Conformal Printing: Helix, Meanderline, and Hybrid Designs," *IEEE Antennas and Wireless Propagation Letters*, vol. 10, pp. 1425–1428, 2011.

[44] J. Ziegler and A. Zadehgol, "Stacked printed circuit board implementations of three dimensional antennas," U.S. Provisional Patent Application 62/432,389, Dec. 09, 2016.

[45] *Sim4Life*, ZMT, Zürich, Switzerland.

[46] "Advanced Circuits' Capabilities," http://www.4pcb.com/ Advanced-Circuits-PCB-Capabilities-12-1-15.pdf, Dec. 2015.

[47] J. J. Adams and J. T. Bernhard, "Tuning Method for a New Electrically Small Antenna With Low," *IEEE Antennas and Wireless Propagation Letters*, vol. 8, pp. 303–306, 2009.

[48] H. F. Pues and A. R. V. de Capelle, "An impedance-matching technique for increasing the bandwidth of microstrip antennas," *IEEE Transactions on Antennas and Propagation*, vol. 37, no. 11, pp. 1345–1354, Nov. 1989.

[49] R. K. Ulrich and W. D. Brown, "Organic Printed Circuit Board Materials and Processes," in *Advanced Electronic Packaging*. Wiley-IEEE Press, 2006, pp. 105–147.

[50] K. Yee, "Numerical solution of initial boundary value problems involving maxwell's equations in isotropic media," *IEEE Transactions on Antennas and Propagation*, vol. 14, no. 3, pp. 302–307, May 1966.

[51] D. Sullivan, *Electromagnetic Simulation Using the FDTD Method*, 2nd ed. Wiley, 2013.

[52] J. Jin, *Concluding Remarks on Computational Electromagnetics*. Wiley-IEEE Press, 2010, pp. 533–558. [Online]. Available: http://ida.lib.uidaho.edu:2065/xpl/ articleDetails.jsp?arnumber=5628388

[53] E. R. C. Phillips, J. Parr, *Signals, Systems, and Transforms*, 4th ed. Pearson, 2008.

[54] D. Sullivan, *Quantum Mechanics for Electrical Engineers*, 1st ed. Wiley, 2012.

[55] J. G. V. Bladel, *Linear Analysis*. Wiley-IEEE Press, 2007, pp. 1–49. [Online]. Available: http://ida.lib.uidaho.edu:2065/xpl/articleDetails.jsp?arnumber=5236586

[56] J. Jin, *The Finite Element Method in Electromagnetics*. Wiley, 2002.

[57] R. Tazzioli, "Green's function in some contributions of 19th century mathematicians," *Historia Mathematica*, vol. 28, no. 3, pp. 232 – 252, 2001. [Online]. Available: http://www.sciencedirect.com/science/article/pii/S0315086001923158

[58] C. Balanis, *Advanced Engineering Electromagnetics*, 2nd ed.   Wiley, 2012.

[59] J. Vazquez and C. G. Parini, "Discrete green's function formulation of fdtd method for electromagnetic modelling," *Electronics Letters*, vol. 35, no. 7, pp. 554–555, Apr 1999.

[60] R. E. Collin, *Green's Functions.*   Wiley-IEEE Press, 1991, pp. 55–172. [Online]. Available: http://ieeexplore.ieee.org/xpl/articleDetails.jsp?arnumber=5265595

[61] R. Bera, A. Bandyopadhyay, and P. Ray, *Mathematical Physics for Engineers*, 1st ed.   New Academic Science, 2011. [Online]. Available: http://ida.lib.uidaho.edu:3500/lib/uidaho/detail.action?docID=10595621

[62] F. T. Ulaby, *Fundamentals of Applied Electromagnetics.*   Upper Saddle River, NJ, USA: Prentice-Hall, Inc., 1997.

[63] J. A. Stratton, *Electromagnetic Theory.*   John Wiley & Sons, Jan. 2007.

[64] W. C. Chew, "Planarly Layered Media," in *Waves and Fields in Inhomogenous Media.* Wiley-IEEE Press, 1995, pp. 45–160.

[65] W. J. Parnell, *MATH 34032 - Greens functions integral equations and applications.* University of Manchester, 2013. [Online]. Available: http://www.maths.manchester.ac.uk/~wparnell/MT34032_2013/greens_notes.pdf

[66] J.-M. Jin, "Basic Electromagnetic Theory," in *Theory and Computation of Electromagnetic Fields.*   Wiley-IEEE Press, 2010, pp. 1–42.

[67] I. Stakgold and M. J. Holst, *Green's Functions and Boundary Value Problems.*   John Wiley & Sons, Mar. 2011.

[68] R. Garbacz and R. Turpin, "A generalized expansion for radiated and scattered fields," *IEEE Transactions on Antennas and Propagation*, vol. 19, no. 3, pp. 348–358, May 1971.

[69] R. Harrington and J. Mautz, "Theory of characteristic modes for conducting bodies," *IEEE Transactions on Antennas and Propagation*, vol. 19, no. 5, pp. 622–628, Sep. 1971.

[70] ——, "Computation of characteristic modes for conducting bodies," *IEEE Transactions on Antennas and Propagation*, vol. 19, no. 5, pp. 629–639, Sep. 1971.

[71] M. Cabedo-Fabres, E. Antonino-Daviu, A. Valero-Nogueira, and M. F. Bataller, "The Theory of Characteristic Modes Revisited: A Contribution to the Design of Antennas for Modern Applications," *IEEE Antennas and Propagation Magazine*, vol. 49, no. 5, pp. 52–68, Oct. 2007.

[72] Y. Chen and C.-F. Wang, "Introduction," in *Characteristic Modes*. John Wiley & Sons, Inc, 2015, pp. 1–35.

[73] Y. Chen and C. F. Wang, "Electrically Small UAV Antenna Design Using Characteristic Modes," *IEEE Transactions on Antennas and Propagation*, vol. 62, no. 2, pp. 535–545, Feb. 2014.

[74] K. A. Obeidat, B. D. Raines, and R. G. Rojas, "Design and analysis of a helical spherical antenna using the theory of characteristic modes," in *2008 IEEE Antennas and Propagation Society International Symposium*, Jul. 2008, pp. 1–4.

[75] Q. I. Dai, H. Gan, W. C. Chew, and C. F. Wang, "Characteristic mode analysis using green's function of arbitrary background," in *2016 IEEE International Symposium on Antennas and Propagation (APSURSI)*, Jun. 2016, pp. 423–424.

[76] Y. Chen and S. Yang, "Characteristic mode theory for antennas with multilayered media," in *2016 Progress in Electromagnetic Research Symposium (PIERS)*, Aug. 2016, pp. 866–868.

[77] D. J. Ludick and D. B. Davidson, "Applying characteristic mode analysis to finite antenna array design," in *2016 International Conference on Electromagnetics in Advanced Applications (ICEAA)*, Sep. 2016, pp. 934–937.